UNIVERSITY OF CALIFORNIA
RIVERSIDE

Silver Nanowire-Based Near-Field Scanning Optical Microscope for Photocurrent Mapping

A Dissertation submitted in partial satisfaction
of the requirements for the degree of

Doctor of Philosophy

in

Electrical Engineering

by

Qiushi Liu

December 2018

Dissertation Committee:
Dr. Ming Liu, Chairperson
Dr. Elaine D Haberer
Dr. Jianlin Liu

The Dissertation of Qiushi Liu is approved:

Committee Chairperson

University of California, Riverside

Acknowledgments

I would like to express my gratitude to my research advisor, Dr. Ming Liu, wholeheartedly, for his academic mentorship and constant supports during my Ph.D. studies. His visions in electrical engineering and research advice have guided me throughout my Ph.D. research activities. It's been a great pleasure and fortune for me to have him as my advisor.

I would like to thank the Department of Electrical and Computer Engineering at University of California, Riverside, especially the members of my dissertation committee, Dr. Elaine D Haberer, and Dr. Jianlin Liu, for their support on my dissertation research. I would like to thank Dr. Ruoxue Yan for her kindly help during my research. I would like to thank all my laboratory mates with whom I have conducted research together, Sanggon Kim, Peter Bryler, Xuezhi Ma, Yangzhi Zhu, Da Xu, Ning Yu, Leonard Apontti. I want to acknowledge the National Science Foundation for its support for my Ph.D. research. I would like to express my deepest gratitude to my family. Thanks for their generous and endless love to me. They are always with me when I went through tough situation and provided encouragement and supports to me.

ABSTRACT OF THE DISSERTATION

Silver-Based High Spatial Resolution Near-Field Photocurrent Mapping of Two-Dimensional Materials

by

Qiushi Liu

Doctor of Philosophy, Graduate Program in Electrical Engineering

University of California, Riverside, December 2018

Dr. Ming Liu, Chairperson

Silver-based Near-field Scanning Optical Microscopy provides access to high spatial resolution photocurrent image mapping of the surface of a variety of two-dimensional material and nanostructures. By observing the photocurrent from the interaction between nano-photons and nano-materials, nano-scale bandstructure information can be studied. For one of its application, strain-induced graphene wrinkle FET's photocurrent has been investigated. Under different channel and gate bias voltages, the photocurrent responses have been mapped point by point, and bias-voltage-related bandstructure information has been obtained. 15 nm photocurrent imaging resolution has been achieved for the first time. Conventional scattering Near-field Scanning Optical Microscopy is not able to provide near-field electric field distribution within the gap between tip and sample. Here we provide an accurate method to reconstruct the near-field electric field on a wide range of two-dimensional material and nanostructures.

Contents

List of figures

List of tables

Chapter 1 The Near-field Scanning Optical Microscope

1.1 Introduction to Optical Diffraction Limit

The ability to obverse samples with high spatial resolution is important in physics, chemistry, material science, and biology fields. The conventional optical microscope is limited by the wavelength of the light source. According to Abbe's theory, the resolving capability is limited due to the loss of diffraction light. The microscopy's optical resolution can be expressed by the Rayleigh criterion[1]:

$$\mathrm{d} = 0.61\frac{\lambda}{\mathrm{NA}}$$

The Rayleigh criterion is just one of the way to describe the optical resolution. They are describing the same limitation: conventional optical systems are not able to collect the whole electromagnetic spectrum emitted from the sample far away.

Before going into details, two concepts will be introduced, the near field and the far field light. The near field and far field describe the regions around the object with different electromagnetic wave behaviors. The non-radiative near field electromagnetic wave is confined closely to the antenna or scattering objects and decreases exponentially with distance increases. On the other hand, the far field is inversely proportional to the square of the distance. The rapid drop of the near field makes the near-field electromagnetic wave vanish within a few wavelengths from the object. For visible light, its near-field part is tightly confined to the object within tens of nanometers.

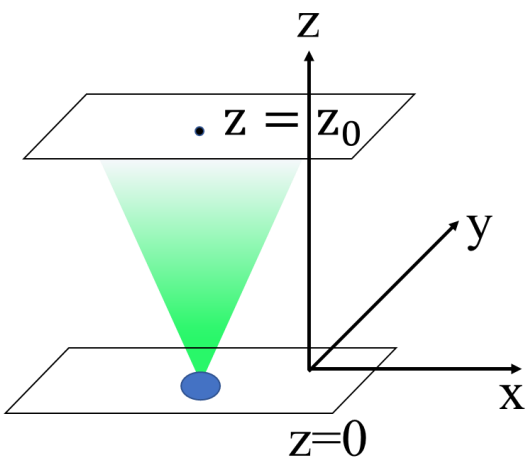

Figure 1. 1 Plane wave light propagating along the z-axis from the sources z=0 to the receiving plane $z=z_0$.

A plane EM wave has the following formation:

$$\mathbf{E}(x,y,z) = \mathbf{E_0}\exp(-j(k_{x,\perp}x + k_{y,\perp}y + k_{z,\parallel}z))$$

$$k_{x,\perp}{}^2 + k_{y,\perp}{}^2 + k_{z,\parallel}{}^2 = k^2$$

Here $k_{x,\perp}$, $k_{y,\perp}$ and $k_{z,\parallel}$ are the spatial momentum in x, y, and z-direction in cartesian coordinates. k, a real value, is the total momentum of the EM wave. Based on the Fourier transform theory, in a linear system, an arbitrary function can be expressed as the integration of harmonic functions. This theory can be applied to electromagnetic theory where an arbitrary EM field can be expressed as a superposition of harmonic components of plane waves. As shown in the figure, a sample is located at the z=0 plane. Suppose it emits light in all the directions, then the electric field arrives at plane z=constant can be written as[2]:

$$\mathbf{E}(x,y,z) = \mathbf{E_0}\iint_{-\infty}^{+\infty}\hat{E}(k_x,k_y;0)\times\exp\left(-j\left(k_x x + k_y y\right)\right)\times\exp(-jk_z z)\,dk_x dk_y$$

We only consider electric field $\mathbf{E}(x, y, z)$. Magnetic field $\mathbf{H}(x, y, z)$ is analogous to elthe ectric field. Here the $\widehat{E}(k_x, k_y; 0)$ is the spatial frequency distribution of the electric field in the z=0 plane. $\exp(-jk_z z)$ describes the wave distribution along the z-axis.

In the case of ${k_{z,\parallel}}^2 = k^2 - ({k_{x,\perp}}^2 + {k_{y,\perp}}^2) \geq 0$, $k_{z,\parallel}$ is a real value. $\exp(-jk_z z)$ is a propagating term and the wave can propagate along the z-direction.

In the case of ${k_{z,\parallel}}^2 = k^2 - ({k_{x,\perp}}^2 + {k_{y,\perp}}^2) < 0$, $k_{z,\parallel}$ is imaginary value. $\exp(-jk_z z)$ is an exponential decay term and the evanescent wave decreases to zero within a few wavelengths. It cannot propagate along the z-direction.

The propagating wave is the far field light and the non-propagating wave is the near-field light. When the plane is $z=z_0$ far from z=0 plane, only the ${k_{z,\parallel}}^2 = k^2 - ({k_{x,\perp}}^2 + {k_{y,\perp}}^2) \geq 0$ part can be received.

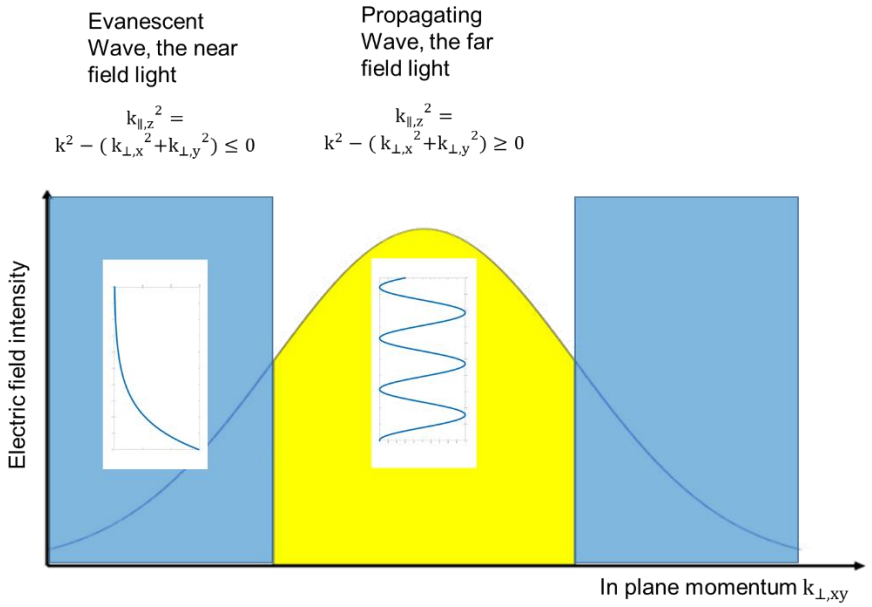

Figure 1. 2 $k_{xy,\perp}$ distribution for different $k_{z,\parallel}$.

When sample scattering or emitting light, its optical image ($\mathbf{E}(x, y, z)$ and $\mathbf{H}(x, y, z)$) is formed by a summation of plane waves with different momentums, which is the light's spatial frequency k. The geometry information is contained in the spatial frequency spectrum. Now consider the most important case where the sample optical image is formed by a summation of plane waves, whose spatial frequencies follow the Gaussian distribution as shown in the figure. In the plane z=constant sufficiently far from the sample z=0 plane, the plane waves with ${k_{z,\parallel}}^2 = k^2 - ({k_{x,\perp}}^2 + {k_{y,\perp}}^2) < 0$ cannot reach the plane and their information will be lost, only the center yellow region where ${k_{z,\parallel}}^2 = k^2 - ({k_{x,\perp}}^2 + {k_{y,\perp}}^2) \geq 0$ can be collected. Since the Fourier transform of Gaussian distribution ($\widehat{E}(k_x, k_y)$) with bandwidth (${k_x}^2 + {k_y}^2) \leq k^2$ in a spatial frequency domain is another Gaussian distribution ($\mathbf{E}(x, y, z)$) with bandwidth $(x^2 + y^2) \leq \frac{1}{k^2}$ in the real space domain, the lateral resolution obtained in far field region is limited by

$$r = \sqrt{(x^2 + y^2)} \leq \frac{1}{k} = \frac{\lambda}{2\pi n}$$

Here $k = \frac{2\pi n}{\lambda}$ where n is the refractive index of the medium where light propagates and λ is the light wavelength. Considering the limitation of collecting aperture size of the optical system in the real world, the actual lateral resolution is limit by $r = \frac{\lambda}{2\pi NA}$ where NA is the numerical aperture.

Simply speaking, diffraction limitation in the far field originates from the loss of near-field information and the optical image cannot be fully recovered using the conventional optical system. To achieve higher optical resolution, the optical system with larger NA and shorter wavelength have been employed. These gains in resolution, however, have been made at the expense of more complicated setup and potential damage to the sample.

1.2 High-Resolution Imaging Techniques

For the visible light, the resolution is around 200 ~ 300 nm which is much larger than the micro-scale structure and limits the application of conventional optical microscopy in nano-tech-knowledge. Lots of efforts have been made to gain higher resolution with other techniques such as Scanning Electron Microscopy (SEM), Tunneling Electron Microscopy (TEM) and Scanning Probe Microscopy (SPM), including Atomic Force Microscopy (AFM) and Scanning Tunneling Microscopy (STM).

The high resolution from these techniques is at the cost of losing optical information. Moreover, many of these high-resolution techniques have a special requirement about the sample preparation and the working environment, which decrease the flexibility to deal with different experimental situations. On the other hand, the spectroscopy analysis and polarization properties based on an optical microscope consists of lots of useful information and are important for many applications.

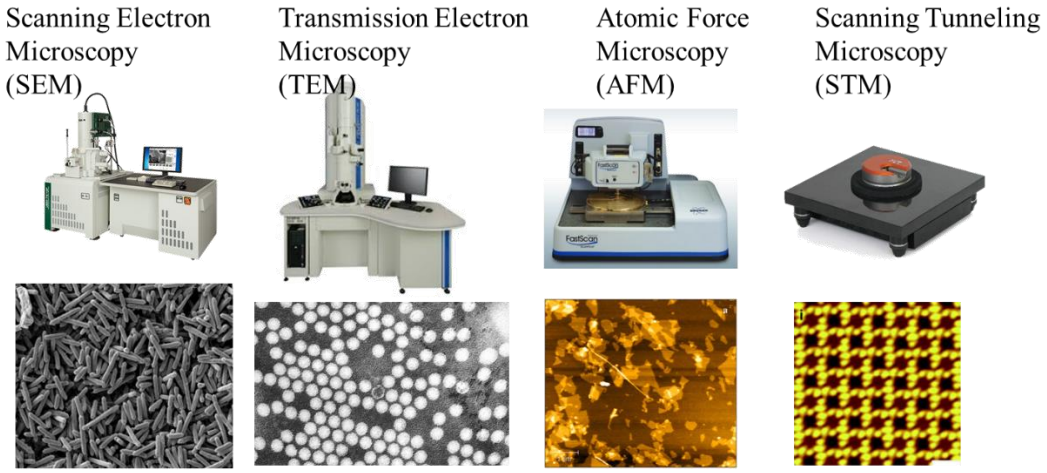

Figure 1. 3 Different types of high-resolution imaging techniques.

	Conventional Optical Microscope	SEM/TEM	SPM
Environment	Air, Liquid, Vacuum	Vacuum	Air, Liquid, Vacuum
Lateral Resolution	1μm	SEM: 1-5 nm TEM: 0.1 nm	AFM: 2-10 nm STM: 0.01 nm
Vertical Resolution	N/A	N/A	AFM: 0.1 nm STM: 0.01 nm
Magnification	$1 - 2 \cdot 10^3$	$10 - 10^8$	$5 \cdot 10^3 - 10^8$
Sample	Not completely transparent.	Conductive, no charge accumulation. TEM: Thin film.	Surface height < 10 mm.
Contrast	Absorption, Reflection.	Scattering, Diffraction	STM: Tunneling
Disadvantages	Limited resolution	Losing optical contrast information	Losing optical contrast information

Table 1 high-resolution imaging techniques

1.3 Near-Field Scanning Optical Microscope (NSOM)

Atomic Force Microscopy (AFM) and Scanning Tunneling Microscopy (STM) can be used to study the sample close to atomic level resolution at ambient conditions. Their tips can be controlled to maintain the distance to the sample within a few nanometers. Combining the high

resolution of these methods with the abundant optical information has driven the development of Near-field Scanning Optical Microscope (NSOM).

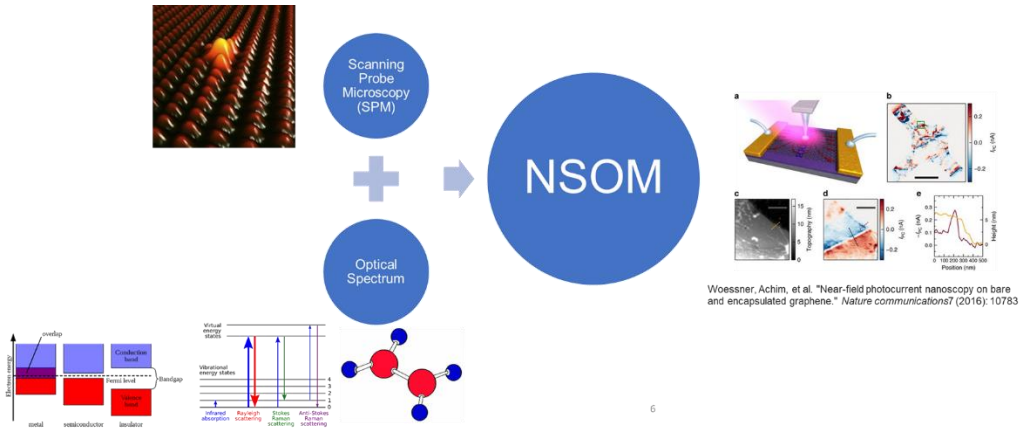

Figure 1. 4 Combining SPM techniques and optical information to get a Near-field Scanning Optical Microscope.

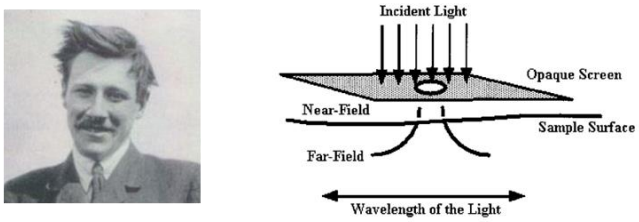

Edward Hutchinson Synge, early in 1928.

Metal screen and hole structure

Figure 1. 5 The first NSOM structure: thin metal film and subwavelength hole structure.

NSOM is a scanning probe microscopy technique based on AFM or STM feedback. During scanning, the NSOM probe is placed close to the sample. The tip size is much smaller than the excitation wavelength and results in an evanescent field. By exploiting the properties of the evanescent wave, NSOM converts the non-propagating evanescent waves into propagating waves. The exploiting of the near-field region within few wavelengths to the source complements the information loss, expands the spatial frequency domain and shrinks the size of real space electric field distribution ($\mathbf{E}(x, y, z)$). By collecting the information hidden in the near-field, NSOM is more

powerful to resolve the optical image. Comparing with conventional far-field techniques, NSOM breaks the diffraction limit and improves the optical lateral resolution within 20nm. The first NSOM is proposed by Edward Hutchinson Synge in 1928. He came up with the idea to use create s subwavelength hole on a thin metal film. When light illuminates onto the hole, this structure creates a near-field around the hole. Therefore, using this structure to scan the sample, reachers can get near-field interaction infromaton.[3,4] After decades of efforts, such subwavelength structure keeps developing and there are two famous structures in NSOM field, the aperture and the apertureless NSOM.

1.4 Aperature and Aperatureless NSOM

Two types of NSOM probes have been studied, Aperture NSOM and Apertureless NSOM as shown in figure 1.6[5]. A typical aperture NSOM is a waveguide coated with metal, with a subwavelength-sized aperture at the end of the probe. As the probe approaches close to the sample, the evanescent wave will be formed between the aperture and the sample. A typical apertureless NSOM is a sharp metal tip. Free space light will be focused on the gap between the probe and the sample where the evanescent wave will be formed.

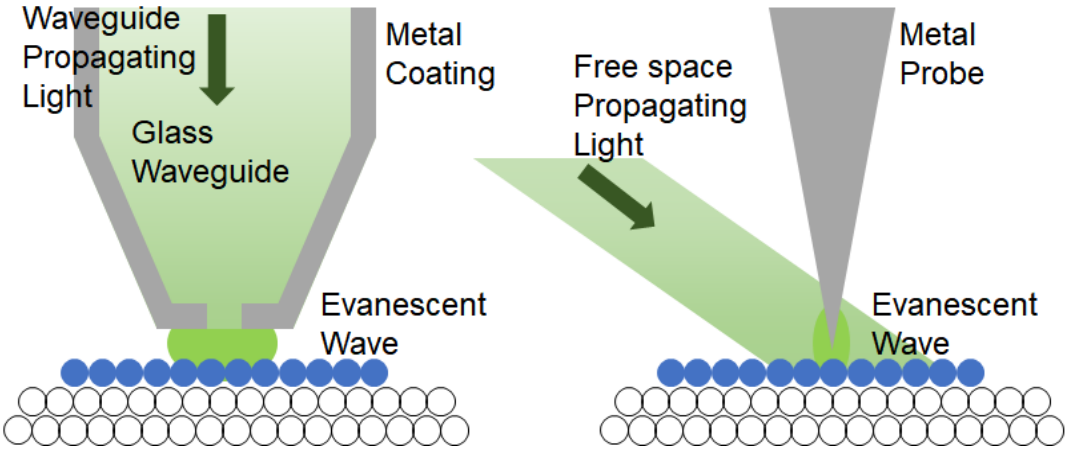

Figure 1. 6 The Aperture and Apertureless NSOM.

In 1972, the first sub-wavelength imaging was developed by Ash and Nicholls[6]. The probe was improved using tapered angle optical fiber via heating and pulling method[7,8]. By changing the heating and pulling parameters, fiber taper angle and diameter can be controlled[9,10]. As the size of the fiber at the taper part decrease beyond incident light cutoff scale, propagating mode in optical fiber is no longer supported and the light starts to scatter from the side wall. To prevent the light from escaping, a layer of metal will be coated to confine the light[7,11,12]. Vacuum evaporate methods are used to deposit metal coating, whose thickness is larger than the excitation light skin depth. A small aperture at the end of the fiber is left open. The whole structure works as a small pinhole where near-field light can be either collected or excited. There are several configurations of operation for aperture NSOM than can be used. The choice depends on the sample properties and the working environment.

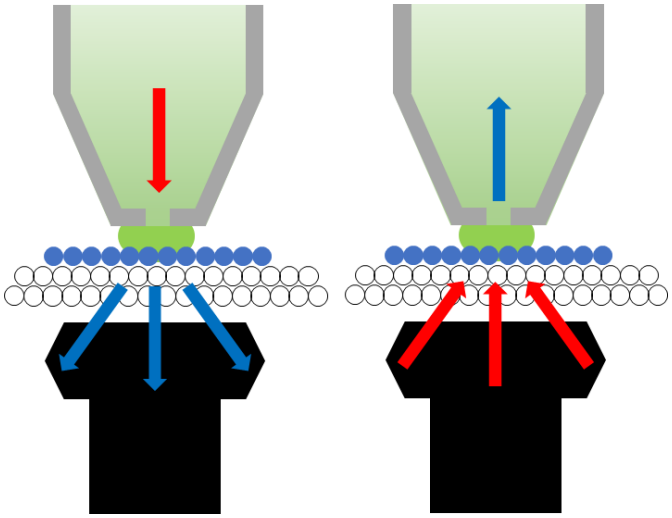

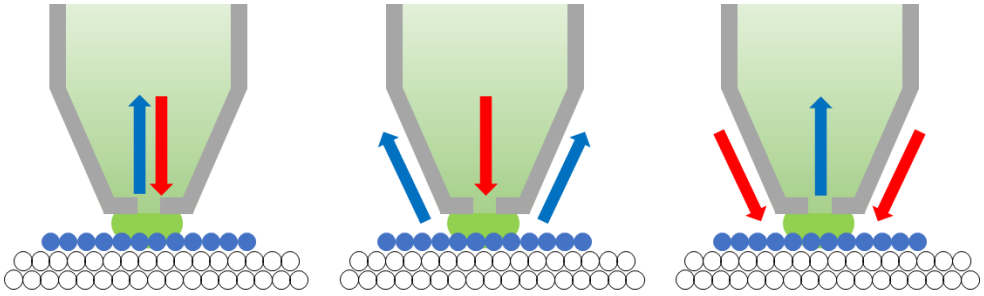

Figure 1. 7 Different aperture NSOM configurations. There are (1) probe in bottom out; (2) bottom in probe out; (3) probe in probe out; (4) probe in side probe out; (5) side probe in probe out.

For example, in the first configuration, light is guided along the fiber and down to the pinhole and excites near-field evanescent wave between the aperture and the sample. The sample will be placed close to the end of the tip and will scatter the evanescent wave into the propagating wave. The sample and its holder are transparent, so an optical lens placed underneath the sample can collect the scattering light. [13,14]

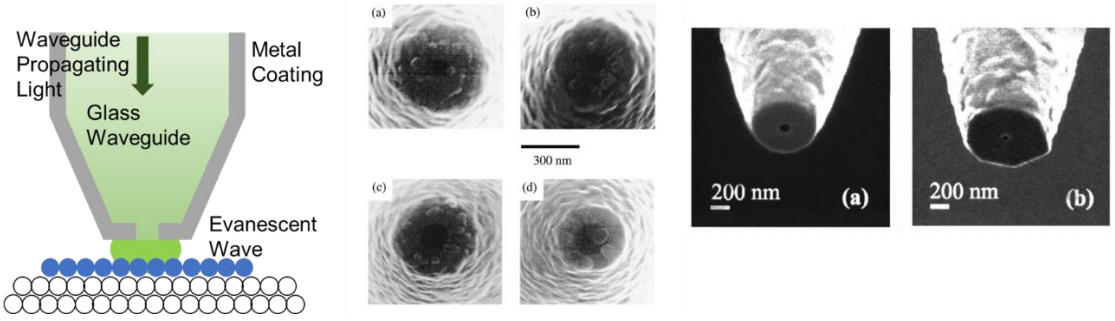

Figure 1. 8 The Aperture NSOM[15,16]

There are several drawbacks for the aperture NSOM. During vacuum evaporating, the roughness of the metal cannot be controlled, the amorphous metal deposition and grain formation will create irregular tip shape which affects the lateral resolution and eventually decrease the scanning image quality. The metal coating quality is critical for NSOM scanning. Another important issue is the extremely low throughput of light power. Typically, the tip aperture size is

around 80-100 nm. Tens of nanowatts of light will reach the end with hundreds of microwatts light guided into it. Such aperture size is still large for the high-resolution imaging. Further decreasing the size of the aperture makes the output light power even smaller. The inefficiency of the probe light transmission ($10^{-4} - 10^{-7}$) is due to the tapered fiber diameter decrease. The diameter of the fiber at the taper region is below the cutoff size of the supporting propagating mode, which makes the light either reflected back or converted into an evanescent wave[17]. Due to the finite skin depth of the metal, part of the evanescent will spread into the metal and be absorbed. Such absorption will locally heat the metal and damage the probe[18-21].

Efforts had been made to improve the smoothness of the probe by employing Focused Ion Beam (FIB) to slice off the irregular part at the end of the probe and produce a flat probe[16,22,23]. This method improves the signal output power by 1 order. However, using FIB to modify the probe increase the complexity and decrease the reproducibility of this technique. By far the best resolution of aperture NSOM is above 20 nm for visible light, which is limited by a minimum aperture size.

To utilize the near-field to obtain sub 20 nm resolution, apertureless NSOM (also known as scattering-type NSOM) has been used with a sharp metal tip which is maintained in a close proximity to the substrate. Instead of using an aperture to conduct light, an external source will illuminate onto the gap between tip and sample. Light with polarization along the tip shaft will induce strongly enhanced the near-field components in the gap. The interaction between the near-field light and the tip-sample system will convert these evanescent waves into scattered propagating waves and the sample local optical information will be collected in the far field.[24]

The interaction between the near-field light and the tip-sample system can be simplified as a point dipole and its mirror image. Then the effective polarizability can be expressed in the following equation:

$$\alpha_{eff} = \frac{\alpha(1+\beta)}{1-\alpha\beta/(16\pi(a+z)^3)}$$

Where $\alpha = 4\pi a^3 \frac{\varepsilon_t - 1}{\varepsilon_t + 2}$, $\beta = \frac{\varepsilon_s - 1}{\varepsilon_s + 1}$, ε_s is the sample dielectric constant, ε_t is the tip dielectric constant, a is tip radius, and z is tip-sample distance.[25,26]

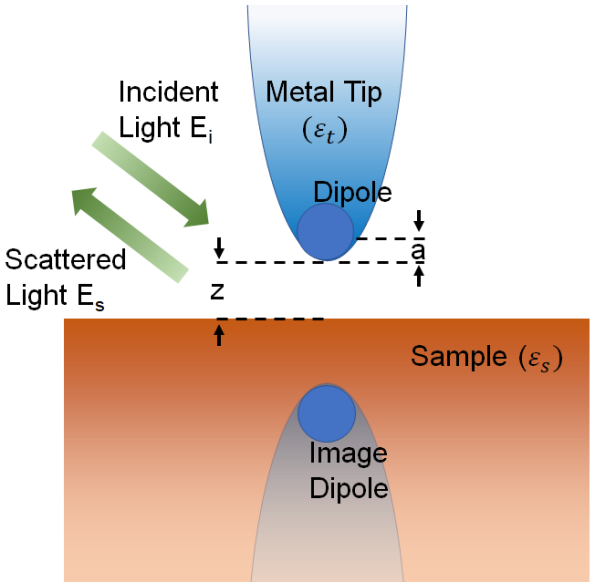

Figure 1. 9 Modelling the near-field interaction in s-SNOM. The replacement of the probing tip by a point dipole.[25,27,28]

The core of the apertureless NSOM lies in the fact that the presence of the sample will modify the effective tip-sample polarizability. Both the real part and the imaginary part of the effective polarizability α_{eff} depend on the dielectric function of the sample. Since the scattered light intensity is proportional to the product of the incident light intensity and the effective polarizability, $E_s \propto \alpha_{eff} E_i$, the spatial variation of the materials can be distinguished via the amplitude and phase contrast. Its resolution is approximately equal to the tip radius (smaller than 20 nm) which beats aperture NSOM due to the smaller near-field interaction volume.[29-31]

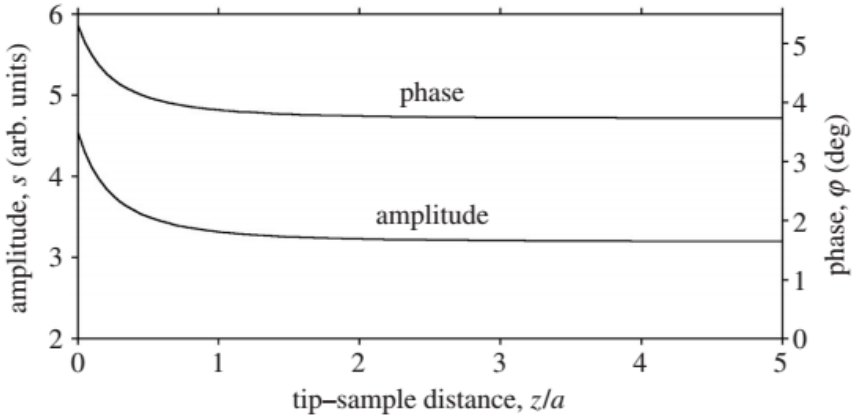

Figure 1. 10 Calculated near-field scattering amplitude s and phase ϕ versus the distance z between the tip sphere and the sample.[25]

Comparing with aperture NSOM, apertureless NSOM probes are easier to fabricate. The idea was proposed by O'Keefe in 1956, followed by John Wessel in 1985, Wickramasinghe & Williams in 1990, Specht in 1992, and Inouye & Kawata in 1994. In 1999, tip-enhanced Raman scattering NSOM was developed as will be mentioned in the following chapter.

The experimental setup for apertureless NSOM consists of the excitation light source, tip-sample distance precisely control system (AFM, STM) and scattering light collection lens. In practice, a metal-coated AFM tip serves as the probe. The light can be excited from the bottom, from the side or from the top. In some cases, the light excitation lens and collection lens can be shared to simplify the setup.

One of the most important issues of apertureless NSOM is the background noise. In their early design, a laser beam focused at the nanoscale gap has a spot size around 10 μm, which is much larger than the tip-sample distance. Therefore, only a small portion of scattering light comes from the near-field within the gap while the rest from the other part won't contribute to the imaging and become the substantial background noise. The early solution is to utilize the AFM tip tapping vibration to create Z-modulation and electronically filter the noise at the vibration frequency Ω.

Since the most part of the laser spot has no tip-enhancement and thus no Z-modulation, this method could eliminate most of the noise. However, it is not enough to suppress the noise comes from tip shaft backscattering, which is also z modulated by the tip. [29]

Generally, the effective polarizability can be expressed as $\alpha_{eff} = s \cdot \exp(i\varphi)$, where s is the amplitude and φ is the phase. According to the equation, both phase and amplitude of $\alpha_{eff}(z)$ change rapidly when $z < a$, which means the tip-sample distance is within few nanometers. When $z \gg$ both phase and amplitude keep almost constant. This nonlinearity $\alpha_{eff}(z)$ is essential for background noise elimination in Z-modulation method since it can be decomposed into the Fourier series:

$$\alpha_{eff} = s_0 \cdot \exp(i\varphi_0) + s_1 \cdot \exp(i\varphi_1) \cdot \cos(\Omega t) + s_2 \cdot \exp(i\varphi_2) \cdot \cos(2\Omega t) + \cdots$$

Modulation and demodulation techniques working at second or even higher harmonic components of Ω have been employed to further eliminate the noise. Two methods (the Heterodyne system and the Homodyne system) and another improved method (the Pseudo-Heterodyne system) based on the Michelson interferometer aperture NSOM have been developed.[32]

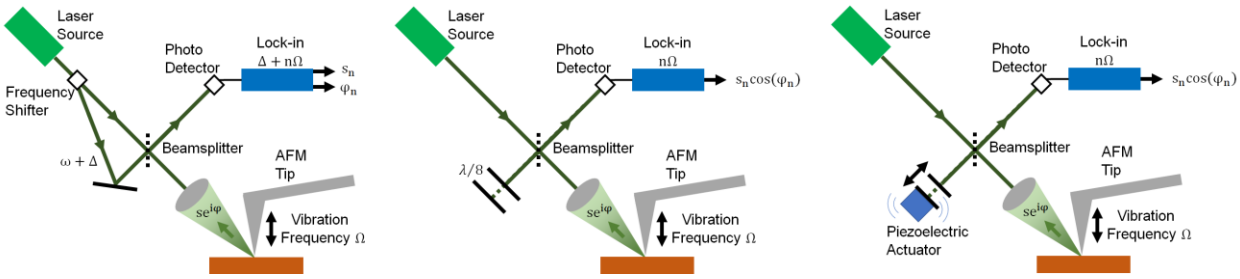

Figure 1. 11 Different modulation and demodulation methods to cancel the large background noise in apertureless NSOM[32-36]

$$E_s = \frac{\alpha_{eff}\pi\sqrt{8\pi/3}}{\lambda^2} E_i = \sigma E_i$$

The scattered far-field light is proportional to the incident light, this part of scattered light is z-modulated. However, in reality, the shaft of the tip will induce an external noise signal which is also z-modulated. So, the relation between scattering and incident light should be changed to:

$$E_s = (\sigma + \sigma_b)E_i$$

If we fix the incident laser wavelength, the σ is equal to α_{eff} times a constant. Therefore, we can use Fourier series to describe $\sigma(z)$ and $\sigma_b(z)$:

$$\sigma = s_0 \cdot \exp(i\varphi_0) + s_1 \cdot \exp(i\varphi_1) \cdot \cos(\Omega t) + s_2 \cdot \exp(i\varphi_2) \cdot \cos(2\Omega t) + \cdots$$

$$\sigma_b = s_{b0} \cdot \exp(i\varphi_{b0}) + s_{b1} \cdot \exp(i\varphi_{b1}) \cdot \cos(\Omega t) + s_{b2} \cdot \exp(i\varphi_{b2}) \cdot \cos(2\Omega t) + \cdots$$

Suppose we don't use any high harmonic techniques mentioned above, then the detected optical signal

$$I \propto |(\sigma + \sigma_b)E_i|^2 = |\sigma + \sigma_b|^2 |E_i|^2$$

$$= |s_0 \cdot \exp(i\varphi_0) + s_1 \cdot \exp(i\varphi_1) \cdot \cos(\Omega t) + s_2 \cdot \exp(i\varphi_2) \cdot \cos(2\Omega t) + \cdots + \sigma_b|^2 |E_i|^2$$

There are always cross terms between σ and σ_b. If σ_b is small, we can ignore it. However, the backscattering from the tip is strong, inducing noise to each term in the equation above. The high harmonic techniques are then developed to separate them.

For the Heterodyne system, a reference laser beam, whose frequency is a shift from ω to $\omega + \Delta$ is induced and superimposed over the signal beam as shown in the figure. The detected optical signal is then changed to:

$$I \propto |(\sigma + \sigma_b)E_i + E_r \exp(i\Delta t)|^2$$

$$\propto |s_0 \cdot \exp(i\varphi_0) + s_1 \cdot \exp(i\varphi_1) \cdot \cos(\Omega t) + s_2 \cdot \exp(i\varphi_2) \cdot \cos(2\Omega t) + \cdots + \sigma_b + \exp(i\Delta t)|^2$$

Where the Δ is the reference beam shifting frequency.

This time there are cross terms without σ_b, but $(\sigma_n + \sigma_{bn})\exp(i\Delta t)$. we only need to extract the signal with the frequency $|\Delta \pm n\Omega|$ and this can be done using a lock-in amplifier. As $n \geq 2$, σ_{bn} vanishes quickly due to the leak of nonlinearity, which makes σ_n outstanding and can be distinguished easily.

The second method is the Homodyne system. Due to the lack of nonlinearity, the noise from backscattering only exists in the first harmonic. So, all the lock-in detections are using high harmonic frequency. A reference beam with same frequency ω is superimposed over the signal beam as shown in the figure, instead of using a different frequency, the reference beam shifts its phase. By moving the mirror, the maximized optical signal corresponding to the real part of the α_{eff} can be measured. By moving a distance of $\frac{\lambda}{8}$, the reference beam phase change by 90°, so the imaginary part of α_{eff} can be measured.

$$I = |\alpha_{eff}E_i + \exp(i\varphi)\,E_r|^2$$

$$= \{(\mathrm{Re}(\alpha_{eff}) + A\cos(\varphi))^2 + (\mathrm{Im}(\alpha_{eff}) + A\sin(\varphi))^2\} \cdot |E_i|^2$$

Where $A = \frac{E_r}{E_i}$.

Another method to separate the σ and σ_b is called the Pseudo-Heterodyne system, which is quite similar to the Heterodyne system. The frequency shift setup is replaced by sinusoidal phase modulation where a piezoelectric actuator is used to drive the mirror. The modulated reference beam can be expressed as Fourier series:

$$E_r = \rho\exp(i\gamma\sin(Mt) + i\psi_r) = \sum_m \rho_m \exp(imMt)$$

$$\rho_m = \rho J_m(\gamma)\exp(i\psi_r + im\pi/2)$$

Where ρ is intensity, M is phase modulation frequency, γ is phase modulation depth. J_m is Bessel function of the first kind, m-th order. Similar to the Heterodyne system, when the reference beam is superimposed over the signal beam as shown in the figure, it generates terms without σ_b with the frequency $f_{n,m} = n\Omega + mM$ when $m \neq 0$. Extracting these frequencies can give us the σ_n.

Due to the optical diffraction limit and NA, the visible light's laser spot is around 10 μm, while our probing area is usually within 10 nm. As long as the light source is larger than the probing area, there would be unnecessary background noises which decrease the image quality. And as long as there are background noises, noise canceling methods are acquired. By employing these high harmonic noise canceling techniques, the apertureless NSOM can provide a high signal to noise ratio as well as high spatial resolution. However, the Michelson interferometer makes the whole setup complicated. For example, when the incident light is visible light (or even shorter wavelength), the adjusting could be very hard to accomplish. Since the wavelength is short, any small misalignment of the mirror may disturb the light interference which makes these methods formidable.

One of the solutions is to deliver and concentrate photons onto nano-scale for probing the sample. With a smaller ruler, we can measure a smaller area. This gives us the motivation of finding another experimental configuration to get rid of the enormous background noise, where the incident light spot should be in the same size of the NSOM tip.

1.5 Surface Plasmon Polariton (SPP)

Before going to the detail about the NSOM tip, the way it guides light and the physics behind the modes it supported should be understood. The interaction between electromagnetic wave and metals can be studied under classical Maxwell's equations without evolving quantum

mechanics down to the nano-scale. At low frequencies, good conductor approximation is valid where the induced free electrons movement will counteract the external EM field in the metal, prohibit the EM wave distribution, and therefore the low-frequency EM wave cannot penetrate into the metal. For higher frequency region up to near infrared, visible, and ultraviolet part, the EM field penetration length starts to increase and finally propagate in the metals. The free-electron-like response at higher frequencies makes metals transparent to the EM wave. The physics behind these phenomena is the induced electrons movement with respect to the external driving force. The electrons movement, which is called the material's optical response, has a strong frequency dependence. Combining external driving field and internal optical response, the total influence can be expressed using the complex electric permittivity $\varepsilon(\omega)$, assuming we are dealing with a nonmagnetic medium whose relative permeability $\mu = 1$. The quantum mechanics is not involved since the spatial and frequency scale we are dealing here are valid for the classical physics.

Over a wide frequency region, the induced electrons movement can be explained using the free electron model (plasma model), where free electrons acting like gas molecules move against fixed ions. The external driving wave will induce collective electrons oscillation. The quantized particle of this electron density oscillation is called the plasmon. Electrons are driven by the external field with their motion damped via collisions. $\gamma = 1/\tau$, where γ is collisions frequency and τ is relaxation time. So, the electron motion can be written as:

$$m\ddot{\mathbf{x}} + m\gamma\dot{\mathbf{x}} = -e\mathbf{E}$$

m is electron mass, x is electron displacement from the ion. If the applied field is harmonic oscillation field $\mathbf{E(t)} = \mathbf{E_0}e^{-i\omega t}$, then:

$$\mathbf{x}(t) = \frac{e}{m(\omega^2 + i\gamma\omega)}\mathbf{E}(t)$$

since polarization $\mathbf{P} = -\mathrm{ne}\mathbf{x}$,

$$\mathbf{P} = -\frac{\mathrm{ne}^2}{\mathrm{m}(\omega^2 + \mathrm{i}\gamma\omega)}\mathbf{E}$$

$$\mathbf{D} = \varepsilon_0(1 - \frac{\omega_\mathrm{p}^2}{\omega^2 + \mathrm{i}\gamma\omega})\mathbf{E}$$

$$\varepsilon(\omega) = 1 - \frac{\omega_\mathrm{p}^2}{\omega^2 + \mathrm{i}\gamma\omega}$$

Here $\omega_\mathrm{p}^2 = \frac{\mathrm{ne}^2}{\varepsilon_0 \mathrm{m}}$ is the plasma frequency of the material.

For high frequency where ω is close to ω_p, the imaginary part of $\varepsilon(\omega)$ is negligible, thus:

$$\varepsilon(\omega) = 1 - \frac{\omega_\mathrm{p}^2}{\omega^2}$$

The Maxwell's equations of the macroscopic form:

$$\nabla \cdot \mathbf{D} = \boldsymbol{\rho}_{\mathrm{ext}}$$

$$\nabla \cdot \mathbf{B} = 0$$

$$\nabla \times \mathbf{E} = -\frac{\partial \mathbf{B}}{\partial \mathrm{t}}$$

$$\nabla \times \mathbf{H} = \mathbf{J_{ext}} + \frac{\partial \mathbf{D}}{\partial \mathrm{t}}$$

Suppose that we are dealing with linear, isotropic, homogeneous, and nonmagnetic media with source free (source charge $\boldsymbol{\rho}_{\mathrm{ext}}$ and current $\mathbf{J_{ext}}$ is outside of the calculation region, which means they are 0 here). Then we are derived the wave equation from the Maxwell's equations as:

$$\nabla \times \nabla \times \mathbf{E} = -\mu_0 \frac{\partial^2 \mathbf{D}}{\partial t^2}$$

Here we don't consider the pure longitudinal EM wave (the bulk plasma at ω_p), only the transverse EM wave. $\nabla \times \nabla \times \mathbf{E} = \nabla(\nabla \cdot \mathbf{E}) - \nabla^2 \mathbf{E}$, $\nabla \cdot (\varepsilon \mathbf{E}) = \varepsilon \nabla \cdot \mathbf{E} + \mathbf{E} \cdot \nabla \varepsilon$, $\nabla \cdot \mathbf{D} = 0$, $\nabla \varepsilon = 0$. Then the equation can be simplified to:

$$\nabla^2 \mathbf{E} - \frac{\varepsilon}{c^2} \frac{\partial^2 \mathbf{E}}{\partial t^2} = 0$$

Here c is the speed of light. Since we are talking about the harmonic oscillation of EM wave, $\mathbf{E}(r, t) = \mathbf{E}(r) e^{-i\omega t}$:

$$\nabla^2 \mathbf{E} - k_0^2 \varepsilon \mathbf{E} = 0$$

Here $k_0 = \frac{\omega}{c}$ is the total wave vector.

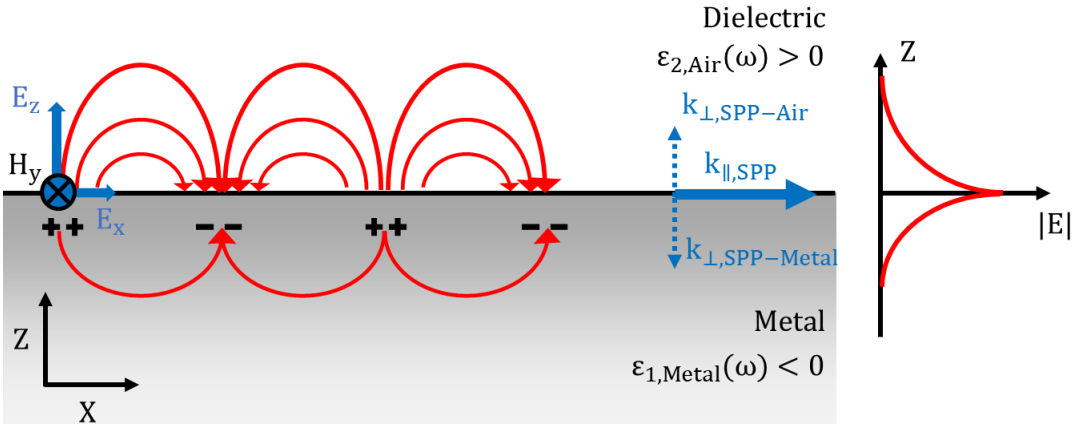

Figure 1. 12 SPP between metal-dielectric interface.

As shown in figure 1.12, suppose there is a transverse EM wave propagating along the interface between metal and dielectric. Metal has permittivity $\varepsilon_1(\omega)$ while dielectric has a permittivity $\varepsilon_2(\omega)$. This interface configuration has infinite width and no permittivity variation in

the y-direction. The different layers are stacked along z-direction and the wave propagates along x-direction with propagation constant $k_x = \beta$. $\mathbf{E}(x, y, z) = \mathbf{E}(z)e^{i\beta x}$. Here we only consider E field, while H can be derived in a same way.[37]

$$\frac{\partial^2 \mathbf{E}(z)}{\partial z^2} + (k_0^2 - \beta^2)\mathbf{E} = 0$$

Although the equation's solution can be split into the Transverse Magnetic mode (TM) and the Transverse Electric mode (TE), only TM mode can be supported in this interface structure. This has been proved by applying the boundary conditions to both TM and TE mode equations. So, we can get TM solution as follow:

For upper part $z > 0$,

$$H_y(z) = C_2 e^{i\beta x} e^{-k_2 z}$$

$$E_x(z) = iC_2 \frac{1}{\omega \varepsilon_0 \varepsilon_2} k_2 e^{i\beta x} e^{-k_2 z}$$

$$E_z(z) = -C_2 \frac{\beta}{\omega \varepsilon_0 \varepsilon_2} e^{i\beta x} e^{-k_2 z}$$

For lower part $z < 0$,

$$H_y(z) = C_1 e^{i\beta x} e^{k_1 z}$$

$$E_x(z) = -iC_1 \frac{1}{\omega \varepsilon_0 \varepsilon_1} k_1 e^{i\beta x} e^{k_1 z}$$

$$E_x(z) = -C_1 \frac{1}{\omega \varepsilon_0 \varepsilon_1} k_1 e^{i\beta x} e^{k_1 z}$$

k_1 and k_2 are the z wave vectors and are a real positive value. Both the upper and lower part, the expressions contain $e^{\pm k_j z}$ ($j = 1,2$), which makes the electric field exponentially decay along the z-direction.

Applying the boundary condition: $H_{y,upper}(z = 0) = H_{y,lower}(z = 0)$, $\varepsilon_j E_{z,upper}(z = 0) = \varepsilon_j E_{z,lower}(z = 0)$, j=1,2 at the interface z=0, so:

$$C_1 = C_2$$

$$\frac{k_2}{k_1} = -\frac{\varepsilon_2}{\varepsilon_1}$$

This condition can only be fulfilled when ε_1 and ε_2 have opposite signs. The dielectric has an almost constant positive permittivity $\varepsilon_2 > 0$, while for metals it can be negative when the frequency is close to but still smaller than ω_p, since $\varepsilon_1(\omega) = 1 - \frac{\omega_p^2}{\omega^2}$. Here:

$$k_1^2 = \beta^2 - k_0^2 \varepsilon_1$$

$$k_2^2 = \beta^2 - k_0^2 \varepsilon_2$$

Finally, the dispersion relation can be achieved:

$$\beta = k_0 \sqrt{\frac{\varepsilon_1 \varepsilon_2}{\varepsilon_1 + \varepsilon_2}} = \frac{\omega}{c} \sqrt{\frac{\varepsilon_1 \varepsilon_2}{\varepsilon_1 + \varepsilon_2}}$$

The propagation mode achieved in the metal-dielectric interface structure, coupling the photon with the plasmon, is called the Surface Plasmon Polariton (SPP). As shown in the figure, electrons oscillate collectively which creates density wave. It is coupled with the external EM wave and propagates along the metal-dielectric interface. Due to the large propagation constant β, the EM wavelength is larger than the light propagating only in the upper dielectric. On the other

hand, the equations above imply that x wave vector β is larger than the total wave vector k_0, making z direction wave vector imaginary. Therefore, the electric field distribution along z-direction is exponentially decayed. The large difference of the $\beta^2 - k_0^2\varepsilon_j$ (j=1,2) gives large decay constants k_1 and k_2, which gives a rapid drop in electric field distribution along the z-direction. This gives us the subwavelength scale of the light confinement and can be used as a small light source.

The figure shows the dispersion curve for light propagate in air, silica and metal-air surface, where frequency ω is plotted as a function of propagation wave vector β. For dielectrics like air and silica, the frequency is a linear function of the wave vector. Their slops are constants which are decided by $v = c/n$, n is refractive index and v is the phase velocity. At low-frequency region, dielectric-metal SPP dispersion curve is very close to the dielectric dispersion line which can be understood from their relation $\beta = \frac{\omega}{c}\sqrt{\frac{\varepsilon_1\varepsilon_2}{\varepsilon_1+\varepsilon_2}}$ and $\varepsilon_1(\omega) = 1 - \frac{\omega_p^2}{\omega^2}$ where ω is small. The delocalization of the SPP modes at low frequency leak their EM field into the dielectric, and therefore these modes look like propagating in the corresponding dielectric with weakly bound to the metal. However, due to this nonlinear relation, ω approach to the asymptote line $\omega = \omega_{sp}$ as wave vector goes to infinity $\beta \to \infty$. In this case, SPP mode has strong bound to the metal, where less EM field leak into the dielectric. ω_{sp} is the surface plasmon frequency:

$$\omega_{sp} = \frac{\omega_p}{\sqrt{1+\varepsilon_2}}$$

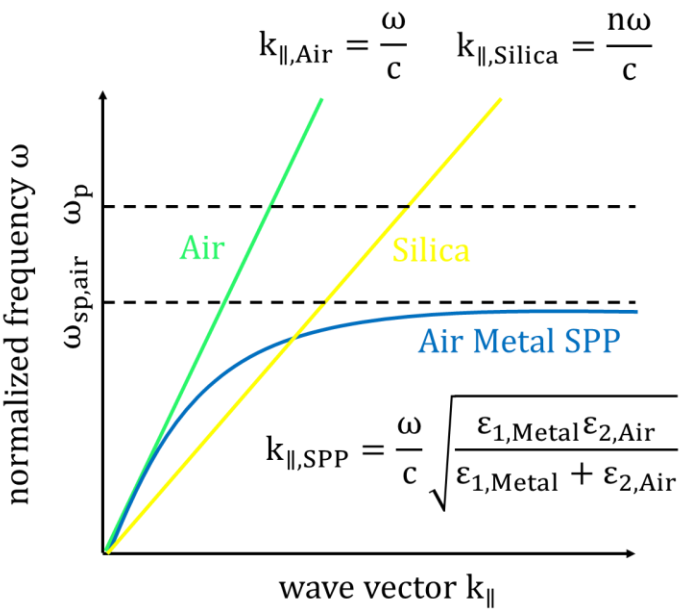

Figure 1. 13 The dispersion curve for light propagating in the Air, the Silica and between the Air-Metal interface as SPP. As shown in the figure, the SPP curve is always to the right of the air curve, which gives a larger propagating momentum. On the other hand, for some frequencies of light, the SPP curve is to the left of the silica curve.

Due to this nonlinear dispersion nature, the dielectric-metal dispersion curve always lies to the right of the corresponding dielectric dispersion line, which means for the same frequency SPP mode has larger propagation constant than dielectric mode as shown in the figure. So direct SPP excitation via coupling from dielectric into dielectric-metal is not possible due to the phase mismatching. For example in the left figure, direct excitation from air to air-metal SPP cannot be achieved, since the projection of the incident wave $k_x = k \cdot \sin(\theta)$ is smaller than β with an incident angle θ.

However, when the light is propagating in the silica, the propagating momentum is larger than that in the air, and as shown in the figure 1.13, for certain range of incident light frequency, the silica dispersion curve is to the right of the SPP curve. This means the light propagating in the silica can have larger momentum than SPP.

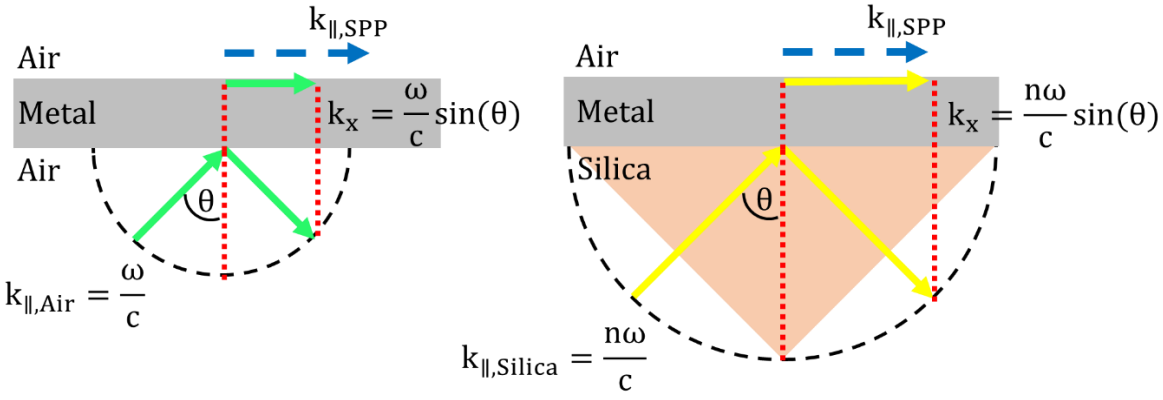

Figure 1. 14 Momentum matching. For light illuminates from the air onto the metal-air interface, the projection of the air light momentum is always smaller than the momentum of the interface SPP. On the other hand, for the light illuminates from silica onto the metal-air interface, the projection of the silica light momentum can equal to the SPP momentum, which makes it possible to satisfy the momentum matching and excite the SPP.

As shown in figure 1.14, when the incident light momentum is smaller than the SPP momentum at that frequency, the projection of the light momentum is always smaller than SPP momentum. Therefore, the momentum matching condition is not satisfied and it can not excite the SPP mode. However, when the light is propagating in the silica, due to larger refractive index n, the light momentum is larger than SPP momentum for certain frequency and its projection on the interface for certain incident angle can equal to the SPP momentum, which satisfies the momentum matching condition and excites the SPP.

The SPP modes above is between the two-dimensional interface as Kretschman geometry[38]. In the following chapter, the SPP modes in one-dimensional structure will be studied.

Chapter 2 Silver Nanowire-based SPM probe and Raman enhancement

2.1 Silver Nanowire (AgNW)

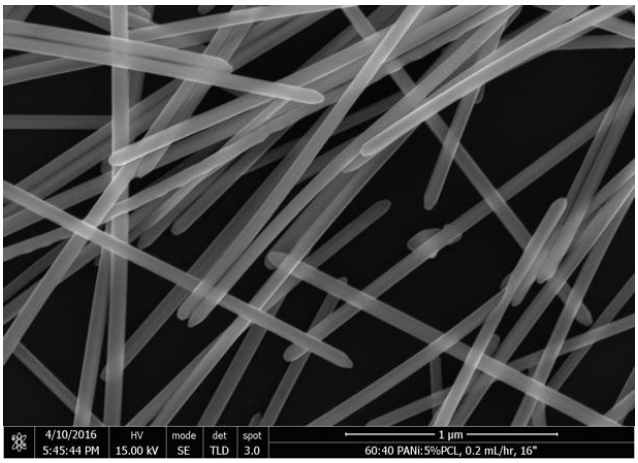

Figure 2. 1 Silver Nanowire bundle

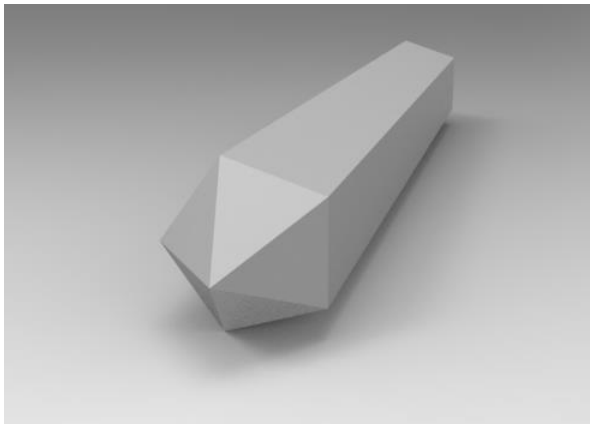

Figure 2. 2 AgNW: Pentagonal-shape atomic flat nanostructure.

Chemical synthesized Silver nanowire (AgNW) by polyol method is single crystal whose plasma frequency is in the visible light range. The diameters of AgNW is around 80 – 200 nm. The length of the AgNW is around 40 – 100 µm. AgNW has an atomic smooth surface for near zero

scattering loss. Due to its atomic-scale flat surface and small dissipation loss among noble metal, AgNW has been used as nanostructure for the SPP **coupling**, **guiding**, and **nano-focusing**. [39,40]

2.2 The AgNW-based SPM Probe

Chemically-synthesized single-crystalline silver nanowire (AgNW) probes can combine the scanning tunneling microscopy (STM) technique with tip-enhanced Raman scattering spectroscopy (TERS) for complementary morphological and chemical information with nanoscale spatial resolution. However, its performance has been limited by the blunt nanowire tip geometry, the insulating surfactant layer coating AgNW surfaces, and the thermal-induced mechanical vibrations. Here, we report a reproducible fabrication method for the preparation of sharp-tip AgNW-based TERS probes. By removing the polyvinylpyrrolidone (PVP) surfactant molecules from the AgNW surfaces for stable electrical conductivity and controlling the protruding length with μm-level accuracy for improved mechanical stability, we demonstrate atomic-resolution STM imaging with the sharp-tip AgNW probe. Furthermore, the sharp-tip AgNW has an excellent TER enhancement ($\sim 2.2 \times 10^5$), which is about 60 folds of that achieved by regular AgNWs. Our experiments demonstrate that AgNWs with clean interfaces and the proper tip geometry can provide reliable and reproducible STM and TER characterizations, which remove the hurdles preventing the implementation of AgNW in STM-based near-field optical applications for a broad community.

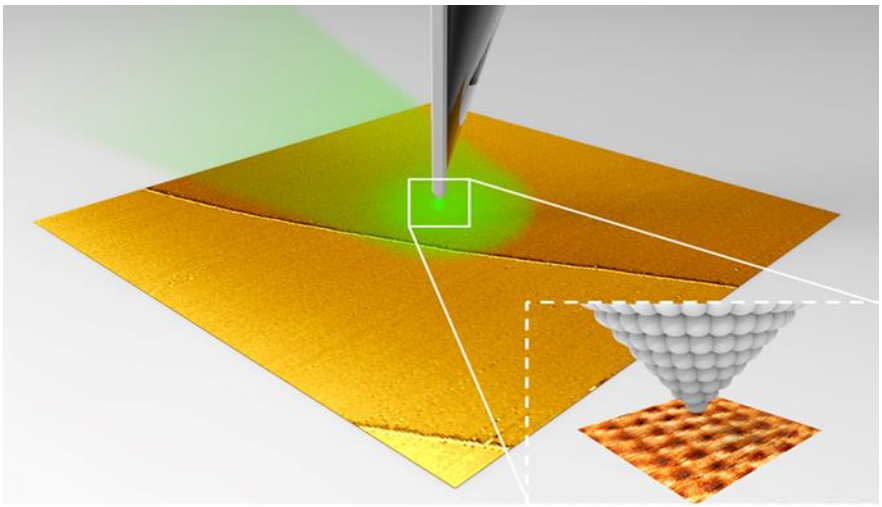

Figure 2. 3 Schematic illustration of using a sharp-tip silver nanowire probe for STM-TERS. Inset: An atomic-resolution image of HOPG surface acquired by the probe.

The techniques to acquire both topographical and chemical information with nanoscale spatial resolution have intrigued broad research interest, due to the increasing demands of such capability in nanotechnology and material science. Although topographical information can be readily acquired with high spatial resolution via conventional characterization tools including electron microscopy and scanning probe microscopy (SPM), mapping the chemical information at a similar scale remains challenging. Raman scattering vibrational spectroscopy is a powerful nondestructive technique for the investigation of the chemical bonding, composition, physical states and photon confinement of various types of materials. Integrating Raman spectroscopy with SPM techniques[41] has been demonstrated to break the optical diffraction limit that restricts the spatial resolutions of the conventional Raman imaging. This integration leads to the development of the tip-enhanced Raman spectroscopy (TERS)[42] imaging technique, which combines the high spatial resolution of SPM with the surface-plasmon-enhanced Raman signal through the use of a sharp metal tip[43-45]. As a result, the quality and reproducibility of TERS images profoundly rely on the morphology and the plasmonic enhancement factor of the metallic probes. The probe-preparation techniques have been at the heart of TERS imaging.[45-51]

Ever since its first experimental demonstration in 2000[41,45,52], a number of probe preparation methods have been developed for TERS measurements, including metal deposition on conventional AFM probes[46,47] and the electrochemical etching of metal needles[48]. Various illumination methods, such as bottom-illumination[53], side-illumination[54], and top-illumination[55] methods, have been examined and enhancement factors (EF) between 10^2~10^4 have been reported on numerous samples including organic dyes[56], low-dimensional materials[57], and biological molecules[58]. However, it remains challenging to prepare high-performance probes with reasonable reliability and consistency with these methods[49-51], which have become a major obstacle against TERS applications.

Recently, the AgNW synthesized by polyol process[59] has been considered as a promising candidate for reliable TERS probe preparation, due to its high synthesis yield, outstanding plasmonic performance[60-63], and excellent mechanical properties[64] for SPM applications. By assembling AgNWs with conventional cantilever probes, high-aspect-ratio AFM probes have been demonstrated[65]. The plasmonic hotspot supported by the AgNW tip is also expected to be suitable for TERS measurements with high spatial resolution and sensitivity, in particular when STM is employed. However, the practical implementation of AgNWs for STM-TERS imaging is facing three major obstacles. Firstly, polyvinylpyrrolidone (PVP) molecules, an essential surfactant used for the one-dimensional growth of AgNWs[66], form an electrically insulating layer on the AgNW surface and hinder the charge transfer processes, including the charge transfer from the STM electrode to the AgNW probe and from the AgNW probe to the sample substrate. Secondly, most AgNWs synthesized by the polyol synthesis have round or even flat tip shapes[67] due to the oxidative etching during the sample synthesis and storage, which decrease both the STM and the TERS resolutions. Lastly, the common method to prepare AgNW probes utilizes the alternating current-dielectrophoresis (ac-DEP) force to attach AgNWs onto metallic tips[50,51,61], which tend have long

protruding AgNW regions since the attaching locations are random. The long protruding length leads to large vibrational noises and cannot provide atomic resolution imaging. Moreover, the ac-DEP method requires the surfactant coating layer on AgNWs to maintain their dispersion in solution, resulting in poor electrical conductivity in the prepared probes that are not suitable for STM imaging. In this work, we investigate the influences of the surfactant layer, the AgNW tip shape, and the protruding length on STM imaging quality (Figure 2.3). We also report a reliable TERS probe fabrication method which utilizes a micromanipulator to mount a sharp-tip surfactant-free silver nanowire (AgNW) onto a tungsten probe with μm accuracy. By comparing the performance of sharp-tip AgNWs with regular ones, we prove that the Raman enhancement factor can be improved by 60 folds on a monolayer graphene sample.

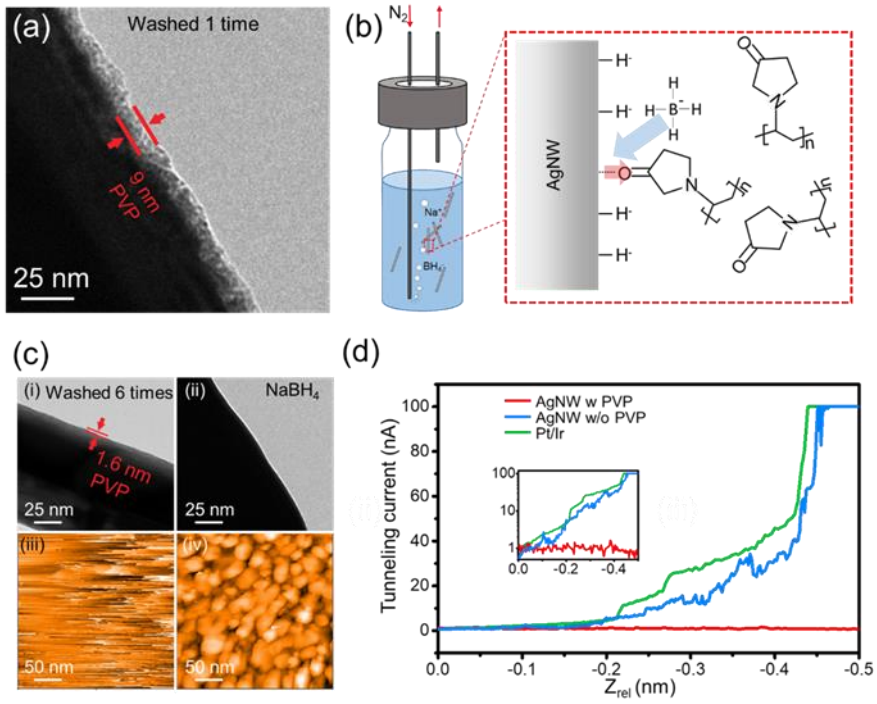

Figure 2. 4 Removal of surfactant molecules from AgNW surfaces and its impacts on STM imaging. (a), TEM confirms that the as-prepared AgNWs are coated by a thin layer (~9 nm) of PVP molecules, which serve as the surface surfactant during the salt-mediated polyol process. (b), Schematic illustration of the surfactant removal process. Nitrogen bubbles are generated to stir

the $NaBH_4$ solution while maintaining the N_2 environment to avoid the oxidation of AgNWs. Inset: the detachment of PVP from Ag surface by hydride generated from the boron hydride. (c), Comparison of AgNWs prepared by the conventional cleaning method (6 times of washing with ethanol, inset i) and the NaBH4 cleaning method (inset ii). The conventional method leaves ~ 1.6 nm of PVP residues that result in a poor STM image quality as shown in (iii). AgNWs treated by $NaBH_4$ cleaning have PVP-free surface and can serve as STM probes for topographical imaging (iv). (STM conditions: -1V probe bias, -1 nA tunneling current). (d), Comparison of tunneling current variations as a function of the probe movement toward the substrate. (probe bias: -1 V)

Firstly, we examined the PVP layer thickness on AgNW cleaned with a conventional purification method using ethanol and centrifugation[51,68]. The TEM images show a significant reduction of PVP layer thickness after washing with ethanol for 6 times, as compared with the pristine AgNWs (Figure 2.4 a and 2.4 c-i). Additional washing cannot remove the PVP layer below 1 nm[68], even with rigorous vortex or sonication. On the other hand, oxidation of Ag arises due to the diffusion of the oxygen into the washing solution during the prolonged purification period. The PVP residues can significantly reduce the STM performance of an AgNW probe, by requiring high bias voltage (> 1V) to initiate the tunneling current, reducing the current-distance sensitivity and introducing the PVP molecule contamination during the scanning. Furthermore, as shown in the tunneling current characteristic at different probe-to-sample gap distance (Figure 2.4 d, red curve), there is no significant current change with the decrease of the gap distance when a PVP-coated AgNW is used, due to the blockage of the thin PVP layer (~1 nm). Tip cleaning process using high voltage pulses (5V) may partially remove the PVP molecules from the AgNW apex, but no measurable improvement on the scanning results was observed. This may originate from the difficulty in removing the long-chain PVP molecules (~55k in molecule weight) attached at the proximity of the tip apex, which can be dragged into the gap by the sample substrate during the scanning process and influence the tunneling current. The low current-distance sensitivity results in poor STM imaging quality on a gold substrate (Figure 2.4 c iii). To fully remove the PVP residues

left by the regular purification method, we used the sodium borohydride ($NaBH_4$) solution that has been demonstrated as an efficient adsorbate stripper for various chemicals, including organothiols, rhodamine, and PVP, from metal surfaces via the hydride of the absorbate.[69,70] To avoid the fast oxidation of fresh silver surfaces, which is within hours in water without the protection of a PVP layer, we conducted the purification process in deoxygenated $NaBH_4$ solution purged and stirred by bubbles from high-flow-rate nitrogen gas, as shown in Figure 2b. This PVP removal method prevents oxidation of the AgNW after the complete desorption of the PVP layer from the nanowire surface and the vigorous stirring with the nitrogen bubbles accelerates the desorption of the PVP layer. Complete removal of the PVP layer from the surface of AgNW was confirmed with TEM images (Figure 2.4 c-ii) and the significant improvement in current-distance measurement was achieved (Figure 2.4 d, blue curve). After the thorough purification, the AgNW probe has the similar current-distance characteristic as a freshly prepared platinum/iridium (Pt/Ir) probe (Figure 2.4 d, green curve), indicating that the PVP residues are reduced to a negligible level. It is worth noting that the work functions obtained for both Ag and Pt/Ir are significantly smaller than other experimental values, which may due to the surface contamination of the sample substrate under the ambient condition[71]. The STM scanning result of an Au film using the PVP-removed AgNW probe clearly shows the grains of deposited gold, as shown in Figure 2.4 c iv.

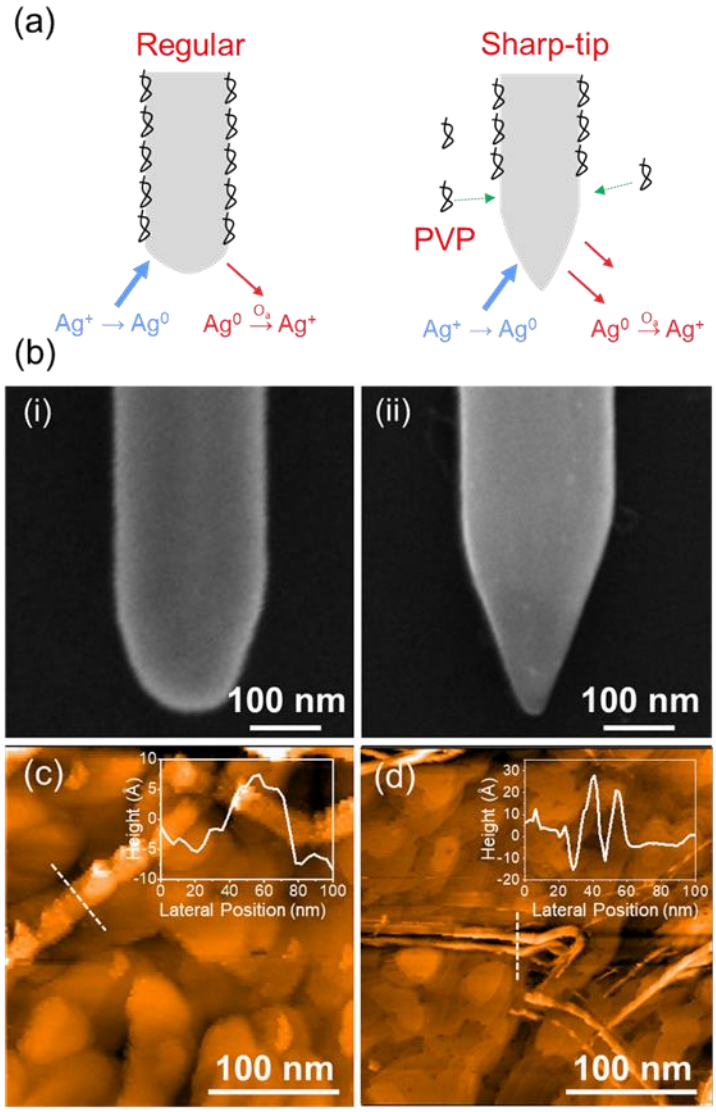

Figure 2. 5 Influence of AgNW tip radius on STM scanning. (a), Schematic illustration of AgNW sharpening process by controlling the AgNW growth, oxidative etching, and PVP passivation rates occurring at the tip of AgNW. (b), SEM images of AgNW produced by the regular polyol synthesis method and the sharp-tip nanowire synthesis method. The AgNW probes in (i) and (ii) are used to get scanning results on an SWCNT sample, shown in (c) and (d), respectively. Insets: the cross-sectional profiles along the dashed lines. STM conditions: probe bias -200 mV, tunneling current -0.4 nA.

The shape of an AgNW tip can significantly influence the STM quality. AgNWs synthesized with conventional polyol process through the salt-mediated agents have rounded or

even flap tip shape as shown in Figure 2.5 b-i, originating from etching in the existence of oxygen and Cl^- during the synthesis[72]. The multi-channel effect occurs when blunt-tip AgNWs are used, resulting in low spatial resolutions and ghosting images. Figure 2.5 c shows the STM scanning image of single-walled carbon nanotubes (SWCNTs) dispersed on an Au film, using an AgNW probe with round tip geometry. The cross-sectional analysis reveals that a 1.4nm-in-height SWCNT bundle has a width of 34 nm, which is overestimated due to the blunt AgNW tip shape. In order to reduce the tip radius, a modified copper chloride-mediated polyol method has been exploited for sharp-tip AgNWs[65]. By increasing the growth rate to faster than the PVP passivation rate (Figure 2.5 a), AgNWs with conical tips could be synthesized. The sharp-tip AgNW with a small tip radius ~5 nm can provide a much finer STM resolution on the same SWCNT sample (Figure 2.5 d). In particular, the sharp tip allows to image trenches such as the gaps between CNT bundles (inset of Figure 2.5 d). It also enables a drastic enhancement of the TERS performance which is discussed in the following section.

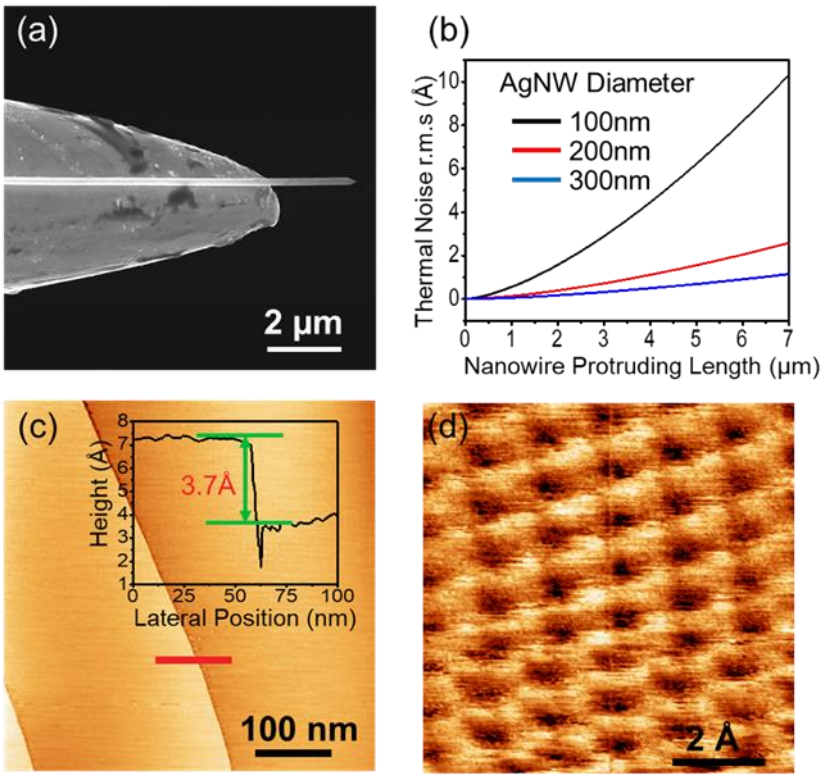

Figure 2. 6 Atomic-resolution STM images obtained by the sharp-tip AgNW. (a), SEM image of the AgNW probe mounted on a tungsten tip. The protruding length of AgNW is 2.3μm. (b), Thermally induced vibration under different nanowire diameters (100, 200, and 300 nm). (c), The STM image of HOPG shows a clear and accurate vertical resolution of monoatomic layer. Inset: the cross-sectional profile of the red solid line. (d), Atomic-resolution STM image of HOPG. (Probe bias -50 mV, tunneling current -1 nA).

Besides the PVP insulating layer and the AgNW tip radius, another determining factor for high-quality STM imaging is the vibration of the nanowire, which can be attributed to acoustic pressure-induced vibration and thermally induced vibration. The acoustic noise level in a quiet room is around 20~40 dB and reaches ~60 dB in a research laboratory, generating a root-mean-squared (r.m.s.) displacement on the free-standing AgNW that can be estimated by the Euler-Bernoulli beam theory[73],

$$\langle r.m.s_{acoustic} \rangle = \frac{qL^4}{\sqrt{2} \cdot 8EI} \quad (1)$$

where q is a uniform distributed load per unit length, L is the length of the nanowire, E is the modulus of elasticity, which is reported ~90 GPa for AgNW[74], and I is the area moment of inertia for a cylindrical cantilever. q can be estimated by $q = P \cdot a$, where P is the acoustic pressure and a is the nanowire diameter. The acoustic noise level (L_P) measured in dB is defined by

$$L_P = 20 \frac{P}{P_0} \ (dB) \quad (2)$$

where P_0 is reference acoustic pressure (20 μPa). For a typical AgNW with the diameter between 100~300 nm, the free-standing protruding region must be shorter than ~ 20 μm in order to have the acoustic vibration amplitude less than 1 Å under 60 dB environmental noise.

The thermal fluctuation of an AgNW can be estimated according to the equipartition theorem. Every independent quadratic term of a cantilever oscillator system in the thermal equilibrium has a mean value of $\frac{1}{2}k_B T$, where k_B is the Boltzmann constant and T is the absolute temperature. A cantilever with a spring constant K and mean square deflection $\langle x^2 \rangle$ has a potential energy of $\frac{1}{2}K\langle x^2 \rangle$ where K is given by $K = \frac{3EI}{L^3}$. The equipartition theorem gives $\frac{1}{2}k_B T = \frac{1}{2}K\langle x^2 \rangle$ which can be used to estimate the amplitude of the thermally induced root-mean-square oscillation of a cantilever with a free end:

$$\langle r.m.s_{thermal} \rangle_{25℃} = 5.6 \times 10^{-3} \frac{L^{\frac{3}{2}}}{a^2} \text{ Å} \quad (3)$$

This equation is valid at 25°C, with a and L in the unit of μm. To achieve the atomic-resolution STM imaging, the protruding length of a 200 nm-in-diameter AgNW needs to be shorter than 3.7 μm to reduce the thermal noise level to less than 1 Å (Figure 2.6 b). For a narrower AgNW

with 100 nm in diameter, this protruding limit is decreased to 1.5 μm. Compared with the acoustic-pressure-induced vibration, the thermally induced vibration dominates in the AgNW-STM system.

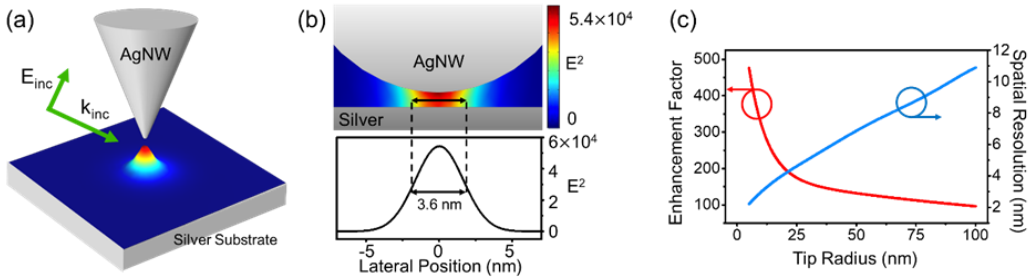

Figure 2. 7 Electromagnetic simulation of the localized surface plasmon resonance inside the gap formed by an AgNW tip and a metal substrate. (a), Simulation geometry schematic. Simulation conditions: tip radius ~15 nm, gap distance 1nm, excitation wavelength 532nm. (b), Zoom-in plot of the intensity ($|E|^2$) distribution at the gap region. Bottom: Intensity profile at the gap reveals a hotspot size of 3.6 nm. (c), Calculated results of field enhancement factor and hotspot size as functions of tip radius.

Precisely controlling the protruding length of an AgNW on a tungsten tip is consequently essential in suppressing the mechanical noise level for atomic-resolution STM imaging. Previous attempts using the ac-DEP force to attach AgNWs tend to have arbitrary protruding lengths between 10~100 μm since the adhesion locations induced by ac-DEP force are random. Here, we mount the AgNW onto a tungsten tip using a bench-top micromanipulator to realize the μm-accuracy control of protruding length. The length of the freestanding protruding portion of the AgNW can be adjusted by moving the AgNW along the tungsten tip and is shortened to less than 2 μm for the low-vibration-noise atomic-resolution STM imaging. Figure 2.6 a shows the SEM image of an AgNW-STM probe, using a 200 nm-in-diameter AgNW and 2.3 μm in protruding length, yielding around 0.5 Å thermal noise according to Eq. (3). To prevent the oxidation of the AgNW and reduce the acoustic noise, the STM scanning head is sealed in a helium chamber during the scanning. The corresponding STM images of a highly-oriented pyrolytic graphite (HOPG) sample taken under ambient conditions are shown in Figure 2.6 c and 2.6 d. Clear steps are observed within a 500 nm × 500 nm range scanning, with the cross section (Figure 2.6 c inset) showing approximately 3.7 Å step height that is close to the single atom layer thickness of graphite. The zoom-in scanning on a flat region of the HOPG in Figure 2.6 d illustrates the hexagonal structure of carbon atoms, which proves the capability of the prepared AgNW-STM probe for steady raster scanning with atomic resolution.

To gain insight on the TERS performance, we performed full-wave electromagnetic simulations using the finite element analysis (COMSOL Multiphysics 5.1) to assess the field enhancement factor, which is defined as the ratio between the electric field at the tip apex and that of the incident light ($EF_{field} = \frac{E_{tip}}{E_{inc.}}$), over a wavelength range from 400 to 800 nm. As illustrated in Figure 2.7 a, the 3D simulation geometry contains a silver conical probe vertically placed above

a silver substrate with 1 nm gap in between and is illuminated by a diffraction-limited laser beam with *p*-polarization from the side at 20° incident angle. Figure 2.7 b depicts the results of a conical tip (tip radius ~15 nm) excited by a 532 nm laser, which contains a strongly-enhanced highly-localized hotspot at the gap. The cross-section profile of $|E|^2$ reveals that the hotspot has a full width at half maximum (FWHM) of 3.8 nm, much smaller than the tip radius. We calculated both the enhancement factor EF (red curve) and the hotspot size (blue curve) as a function of the tip radius, as shown in Figure 2.7 c. As the tip radius decreases, the EF increases exponentially, while the size of the electric field FWHM decreases linearly.

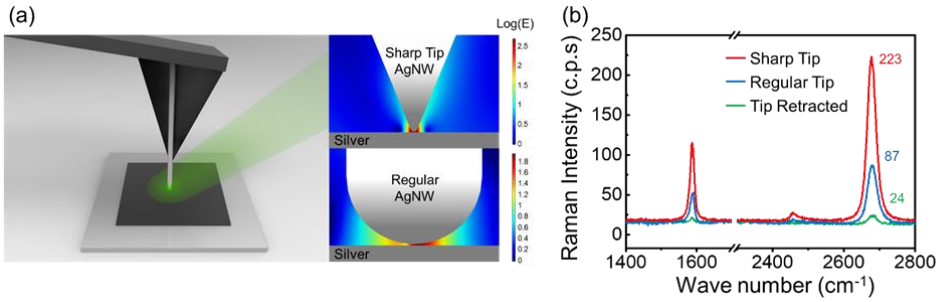

Figure 2. 8 Tip-enhanced Raman spectroscopy measurement. (a), The schematic of the sharp-tip AgNW for TERS measurement. The AgNW is mounted on an AFM cantilever. A monolayer graphene on an Ag substrate is used to evaluate the Raman enhancement factor. Inset images show the electric field distribution around a sharp-tip AgNW and regular rounded tip. (b), Raman spectra acquired by different AgNW tips. Laser specification: 532 nm in wavelength, 100 μW at the sample surface.

The Raman spectroscopy measurements were carried out in backscattering geometry using a commercial Raman spectrometer (Horiba Labram HR800), which is equipped with a motorized objective lens holder, a 600 grooves/mm grating, and a long-working-distance 100× with a numerical aperture (NA) of 0.6. The objective mounted on the motorized holder was dedicated to align the incident light (Laser Quantum Ventus, 532 nm, 100 μW at the sample) with the AgNW tip apex and collect the Raman scatterings, as depicted in Figure 6a. As a proof of functionality,

the TERS experiments were performed on a monolayer graphene sample, which was prepared on a copper film by the chemical vapor deposition (CVD) method and transferred on a silver substrate (50 nm in film thickness, deposited on a silicon dioxide wafer) using the PDMS-assisted transfer technique[75]. The surface roughness of the silver film is below 1 nm, which is low enough to suppress the surface-enhanced Raman scattering (SERS) process on the film. Figure 2.8 exhibits the TER spectra measured by a regular AgNW probe and a sharp-tip AgNW probe, in comparison with the Raman spectrum background without the probe launched (green curve). All TER spectra show intense spectral features that can be assigned to typical graphene phonon modes, in particular, the G-band at around 1580 cm^{-1} and the 2D peak at around 2680 cm^{-1}. The positions of the G and 2D peaks, the single Lorentzian shape of the 2D peak, the intensity ratio of the 2D to G peaks (~2), and the absence of the D peak (~1350 cm^{-1}) all indicate the high quality of the single layer graphene sample after the transfer process, which is suitable for the evaluation of the TER enhancement.

To estimate the field enhancement achieved with the AgNW probes, we calculate the Raman enhancement factor through the following equation[76].

$$EF_{Raman} = \frac{I_{NF}}{I_{FF}} \frac{A_{FF}}{A_{NF}}$$

(4)

which considers the normalized Raman intensity by dividing the intensity from the far-field (I_{FF}) and the near-field (I_{NF}) with the corresponding area (A_{FF} and A_{NF}), leading to the enhancement factor that is independent of Raman excitathe tion area. I_{FF} and I_{NF} can be obtained from the spectra in Figure 2.8 b. The area of excitation A_{NF} is estimated based on the numerical simulation in Figure 2.7, yielding around $A_{NF} = \pi \times (2.5\ nm)^2$ for the sharp-tip AgNW and $A_{NF} = \pi \times (12\ nm)^2$ for a regular AgNW probe. In contrast, the semi-minor diameter of the elliptical laser spot focused by the tilted objective lens (tilt angle ~20°) from the side is diffraction-limited to about

$d_{ex,minor} \approx 0.51 \times \lambda/NA \approx 450\,nm$, and the semi-major diameter is $d_{ex,major} \approx d_{ex,minor}/sin20° \approx 1300\,nm$. The illuminated area is therefore at least $A_{FF} = \pi/4 \times (450nm) \times (1300nm)$. The Raman enhancement factor can be estimated from eq. (4), which gives 2.2×10^5 for the sharp-tip AgNW probe, a 60-fold increment when compared with the regular AgNW (~3.7×10^3). Since the Raman intensity scales approximately with the electric field as $|E|^4$, the EF_{Raman} corresponds to electric field enhancement (EF_{field}) around 22 for the sharp-tip AgNW and ~8 for the regular AgNW. These values are similar to other sharp TERS tips prepared by pulling and electrochemical etching of gold wires[47] but requires much simpler fabrication.

To conclude, we demonstrate a reliable process for the reproducible fabrication of ultra-clean nanowire-based STM probes. The probes consist of a sharp-tip silver nanowire positioned on a regular metallic probe and can provide atomic-resolution STM imaging on a graphite lattice and topographical mapping of single-walled carbon nanotubes deposited on metal substrates. We confirm that the surfactant residues left on the AgNW surface after conventional cleaning treatment, the tip radius, and the thermal vibration from the protruding part of the AgNW are the major limiting factors for imaging resolution. The promising results imply that the micromanipulation method to assemble sharp-tip AgNWs on metallic tips for STM-TERS applications can be a reliable fabrication technique for a much simplified near-field Raman imaging research.

AgNW synthesis

AgNWs with round tips were synthesized via a modified salt-mediated polyol process. $CuCl_2$ was used as the salt-mediated agent to remove the adsorbed atomic oxygen efficiently from AgNW for less oxidative etching and fast growth[66]. 5 ml ethylene glycol was added in a pear-shaped flask with a stir bar and the flask was immersed in a silicone oil bath at 152 °C under magnetic stirring (400 rpm) for 15 minutes. While heating up the flask, 6 ml of 0.094 M $AgNO_3$

(99+%, Fisher) and 6 ml of 0.147 M PVP (avg Mw # 55 000, Sigma-Aldrich) in ethylene glycol (EG, 99%, Fisher) were prepared. 80 µl of 4 mM $CuCl_2$ (99.995%, Sigma-Aldrich) was added in the flask and the flask was heated for an additional 15 minutes. Injection of 3 ml of the PVP was conducted into the flask followed by the injection of $AgNO_3$ solution at the injection rate of 125 µl/min using two syringe pumps[67]. The injection continued for 40 mins and the flask was removed from the silicone oil bath and cooled at room temperature for 15 minutes. The synthesized AgNWs were purified with ethanol and centrifugation at 2000 RPM for 20 minutes 5 times. For the ultra-sharp AgNW, we followed the synthesis method described in Ref[65].

Removal of PVP layer from AgNW surface

AgNW in 3 ml of 4 mM $NaBH_4$ was added in a 4 ml glass vial with a septa cap and it was purged with nitrogen supplied with a syringe needle. After 1-hour purification, the solution was refreshed with a $NaBH_4$ solution and additional 1-hour purgation was conducted. When the removal process completed, aggregated AgNW could be observed in the solution. The AgNW aggregates were transferred to another clean 4 ml vial with ethanol. A gentle sonication was performed to disperse the AgNWs before using.

Au film and SWCNTs/Au

Au (100nm in thickness) was deposited on silicon substrates and freshly exfoliated mica layers using e-beam thermal evaporator at the deposition rate of 1Å/s. The Au film on a silicon substrate was directly used for the scanning of Au grains. For SWCNTs/Au samples, the ultrasmooth Au film was required, which was prepared by annealing Au/mica at 350 °C for 1 hour. The Au film was then mechanically peeled off by gluing the Au film onto to a silicon substrate. We sprayed SWCNTs (conductive aqueous ink, Sigma-Aldrich) on the Au film at 60 °C. Surfactants used for the dispersion of the SWCNTs in water was removed by immersing the

SWCNTs/Au in DI water which is refreshed by the continuous flow of DI water. The SWCNTs/Au sample was dried by blowing gently with a nitrogen gun.

STM scanning.

All the scanning images were acquired using a NaioSTM (NanoSurf) apparatus in a helium chamber.

2.3 Other AgNW based SPM Probe

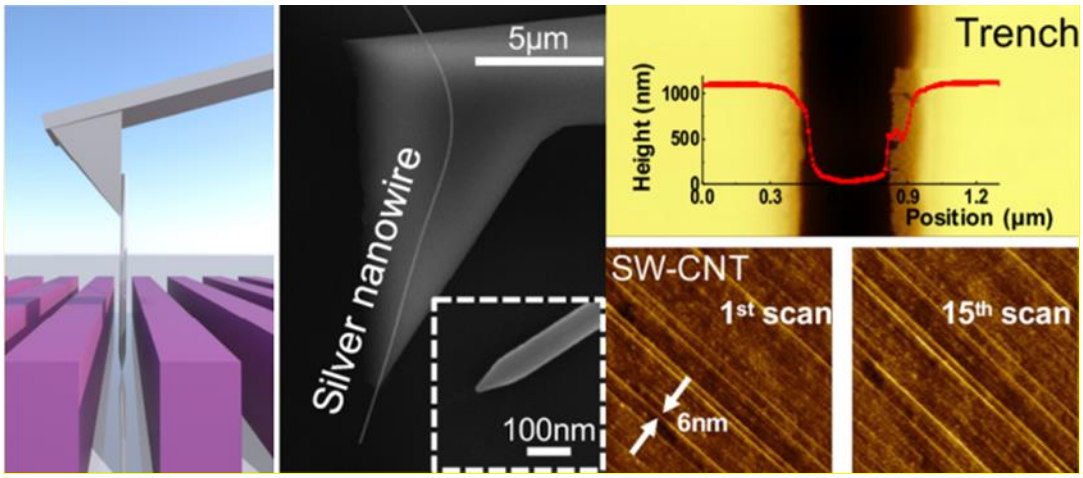

Figure 2. 9 AgNW based AFM probe[65]

In other experiments, we have proved that AgNW is a powerful tool for the SPM probe. Compared with bulk silver, crystalline AgNWs have improved mechanical properties. Strain-stress measurements have revealed that Young's modulus of AgNWs benefits from the stiffening size effect[77] and can reach 160 GPa[64,78]. By aligning the AgNW onto the conventional AFM cantilever, we have shown that the AgNW based AFM probe has good stability and can achieve high spatial resolution. Therefore by using AgNW for both STM and AFM, we have proved that AgNW is a reliable material for the SPM probe.

Chapter 3 The SPP Modes in the AgNW

3.1 The Optical Properties of AgNW: SPP Modes in the One-Dimensional AgNW Structure

Various types of metallic nanostructure have been developed to conducted SPP wave. For example, the thin film, sharp metal wedges, chains of nanoparticles, metal strips and metal nanowire, nanogap, nano slot, and nano grooves etc. However, not all these nanostructures are capable of delivering and concentrating light into nanoscale. Some of them exhibit strong dissipation, some of them have weak spatial confinement, and others may require complicated fabrication process. The nanowire may be sensitive to the surface roughness which might cause scattering loss and short propagation length could be achieved. Chemical synthesized Silver nanowire (AgNW) by polyol method is single crystal whose plasma frequency is in the visible light range. Due to its atomic-scale flat surface and small dissipation loss among noble metal, AgNW has been used as nanostructure for the SPP coupling, guiding, and nano-focusing. [63,79-87]

For the SPP excitation, the prism coupling which is similar to the Kretschman geometry has been employed to compensate the wave vector mismatch. In this structure, the AgNW is placed parallel onto a tapered angle optical fiber at the tip region. The regular length of the AgNWs is in the range $[40\mu m - 70\mu m]$. The protruding length of the AgNW is around $[2\mu m - 5\mu m]$. The tapered angle of the optical fiber is around $6°$. Light is guided from the optical fiber to its tip. Due to the large overlapping between the optical fiber tip and the AgNW, SPP modes in the AgNW can be excited from the evanescent coupling.

For the SPP guiding, due to atomic scale flat surface and relatively low dissipation for visible light, the AgNW provides a better propagation length comparing with other nanomaterials and nanostructures.

To utilize the AgNW as an SPP waveguide, the SPP modes in AgNW should be studied. The field distribution of the eigenmode support by cylindrical nanowire can be expressed as:

$$E_m(r, \phi, z) = A_m R_m(k_\perp r) e^{im\phi} e^{ik_\parallel z}$$

The solutions can be shown in the figure. For m=0, it is the lowest mode. Since it is a transverse magnetic mode, so it is called TM_0. This mode has radial electric field distribution, and maintain zero in the center, so its electrical field has a ring shape.

On the other hand, for m=1, the second lowest mode, since it has both electric and magnetic components in propagating direction, so it is a hybrid mode. Because the electric field is larger than the magnetic field, so it is called HE_1. This mode has dipole like electric field distribution, all the electric fields are pointing to the same direction.

There are also higher order modes supported by the one-dimensional structure, HE_2 HE_3… For the AgNW diameter from 80 -200 nm, they are not supported and in this work, only TM_0 mode and HE_1 mode are considered.[88,89]

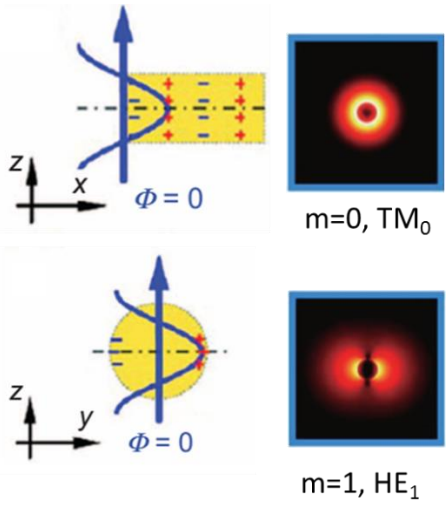

Figure 3. 1 Two lowest SPP modes in AgNW. [90]

$$n_{eff} = \frac{k_{\parallel}}{k_{air}}$$

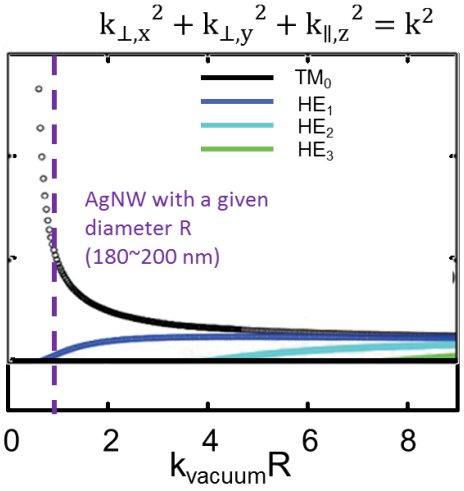

Figure 3. 2 Mode effective index as a function of AgNW diameter.[89]

As shown in figure 3.2, the refractive index of different modes are a function of AgNW diameters R. As R approaching to zero, mode 0 refractive has 1/R dependence and goes to infinitely large. For higher order mode, they are either cut-off or getting close to 1.

Such relations indicate that the propagating wave vector increase for m=0 and generate large imaginary part of vertical momentum. Which means there is strong decay perpendicular to

the propagating direction. This gives strong confinement of the SPP and provides very high resolution. The propagating wave vector for m=1 getting close to 1 which is the refractive index of air. So the vertical momentum is near-zero imaginary value, which gives weak confinement of the mode. This means the m=1 mode is a leaky mode and widely spreads into the neighbor dielectric. In a simple word, for high resolution, only mode m=0 is needed. m=1 and other higher order modes will decrease the resolution.

For the SPP excitation, the prism coupling which is similar to the Kretschman geometry has been employed to compensate the wave vector mismatch. In this structure, the AgNW is placed parallel onto a tapered angle optical fiber at the tip region. The regular length of the AgNWs is in the range $[30\mu m - 70\mu m]$. The protruding length of the AgNW is around $[5\mu m - 10\mu m]$. The tapered angle of the optical fiber is around $6°$. Light is guided from the optical fiber to its tip. Due to the large overlapping between the optical fiber tip and the AgNW, SPP modes in the AgNW can be excited from the evanescent coupling. [91]

For the SPP guiding, due to atomic scale flat surface and relatively low dissipation for visible light, the AgNW provides a better propagation length comparing with other nanomaterials and nanostructures.

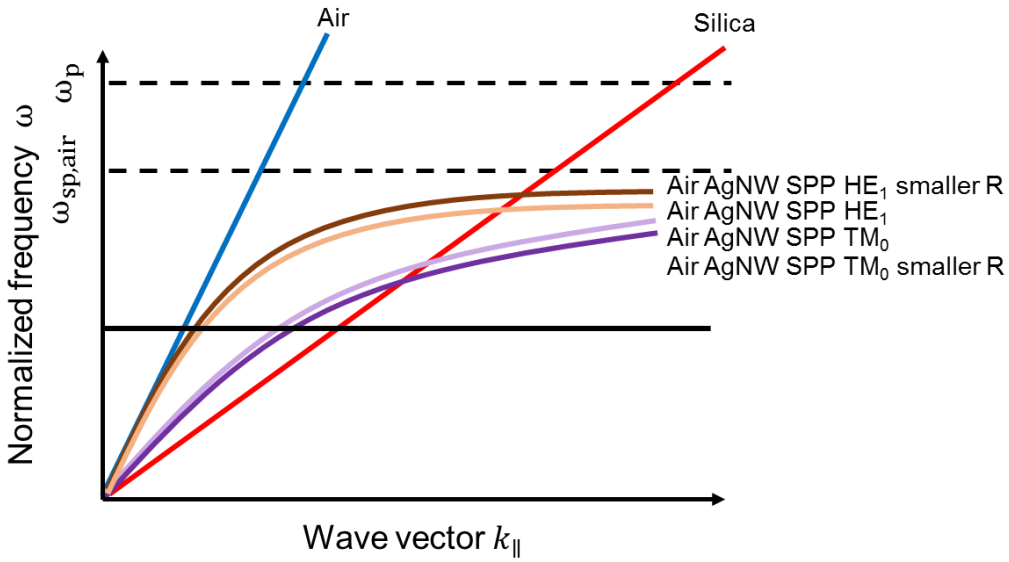

Figure 3. 3 Dispersion curve for different AgNW SPP modes and diameters.

However, as shown in figure 3.3, for different SPP modes with different AgNW diameters, the Kretschman geometry has the chance to excite both m=0 and m=1 modes for the same frequency. TM_0 provides high resolution but HE_1 doesn't. To selectively pick out the TM0 mode and focus it to the tip of AgNW is the core of our design.

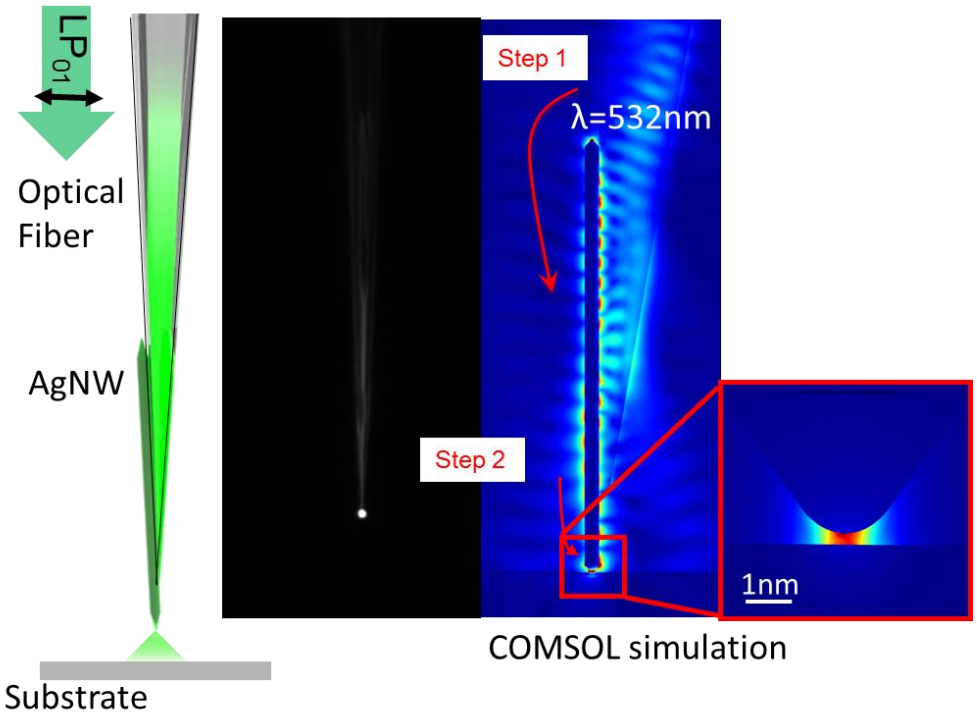

Figure 3. 4 Two-step nanofocusing technique

3.2 Two-step Nanofocusing Technique

A two-step nanofocusing technique has been developed to selectively coupling light from the optical fiber into AgNW TM_0 mode has been developed as shown in figure 3.4. As the light propagates to the tip of the optical fiber, it will be first selectively coupled into TM_0 mode. And then the mode will be adiabatically focused to the tip of AgNW.

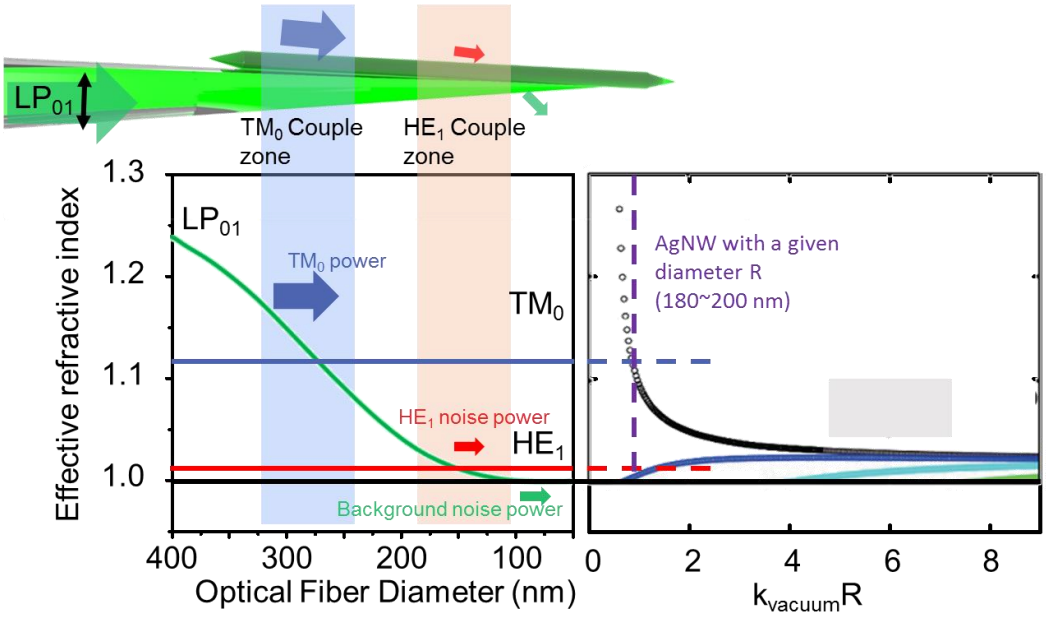

Figure 3. 5 Two-step nanofocusing technique

As shown in the figure, when the diameter of the AgNW is given, it will support TM_0 and HE_1 with different effective refractive index. The effective index of the TM_0 is always larger than HE_1. As the diameter of the optical fiber core part decreases smaller than the wavelength scale, its effective mode index starts to decreases and will finally approach to one which is the refractive index of the air. During the decrease of fiber refractive index, its value will have cross point with both TM_0 and HE_1 refractive index. This will create two coupling zone along the fiber separately. As calculated in the other simulation results, only the p-polarized light in the optical fiber can excite TM_0 mode.

Now a p-polarized gaussian shape linear polarized light LP_{01} illuminates into the fiber and approached to the end of the fiber. When it propagates into the cone shape zone of the fiber, it will meet TM_0 coupling first. By appropriate design of the optical structure, for example choosing fiber

tip angle around 6 – 8 degree, and appropriate diameter of AgNW, from 180 nm – 200 nm, we have the chance to couple most of the power into TM_0 mode. The rest of the light power will keep propagate and meet the HE_1 coupling zone. So only a small portion of light can couple into the HE_1 mode or scatter out from the fiber.

By physically separate the TM0 and HE1 mode coupling region, we can get the most power into TM0 and achieve super high resolution in the next step.

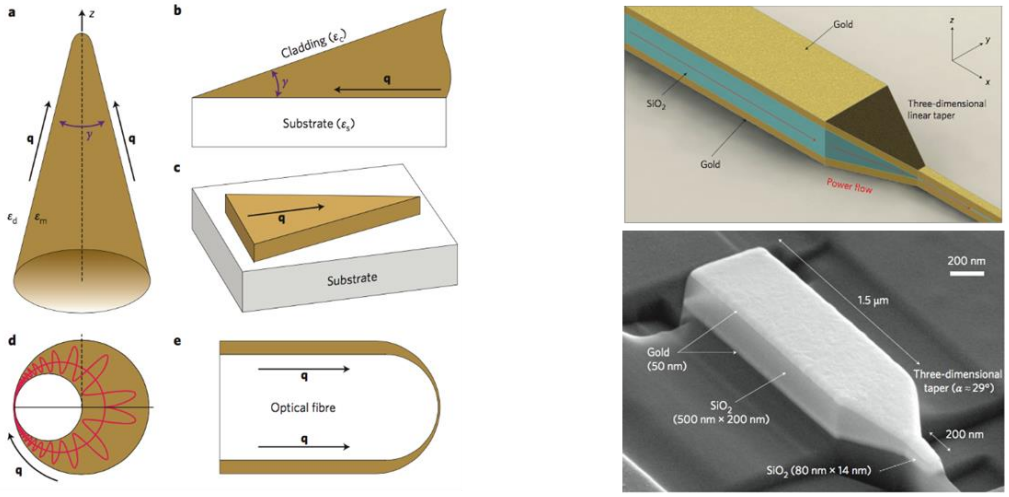

Figure 3. 6 Popular adiabatic nanofocusing structure.

In the second step, the TM_0 mode will be focused at the tip of the AgNW adiabatically. Figure 3.6 shows some popular nano design for adiabatic nanofocusing. However, these structures require complicated fabrications.

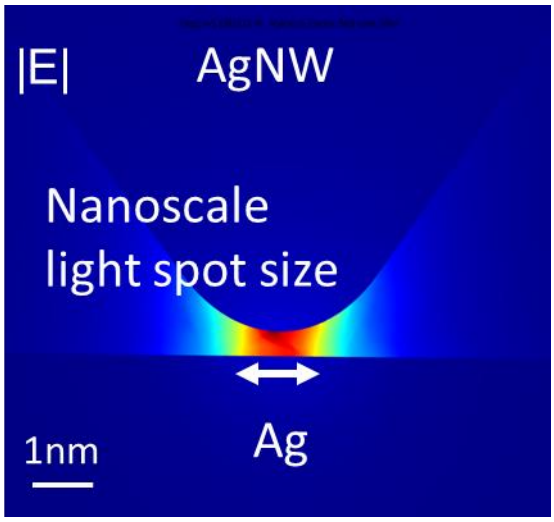

Figure 3. 7 AgNW adiabatic nanofocusing.

For the TM_0 mode of SPP nano-focusing, the AgNW tip radius can transform the propagating SPP into the localized surface plasmon adiabatically. In such adiabatic process, the tapered angle fiber tip changes its radius weakly, so the propagating SPP won't 'feel' the change of the environment. Imaging the SPP as a box of particles, the decreasing of the tip size equivalent to box size compression and doing work on particles. However, if the compression is sufficiently slow, the work can be ignored which means there is almost no external force applies on these photon particles. Therefore, there is no significant reflection of the SPP in this adiabatic process.

It has been proved that as the propagating SPP approaches to the tip with a tapered angle, the SPP's phase and group velocity tend to zero asymptotically. As a consequence, the SPP tends to stop and its wavelength tends to approach zero asymptotically as it gets close to the tip. Without significant energy loss due to reflection, the AgNW tip accumulates energy from photon where the SPP tends to stop. Therefore, the local EM field is dramatically enhanced by 3 orders due to its three-dimensional energy concentration. AgNW can tightly confine the mode into a nanoscale spot.[92,93]

Please notice that using a tapered angle optical fiber along without any metal cannot confine and enhance EM field. It has been measured that as the radius of tapered angle optical fiber decreases, the EM field will leak out from the fiber and distribute in the air. There is neither mode confinement nor mode enhancement for the dielectric materials as long as their permittivity is positive.

3.3 The SPP Mode at the AgNW Tip

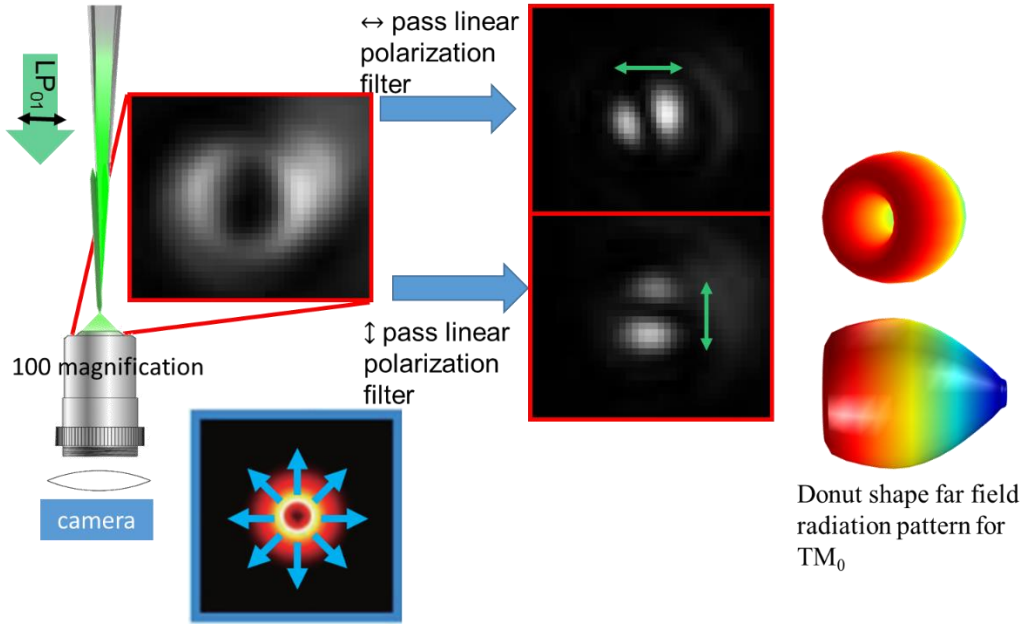

Figure 3. 8 TM_0 at the tip of the AgNW. The radiation of the TM_0.

The radiation pattern of the TM_0 at the tip of the AgNW has been studied. As shown in figure 3.8, the optical fiber with AgNW is placed perpendicular to the microscope lens. 100 magnification of the lens has been used to focus at the tip of the AgNW. A rind shape of light has been observed. To prove this ring shape is TM_0, linear polarization filter has been employed. Since the TM_0 has a radial pointing electric field, there should only one direction of light under the filter.

As shown in figure 3.8, the direction of the light field flows the polarization direction of the filter and proves that it is a radial distribution field.

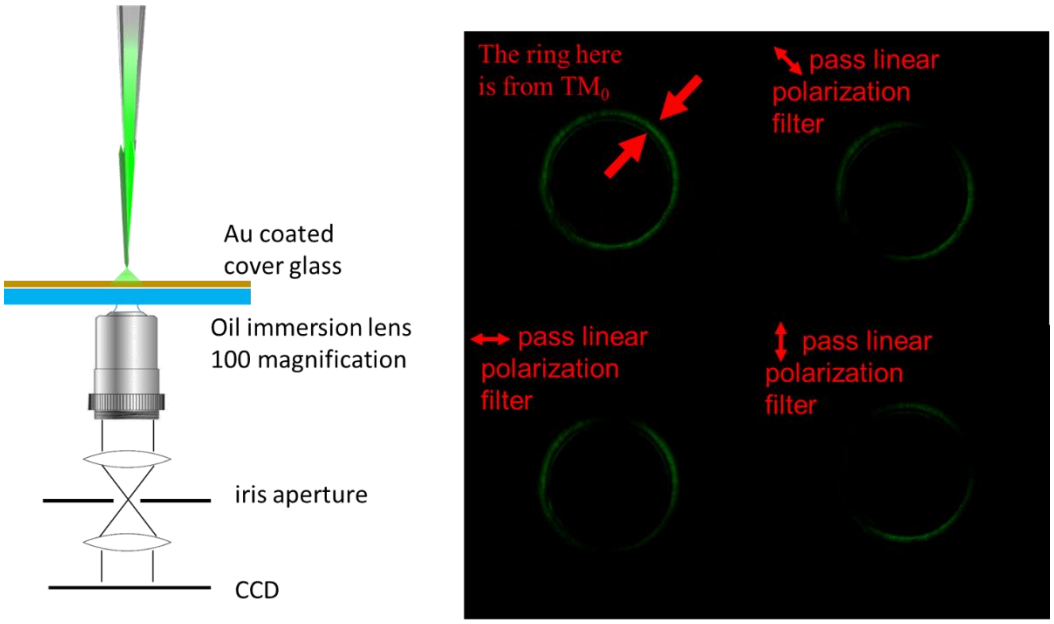

Figure 3. 9 TM_0 mode in the k-space.

K-space images of TM_0 mode are observed to further study the mode in the AgNW[94]. As shown in figure 3.9, a k-space imaging setup is used to capture the momentum distribution of TM_0 mode. The probe is landed onto a 30 nm gold coated cover glass. A 100 magnification oil immersion lens is employed to collect the light from the tip. The results show that a board ring from TM_0. Due to the uncertainty principle, a tightly confined mode at AgNW tip in real space results in a board ring in k-space. This ring maintains the radial polarization. When a linear polarized filter is applied to the light pattern, the light flows the direction of the filter.

Now, the tapered angle optical fiber and the AgNW configuration provides the way to excite the SPP. The propagating SPP provides sub-wavelength light confinement. And the nano-

focusing accumulates photon energy and provides strong enhancement for the localized surface plasmon EM field. With these conditions, we are ready to prepare a light source, with nanometer scale strongly enhanced near-field light, and all the portions of the incident light are working as a signal.

Chapter 4 Tuning Fork based Tapping Mode AFM for AgNW based NSOM

4.1 Tuning Fork AFM System for AgNW based NSOM

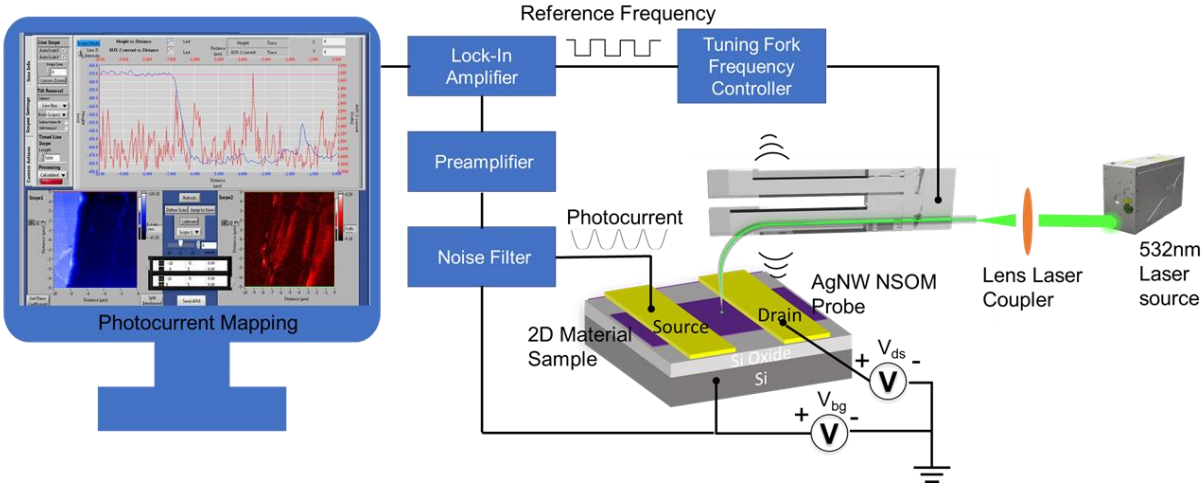

Figure 4. 1 Tuning fork AFM and NSOM photocurrent mapping system.

NSOM is a combination of SPM and optical spectrum. In chapter 2, we have proved that the AgNW can be used as an SPM probe. In chapter 3, we have studied the light along the AgNW, which is the AgNW SPP mode TM_0. We have proved that by using a two-step nanofocusing technique, we can achieve tightly confined light at the tip of AgNW and obtain a strongly enhanced nanoscale light source. Both the SPM and optical parts have been proved to have good performance. Therefore, a tapping mode AFM system is employed for this project, with an AgNW-based probe on it. As shown in the figure, a bent optical fiber is attached to the tuning fork and an AgNW is aligned on the tip of the optical fiber. The tuning fork oscillates with frequency around 32kHz. A laser is conducted along the fiber and coupled into the AgNW tip. The tip light spot is oscillating with the same frequency as the tuning fork above the two-dimensional sample. The sample is biased

with different channel and gate voltage. The modulated photocurrent in the sample is generated by the spotlight from the AgNW and collected in the circuit. Since the photocurrent is modulated by the tuning fork, a lock-in amplifier is used to lock the photocurrent with oscillation frequency and its higher order components. The mapping results will be analyzed together with the AFM results. [95]

4.2 The AFM Feedback System

Before talking about the probe preparation, tuning fork-based AFM will be introduced. Atomic Force Microscopy (AFM) is one type of Scanning Probe Microscopy (SPM). By using the atomic force change between the probe and the sample, it can scan and map the sample surface geometry by "touching" or "feeling" the surface with its probe. Commercial AFM system consists of a cantilever which is typically silicon or silicon nitride, a diode laser whose beam is reflected from the back of the cantilever and several photodiodes to catch and record the reflection beam. The cantilever has a sharp tip with a radius of curvature around a few nanometers. When the tip approaches close to the sample surface, forces between sample and tip lead to a deflection of the AFM probe which causes the reflection beam drift. This tip-sample interaction can be measured by monitoring the position of the reflected beam on photodiodes. The demonstrated resolution is on the order of fractions of a nanometer, which is more than 1000 times better than optical microscopy. However, by employing the laser beam, there might be interference between laser and signal from optical measurement. In some cases, the laser beam for cantilever deflection detection will scatter onto the sample, change its properties and induce unwanted signals. The external optical measurement devices also increase the complexity of the whole system. An alternative way to overcome these problems is employing a quartz tuning fork.[96]

A quartz tuning fork is an acoustic resonator, two prongs are connected at one end and form a U-shaped fork. When struck by an external force, it will resonate at a specific frequency which is defined by force gradient, material property, and its geometry. Using the piezoelectric effect of the quartz crystal, the mechanical motion of tuning fork can generate the electrical signal whose oscillation frequency, amplitude, phase are correlated to the external force. Thus the applied force can be measured according to its output electrical signal. Since only two electrodes are required for force measurement, the quartz tuning fork is easy to integrate into an SPM without any external optical device. Comparing with conventional Si cantilever, the quartz tuning fork has a much larger spring constant, which makes it sensitive to pico-newton force with low oscillation amplitude. All these properties make quartz tuning fork compact, robust and easy to operate.

The piezoelectric oscillation of quartz tuning fork can be modeled as an equivalent electrical LRC circuit, which is an impedance analogy. Since the only difference between tuning fork deflection displacement and charge separation is a real constant, the mechanical and electrical oscillations are in phase. Inductance L (inductor energy) is related to mass M (kinetic energy), while capacitance C (capacitor energy) is related to spring constant k (potential energy). A parallel shunt C_0 can be generated from the outside circuit. It smaller compare with the total impedance of the LRC circuit and can be neglected.[97,98]

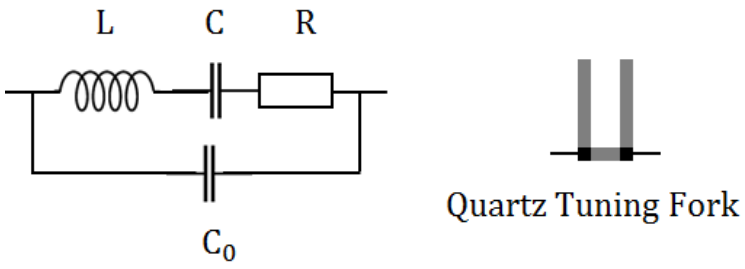

Figure 4. 2 Tuning fork acts as an LRC oscillation circuit.

In clock and watch, the quartz crystal tuning fork serves as timekeeping element in the form of a tiny tuning fork. Usually, by applying a small AC voltage from electric oscillation circuit to its metal electrodes, it was set to vibrate at the frequency of 2^15=32768 Hz. The tuning fork we are using now has the quality factor (Q factor) around 13000.

A configuration consists of the complicated multi-mass-spring model with two prongs mass m_1, m_2 and the base mass m_0 is used. Three vibration eigenmodes have been calculated. The most important one among them is the mode where two prongs vibrate against each other, whose frequency is 32768 Hz before symmetry broken. This mode has an extremely high Q factor compared with the other two modes. When the symmetry is broken, i.e. one of the prongs is attached with a probe and $m_1 \neq m_2$, its frequency shifts and undergoes strong additional damping from the base. Its Q factor drops quickly when the mass difference increase.

Since the minimum detectable force is $F_{min} \propto \sqrt{\frac{1}{Q}}$, increasing Q factor will increase the sensitivity and the scanning resolution. On the other hand, a high Q will restrict the detection response speed and the scanning speed. Therefore there is a trade-off between fast speed and high resolution. Hence, the way to mount the probe onto the tuning fork is critical to control the Q factor.

Depending on the probe-sample distance, there are 3 types of AFM modes. When the probe is far from the sample, the AFM operates in non-contact mode. When the probe brought close to the sample, the AFM operates in tapping mode, when the AFM probe and sample are always in contact, it is operating in contact mode.

With different types of tip oscillation modes, there are 2 types of mounting methods:

Shear force mode: By mounting the straight optical fiber parallel to the prongs, the tip will oscillate parallel to the sample surface. In the shear force mode, the probe will operate in non-

contact mode. When the probe is close to the sample, the vibration amplitude and phase will change due to the increase of attractive force. By monitoring its phase change, the sample surface geometry can be achieved. However, due to the large distance between probe and sample for non-contact shear force mode, the spatial resolution is limited to tens nanometer.

Tapping mode: by mounting the bent optical fiber on the sidewall of the prongs, the tip will oscillate perpendicular to the sample surface. In the tapping mode, the probe will operate in tapping mode. When the probe is close to the sample, the vibration amplitude and phase will change due to the tip-sample interaction. By monitoring its phase or amplitude change, the sample surface geometry can be achieved. Furthermore, due to its large spring constant of approximately 20,000 N/m, the tuning fork tines allows the use of small oscillation amplitudes as small as 0.1nm, offering a potential improvement for high spatial resolution techniques.

In this experiment, our probe is based on tapping mode bend fiber mounted on tuning fork. The bent fiber is used for both AFM force probing and NSOM light conducting. The attached fiber will induce mass different, however, by carefully designed fiber shape and gluing method, we can minimize the asymmetry effect and keep a relatively high Q factor around 9000. This will be discussed in the following chapter.

During scanning, the sample spatial information will be recorded as the probe's electrical signal frequency, amplitude, phase excursions. Depending on different purposes, these output signals will be fed back to the tuning fork, mixed with the driving source to excite the probe.

Open-loop: a straightforward method to use tuning fork is to measure the amplitude or phase excursions caused by applied force from tip-sample interaction directly. Suppose an AC driving voltage is applied to the circuit, the vibration of the tuning fork should be $z(t) = A_0 * \sin(\omega_0 * t + \varphi)$. As the probe approaches the sample, A_0, ω_0 and φ will change. In another word,

the mechanical vibration's amplitude phase and frequency will change due to the interaction between the probe and the sample. And the same thing happens to their output electrical signals. For the open-loop method, it will take mechanical settling time $t_{ring} = 2Q/\omega_0$ for the probe to settle into a steady state. After entering the steady state, the tuning fork amplitude or phase drift will be measured to calculate the force between probe and sample. Our home-made tuning fork probe always has a high Q factor around 7000~9000 and central frequency around 32kHz, which means the settling time is usually around 500 ms. This waiting time is long and inefficiency for studying the sample geometry.

Closed-loop feedback: When the probe has approached the sample in the tapping mode range, there will be an attractive force applied to the probe, which is equivalent to a force gradient dF/dz applied to the probe. This effect is similar to the probe's spring constant being modified from k to $k + dF/dz$. And it will cause the tuning fork probe's resonant frequency to be changed since $\omega_0 = \sqrt{k/m}$. This phenomenon will take $t_{sound} \approx 1/\omega_0$ to change the resonant frequency after the gradient force is applied to the probe. It will take t_{ring} to get a steady state, but it will only take t_{sound} to change probe's mechanical and electrical response, i.e. the resonant frequency. Instead of waiting for a long time to get the steady state, monitoring amplitude or phase change in the resonance frequency of the tuning fork has a much faster response. The closed-loop system is working in the manner that it monitors the real-time change in the probe resonant frequency and uses it for further AFM scanning feedback. Some configurations use force feedback to do the Q-control. By feeding back the output signal with certain phase shift and amplitude gain, it can manually change the effective Q and thus selectively increase the speed or sensitivity. Meanwhile, the phase and amplitude excursions, or error value which is the difference between the reference signal and real-time signal, can be fed to the z-height controller to control the z-piezo motion. As shown in the figure, the phase or amplitude signals go through Proportional-Integral-Derivative

gain (PID) control circuits and fed into the z-height controller. By setting appropriate PID gain, the tip-sample distance can be maintained as a constant and the sample geometry can be described.

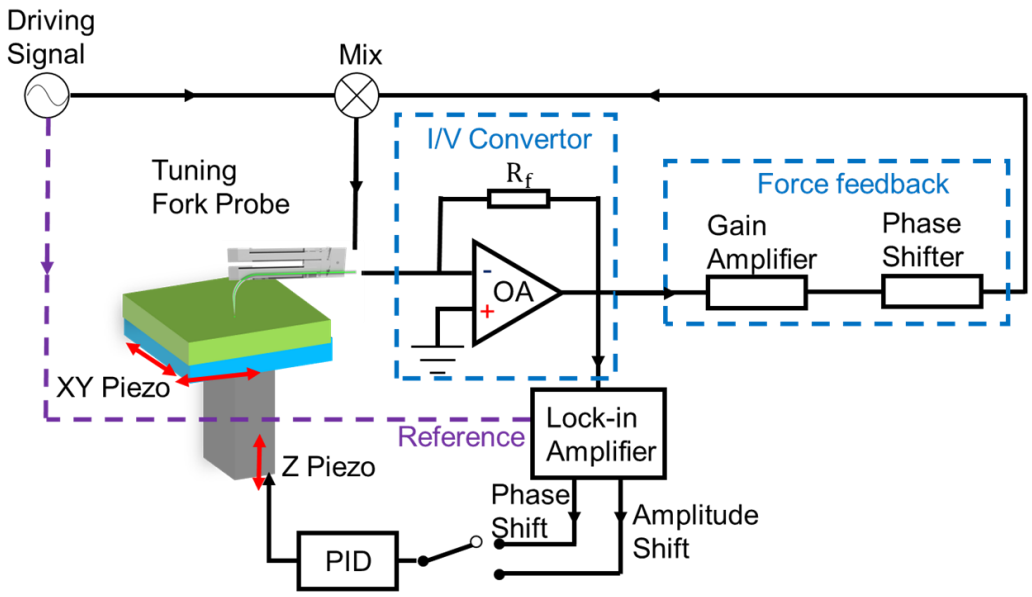

Figure 4. 3 Nanonics Piezo stage AM feedback circuit.

The Proportional-Integral-Derivative gain (PID) is a widely used feedback mechanism. It continuously calculates the error value (the difference between the setpoint and the real value) and applied Proportional/ Integral/ Derivative to it. This value will decide the movement of the piezo stage and in turn, affect the error value. The purpose of the PID circuit is using appropriate influence from P/I/D gain parameters to minimize the error excursions and accurately describe the surface geometry. P-gain is proportional to the error value and a large P-gain will result in a large z-height movement. P-gain is not enough to recover the surface geometry since it has a long response time. I-gain integrates the error over time and eliminates the residual error. D-gain takes the derivative of the error and can increase the response speed of the system. Together they can be chosen to achieve adequate response for the z-height motion.

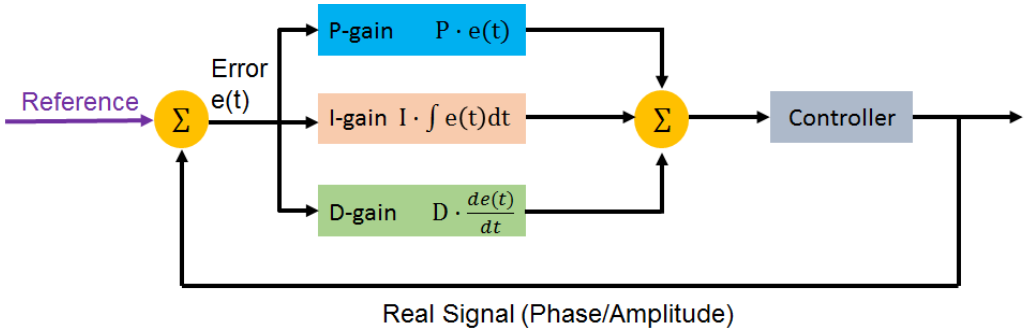

Figure 4. 4 PID feedback control circuit.

4.2 The AgNW based Tuning Fork AFM Probe Preparation and Performance

In this project, we use the two-point gluing method, where the fiber is attached to one of the prongs with two connecting points. The fiber is attached in the way that the straight region is slightly tilted from being parallel to the prongs and the bending region protrudes from the tuning fork. By carefully adjusting the tilted angle and out of plane angle, the protruding region will be perpendicular to the substrate during scanning. For the first attaching point, the non-bending region of the fiber is attached to the very forepart of the tuning fork (no metal region close to the edge) with a small amount of glue. According to the multi-mass-spring model, the increase of the mass difference will induce a reduction of Q factor. Therefore, less glue at the first point can maintain a higher Q factor. For the second attaching point, the fiber is attached to the rear end of the tuning fork. To avoid increasing effective mass, the attaching point should locate out from the soldering region.

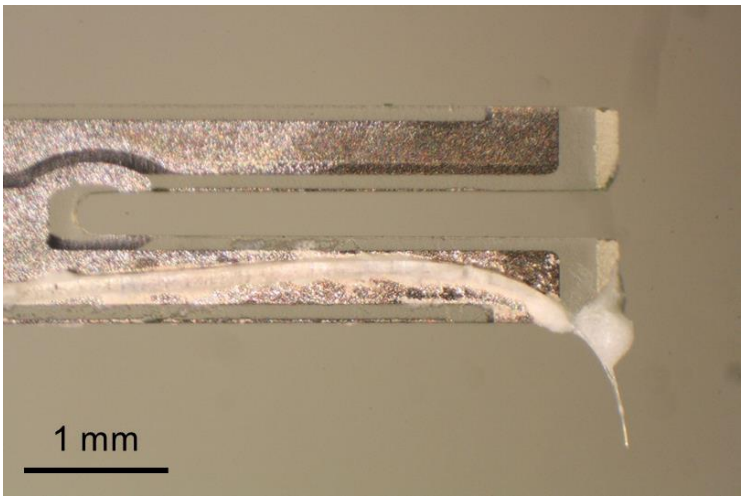

Figure 4. 5 Bent optical fiber glued onto tuning fork.

The glue we use is UV cure glue. By curing the glue under UV light for 10-20 minutes, it is possible to fully cure the glue and solidify the attaching point. The Q factor of the new probe will be checked to evaluate the quality of the probe. Due to the mass difference, the Q factor will have a reduction. A perfect probe has the Q factor around 9000~11000, while Q factor around 4000-8000 still works. A Q factor lower than 2000 might have a resolution problem and is not recommended in our approach.

After preparing the bent tapered angle optical fiber, the fiber will be attached to the tuning fork. Then an AgNW will be attached to the fiber. Our group synthesizes AgNWs in solution. By spreading them on soft PDMS substrate, we can choose suitable length and diameter of AgNW for the probe under an optical microscope. In this experiment, AgNWs whose diameter around 180 nm and length around 40~70 μm are preferred.

As shown in the figure, the AgNW is mounted on a target probe using three-dimensional micromanipulator. Due to the Van der Waals forces, tungsten tip on micromanipulator can pick up

AgNW from PDMS and align it along optical fiber tip. The AgNW should be put on the side of the fiber, so incident light with P-polarization can excite the 0^{th} order SPP mode in AgNW. The AgNW's protruding length should be less than 5 μm, for both mechanical (less vibration during scanning) and optical (less propagation of the SPP modes along AgNW) concerns.

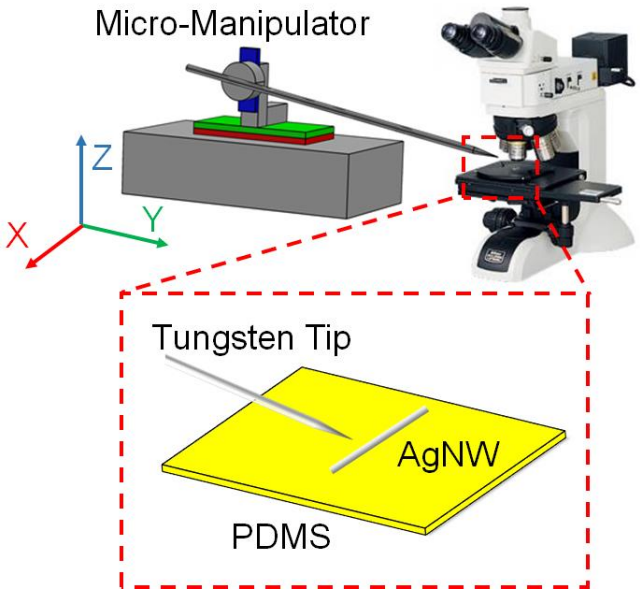

Figure 4. 6 Using micro-manipulator to pick up AgNW and align it onto the fiber.

After mounting the AgNW on fiber, the coupling efficiency needs to be checked. The Coupling Efficiency (CE) is defined as the ratio between the laser power coupled into AgNW tip and the total laser power. $CE = P_{tip}/P_{total}$. When the light comes to the tapered region of the fiber, its propagating modes are no longer supported. It has a chance to couple into AgNW as the SPP modes, scatter into free space or even reflect back. The CE is a good way to tell which channel the light prefers to go and gives a good estimation about the signal to noise ratio.

The top view of the tip should be observed under 100X optical microscope. The optical microscope should focus at the tip of the AgNW tip. The laser is then guided into the fiber and the

laser pattern of the AgNW will be recorded. Laser from AgNW will focus at its tip, while free space scattering laser will form several asymmetry rings around the center. Using CCD, the light intensity can be calculated. With our current technique, a CE around 40%-60% can be achieved.

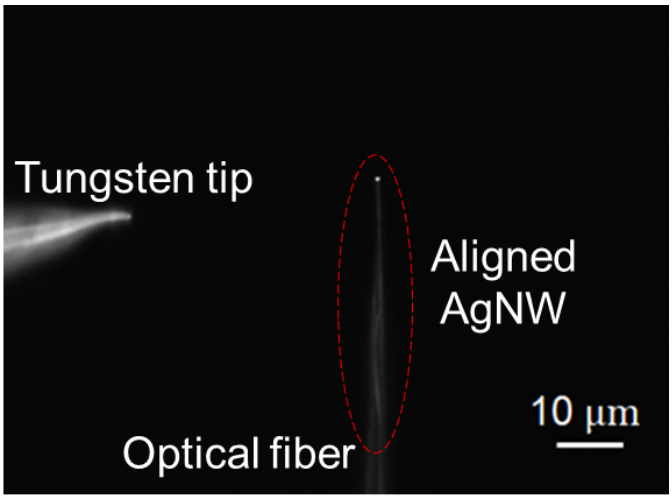

Figure 4. 7 The figure shows the aligned tapered angle fiber and AgNW probe.

After mounting the AgNW on the optical fiber, the coupling efficiency will be examined from the top view.

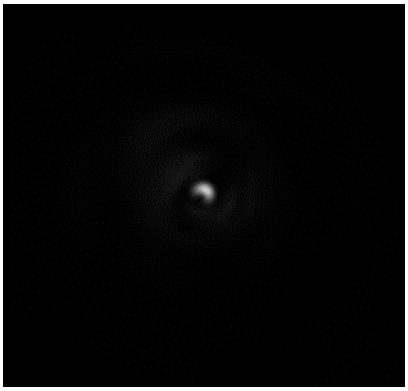

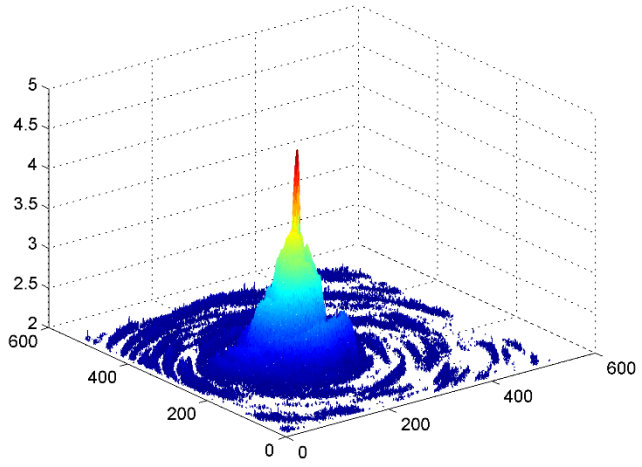

Figure 4. 8 Coupling efficiency calculation by top view of the probe.

4.3 AFM Performance

After checking the coupling efficiency, the AFM performance will be checked. Figure 4.9 shows our probe AFM performance by doing long time scanning. The sample is a graphene wrinkle with only a few nanometer heights. The AFM scanning was performed in the same region for 16th times. Each time takes around one hour. After 16 hours, the probe maintains good AFM stability, with little distorted of the AFM image.

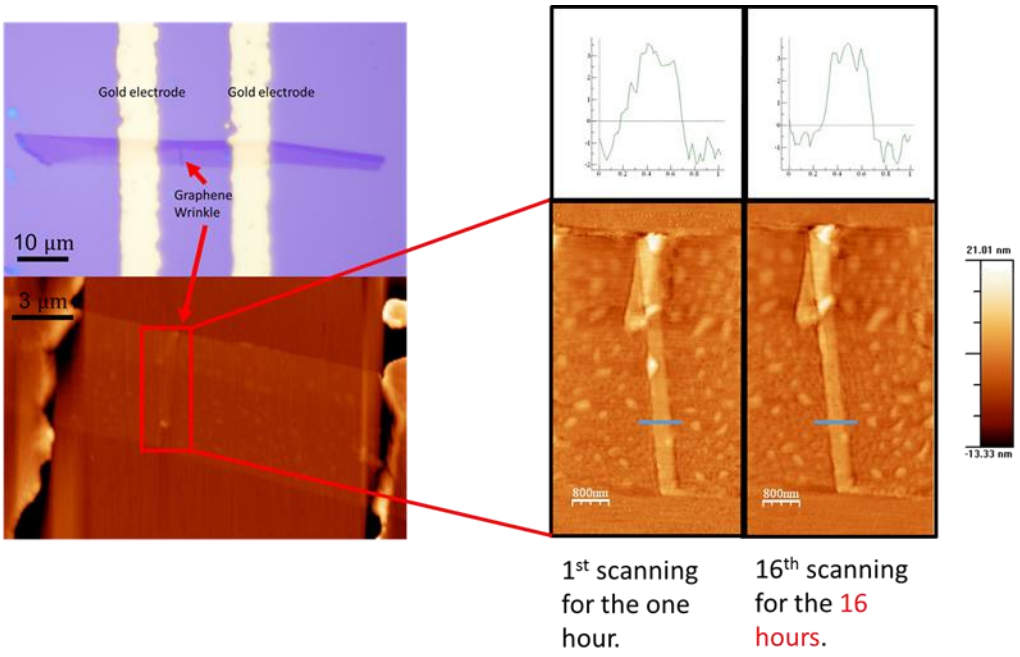

Figure 4. 9 AFM stability after scanning for 16 hours.

Chapter 5 Photocurrent Mapping

5.1 Technical Motivation for Developing AgNW-based NSOM Probe

A basic design of the NSOM probe should fulfill both mechanical and optical requirements. Both the aperture and apertureless designs have good AFM performance. By coating with the metal, their probes can obtain sub-wavelength light confinement.

In a nutshell, our design is based on the tapping mode AFM configuration. A two steps fabrication procedure is required:

1. Attaching bent optical fiber onto tuning fork. The bending shape and the mass of glue require careful design to achieving the best AFM performance. The trade-off the probe's quality factor Q and the scanning results will be optimized.

2. Mounting the AgNWs onto the tapered angle optical fiber. The coupling efficiency (CE) and the AgNW SPP mode will be examined and adjusted to achieve the highest photoresponse during the photon-sample interaction.

Instead of coating metal on the AFM probe, we use micro-manipulator to mount the AgNWs onto the probe. Comparing with bulk silver, crystalline AgNWs have improved mechanical properties with 160 GPa Young's modulus. Therefore, mounting the AgNW onto optical fiber tip can achieve good tapping mode AFM performance. On the other hand, by mounting the AgNW onto the taper region of the fiber, light can propagate from the fiber into the AgNW to excite the AgNW SPP modes. The SPP will be confined and enhanced at the tip of the AgNW, which can be used for NSOM scanning.

During the AgNW-based NSOM scanning, both reflected/transmitted light signals and photon-converted electric signals have been achieved in our group. This project is focusing on

mapping samples with the photon-converted electric signal: the AgNW-based NSOM Probe for Photocurrent Mapping.

As mentioned in the earlier chapter, the extreme confinement of the light at the AgNW tip provides a nanoscale light source with almost no background noise. The light interacting with the sample provides abundant physics and chemical phenomenon in nanoscale. At the time of this publication, there are few groups utilizing the AgNW-based NSOM probe, but no Photocurrent Imaging Technique has been developed. On the other hand, the photocurrent has a close bond to the sample bandstructure and near-field plasmon-matter interaction. Observing subwavelength scale bandstructure information can help researchers to have a deeper understanding of the sample in the micro world. Therefore using our AgNW-based NSOM probe to study photocurrent mapping and the plasmon-matter interaction in nanoscale becomes the primary motivation of this project.

5.2 2D Sample Preparation

Two-dimensional (2D) materials have fancy photocurrent response which can not be seen in bulk structure. 2d materials can also be used in the confined system, for example, the near-field imaging system whose probe is few nanometers from the substrate. Therefore, using 2D materials to build a photocurrent mapping device can provide many interesting results.

Two-dimensional materials are crystalline materials consisting of single or few-layer atoms. In these layered structure materials, the atoms are arranged in a plane with the strong in-plane bond. While the layers are held together by the out of plane Van der Waals forces.

Since the first isolation of graphene in 2004 from graphite, the two-dimensional material family has grown rapidly and newly emerged materials have brought more amazing properties into our view. The reduction in the third dimension of bulk material to atomic level induce quantum confinement in that dimension, which has a strong impact on the band structure of the materials

and are in stark contrast with their three-dimensional counterparts. Since then, a large amount of research has been directed at their abundant physics and chemical properties. Until today to the best of our knowledge, Two-dimensional materials offer great flexible to tune their electrical and optical properties, efficient light absorption can be achieved even in single atom thickness structure providing high responsivity in photo detecting, being mechanically strong and flexible to withstand large strain during transferring and manufacturing.

Two-dimensional materials have a variety of physics and chemical properties. Graphene, as the first 2D materials with zero-bandgap semimetal, has high carrier mobility. TMDCs, on the other hand, can change their bandstructure by changing the layer number, which can be used for light collection and photon-charge conversion. Due to the Van der Waals forces and their strong mechanical properties, these atomic-thickness layers can be attached to the substrate, attach to their transferring intermedia, withstand large forces including stretching, bending, folding and rolling, and stacked layer by layer or transfer onto the certain substrate while still preserving their high crystalline order. Thus, these Van der Walls forces based atomic thickness layered structures offer a way to studies their amazing properties on different substrates and environments. Combining them to utilize their different properties for complicated functions is one of the most interesting topics in this field.

Graphene is a single layer of carbon atoms arranged in the hexagonal lattice. It is one of the basic building element of other carbon-based materials. The graphene was first mechanically exfoliated using Scotch tape in 2004 by Andre Geim and Konstantin Novoselov at the University of Manchester.

As a sheet of two-dimensional sp^2-hybridized carbon, its extended honeycomb lattice is the basic building block of other allotropes. Stacked in laa yered structure, it can form graphite in

three-dimensional. On the other hand, the one-dimensional carbon nanotube can be treated as rolled graphene, and zero-dimensional fullerenes can be treated as wrapped graphene, as shown in figure 5.1.

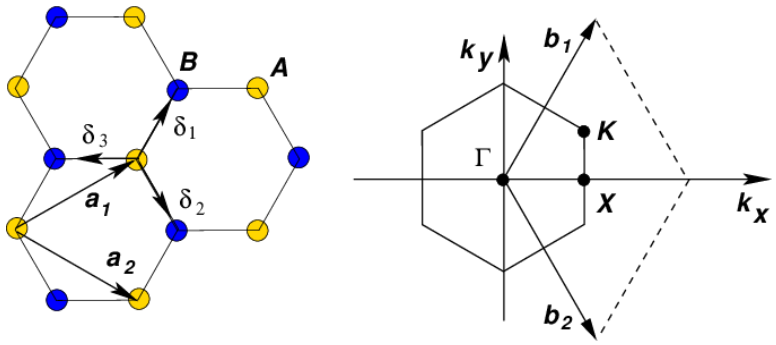

Figure 5. 1 Graphene lattice and its Brillouin zone.

The lattice structure of graphene can be seen as a triangular lattice with two basic atoms A and B in the unit cell as shown in figure 5.1. The lattice constant between A and B is $a \approx 1.42$ Å. Three A atoms and three b atoms form regular hexagon shape. By the tight-binding approach, the electronic dispersion can be achieved. As shown in the figure 5.2, around the K and K' at the corner of the graphene Brillouin zone, cone-shape linear bandstructure can be obtained. These points are Dirac points, and bring important physics phenomenons to graphene. For example, due to the linear shape near Dirac point, the effective mass for carriers there are almost zero which gives high carries mobilities. Conduction and valence band meet at the Dirac point without an external field. So under certain gate bias, the fermi level of graphene can be tuned easily and introduce a significant change of charge carries densities as shown in figure 5.3.

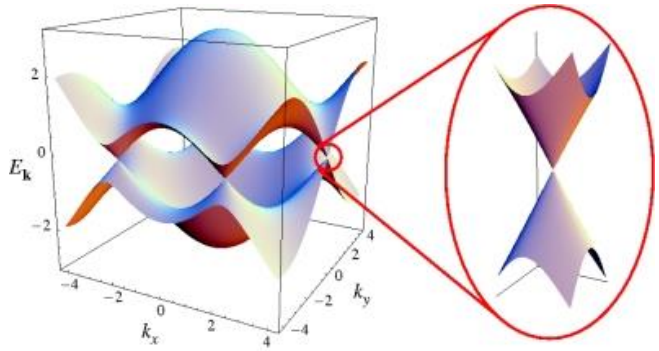

Figure 5. 2 Graphene electronic dispersion and Dirac cone.[99]

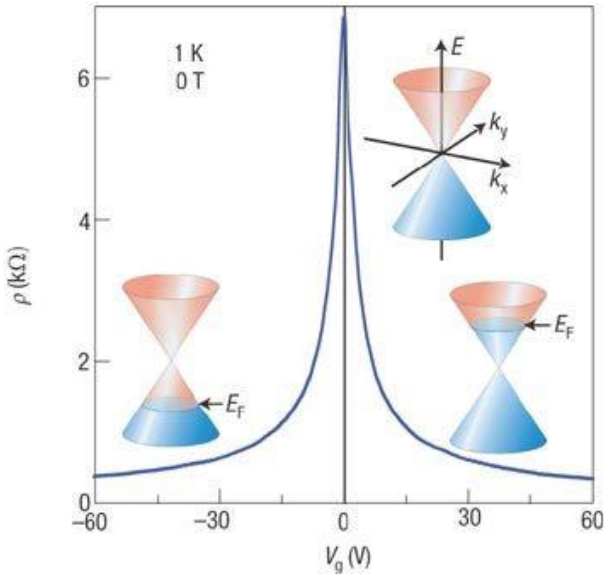

Figure 5. 3 Graphene Fermi level tuned by the gate with ambipolar electric field effect.[100]

Since the first synthesized graphene appeared, different Graphene synthesizing methods have been developed, including chemical vapor deposition (CVD), mechanical exfoliation, epitaxial growth on SiC, chemical reduction of graphite oxide, liquid phase exfoliation, carbon nanotube unzipping and so on.

CVD graphene provides an efficient way to create large scale monolayer graphene. However, it is soon realized that CVD graphene has many drawbacks, such as defects and grain boundaries. The carrier mobility can decrease dramatically due to the scattering from these discontinuous features. And thus the graphene quality is degraded. On the other hand, mechanically exfoliation method can obtain pristine graphene with no defects and continuous structure. This continuous crystallite graphene has good quality in terms of electrical and optical properties and has always been selected as the research object to study novel physics and chemical properties. Thus in this project, the graphene is synthesized using mechanical exfoliation method.

The famous scotch tape is used for graphene cleavage. The reason we choose scotch tape is the tape stickiness since most of the groups in the world find it a good intermediary to split graphene layer against the interlayer Van der Waals forces. The whole transfer process is shown in figure 5.4 a-g. Putting onto the scotch tape, the graphite flake will be spread all over the tape by repeatedly folding the tape. During the folding, it has a chance to split the graphite into single or few-layer graphene flakes. The graphite covered tape will then be put onto clean smooth silicon oxide wafer, with flake side facedown and attach to the substrate. Eraser will be used to rub the tape-wafer and certain stress will be conducted onto their interface. This process will increase the probability of leaving graphene flakes attached to the silicon oxide wafer. The tape-wafer will be heated up to 90℃ for 2 minutes to further increase the probability. The tape will be removed later. Due to the light interference, 300nm silicon oxide on top of silicon will help to see the graphene flakes under the microscope.

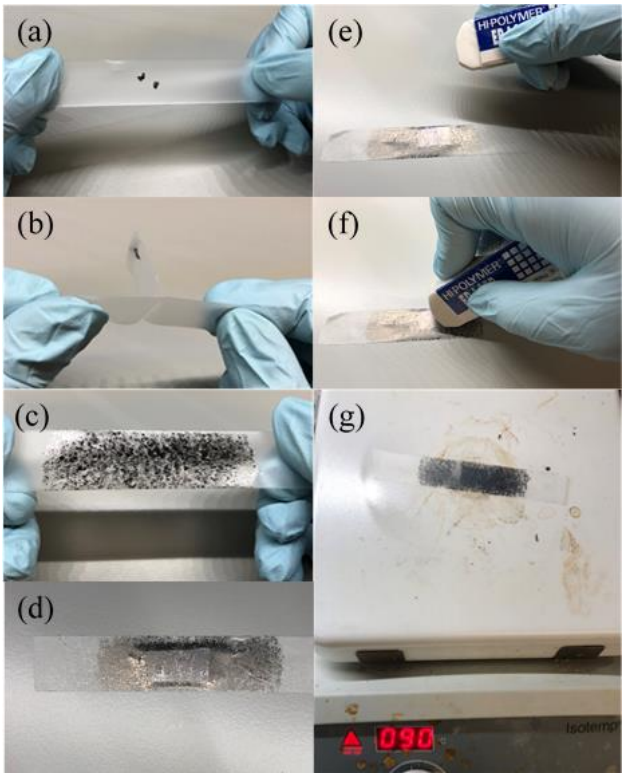

Figure 5. 4 Mechanical exfoliation method for Graphene and MoS2. (a) Graphite flake on scotch tape. (b) Repeatedly folding the tape. (c) Graphite flakes covering the tape. (d) Attaching the tape onto silicon oxide substrate. (e)-(f) Using the eraser to rub the tape. (g) Heat up to 90 ℃ for 2 minutes.

The main drawbacks of this method are the uncontrollability of layer number, sample size, and flake shape, making it impossible to commercialize. But in our group, a regular size of $20\ \mu m \times 20\ \mu m$ or even larger can be easily achieved with mono-layer or few-layer graphene. As shown in the figure 5.5. The graphene flakes are prepared in our group on silicon oxide substrates. Using our methods, size around $100\ \mu m \times 20\ \mu m$ of graphene can be obtained.

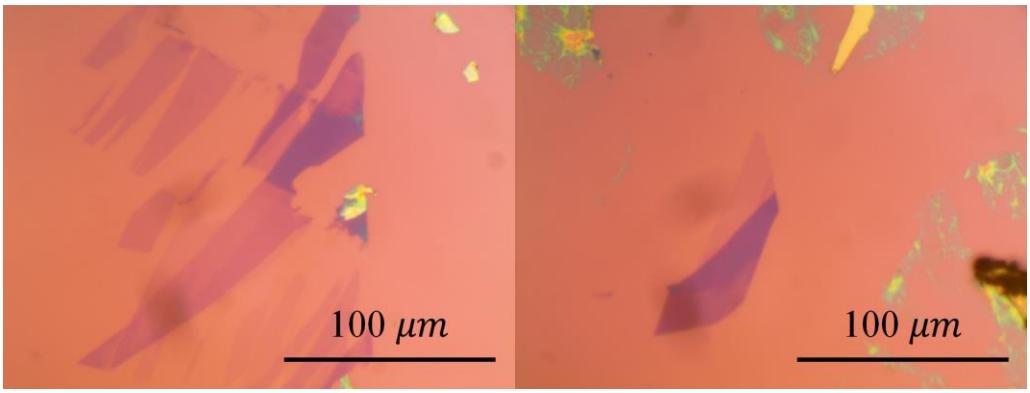

Figure 5. 5 Large size graphene flakes.

Graphene sample can be transferred using a stamp method developed in our group previous studies. By using our group's method, graphene can be transferred from Silicon oxide onto most wanted substrated, which is an extremely useful tool to build up any structure for further research. So once a good sample is found on the wafer, it will be picked up and transferred onto a certain substrate to make a new device.

One of the most impressive advantages of graphene is the ability to absorb around 2.3% of the incident over a broad wavelength in its single layer structure. However, the highest photoresponsivity of graphene is still lower than 10mA/W. Low photoresponsivity is mainly attributed to the low optical absorption and short lifetime of the electron-hole pairs before they recombine, therefore the internal quantum efficiency is around 6-16%, lower than other materials.

The wrinkle is a ubiquitous structure in most of the two-dimensional materials. It can be formed by different thermal expansion during their growing procedure or can be induced by their stamp during transferring. The bandstructure, electrical and optical properties are still not well understood. However, this submicron size folded structure can have quantum confinement smaller to graphene carbon-nanotube and graphene nanoribbon, which will change its bandstructure and

induce the optical gap. At the boundary between wrinkle and graphene sheet, there is also built-in voltage. So graphene sheet with wrinkles on it is a good analogy of semiconductor FET with light absorption and photocurrent generation, where the wrinkles are the channel materials and the graphene sheets are the electrodes. Due to the good matching between them, photogenerated carries can be efficiently separated and extracted from the device, resulting in enhanced photosensitivity.

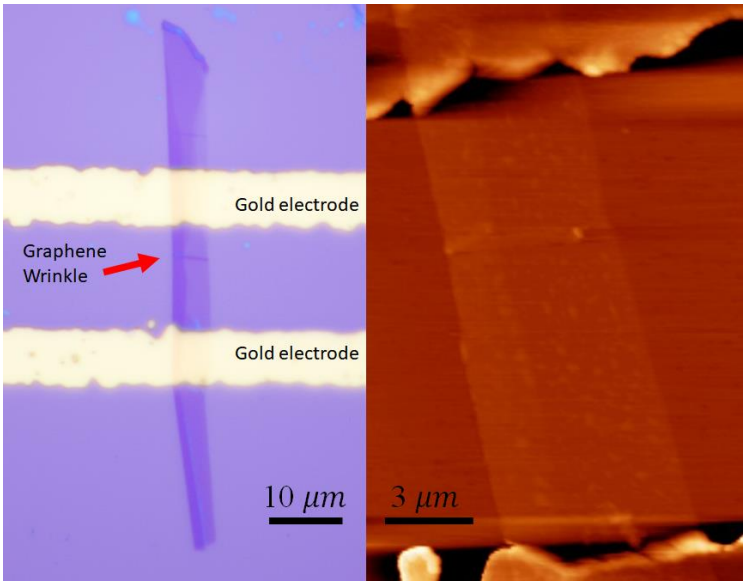

Figure 5. 6 Graphene wrinkle and its AFM image.

In our lab, we can induce graphene wrinkle during transferring. After picking up the sample with a stamp, extend their length by 10% by stretching the stamp and then releasing it is enough to create multiple wrinkle structures without pull the graphene sample apart. These wrinkle sample will then transfer to a certain substrate to make devices. Figure 5.6 shows using stretching and releasing stamp method to create wrinkles.

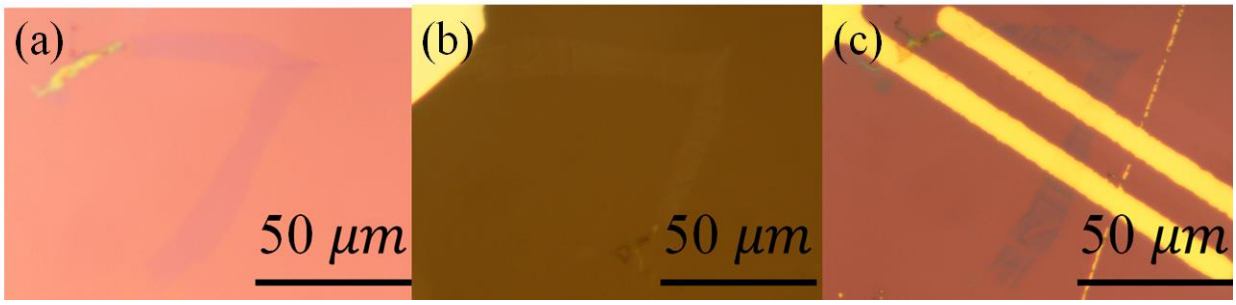

Figure 5. 7 Graphene wrinkles. (a) Before transferring, graphene sample on a silicon substrate. (b) During transferring, graphene sample is released together with a stamp and create wrinkles. (c) After transferring, graphene wrinkles are put onto gold electrodes.

Single layer graphene has opened up ways to study and utilize two-dimensional materials and bring vast micro-world novel physics and chemical properties. But due to its zero-bandgap structure, pure graphene cannot be efficiently turn off with gate and as a consequence cannot be used as a semiconductor FET device. Bandgap engineering has been developed to induce bandgap into graphene, but these methods are always inefficient. One way to make a graphene semiconducting device is graphene Wrinkle which has been introduced. A more general way is to use other two-dimensional materials, for example, Transition Metal Dichalcogenide monolayer materials (TMDCs).

TMDCs are atomically thin two-dimensional compounds with the types of X-M-X. One layer of the transition metal M (Mo, W, etc.) is sandwiched between two layers of chalcogen X (S, Se, etc.). Due to the interlayer Van der Waals forces, TMDCs single layer sample can be isolated using mechanically exfoliation method, similar to their graphene predecessor. In TMDCs family, MoS2, WS2, MoSe2, WSe2 and etc have electrical and optical properties distinctly different from graphene, which makes them potential candidates to build low dimensional devices. In particular, in this project, we focus on MoS2 and its application for photocurrent detection.

Molybdenum disulfide (MoS2) is composed of molybdenum and sulfur. MoS2 bulk has a similar structure to graphite. It is stacked by layered of single atom thick of S-Mo-S 2D single crystal. Each layer has the thickness of 6.5Å and layers are held together by the Van der Waals forces. This is similar to graphene and therefore single and few-layer MoS2 flakes can be obtained using mechanical exfoliation method. MoS2 lattice consists of one layer of hexagonally arranged Mo atoms sandwiched by two layers of hexagonally arranged S atoms. The crystal lattice constant is 3.2Å, the two sulfur atoms layer distance is around 3.1Å. Monolayer MoS2 has a direct bandgap around 1.9eV. There is a transition from direct bandgap to indirect bandgap when the layer number increases. For bilayer mos2 it has 1.5eV indirect bandgap and for bulk mos2 it has 1.2eV indirect bandgap. With its direct bandgap, mobility above 100cm^2/(V*s) and its remarkable mechanical properties, monolayer MoS2 is a powerful material for the optoelectronic application.

Graphene's first isolation method via mechanical exfoliation from graphite bulk inspire the researchers and paves way for the fabrication of other 2D materials. Due to weak out-of-plane Van der Waals forces, MoS2 can be reduced down to single layer flakes using scotch tape. This method can prepare single crystal pristine MoS2 with fewer boundaries and defects. The quality is better than other preparation methods in terms of carriers scattering and trapping, which is preferred for fundamental research in the lab. Nevertheless, the uncontrollability of sample layer number and the shape make it not suitable for large-scale practical applications.

In this project, we use scotch tape to mechanically exfoliate MoS2, similar to graphene exfoliation.

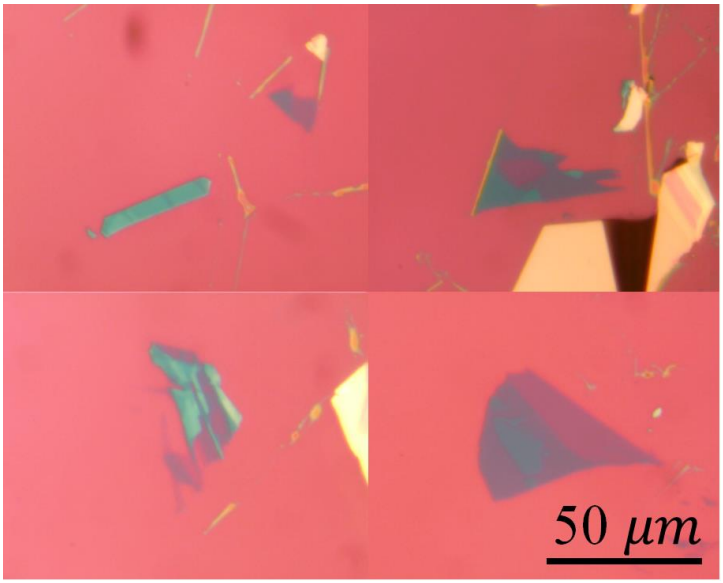

Figure 5. 8 MoS2 flakes

MoS2 sample can also be transferred using the stamp method, similar to graphene transferring. After finding the sample we want, we can use our setup to pick up the sample and transfer it to the target substrate.

MoS2 has high photoresponsivity. The first MoS2 optoelectronic devices were reported by Yin. The MoS2 phototransistor has 1mA/W photoresponsivity at 670nm. Later, the different MoS2 structure has been fabricated and pushed the photoresponsivity up to 880A/W at 680nm for exfoliated monolayer MoS2 and 2200/780 A/W (vacuum/air) for CVD MoS2. Such huge responsivity makes us decided to use MoS2 as the major photodetection materials in our devices.

The powerful transferring method developed in our group has helped us to transfer two-dimensional materials onto target substrates, but furthermore, it opens the door to the realization of artificial heterostructures of 2D materials stacked layer by layer. These heterostructures can be built

on conventional bulk materials, electrodes, or on other 2D materials using stamp transferring method. Combining them will bring novel physics and chemical properties.

5.3 Photocurrent Introduction

The photocurrent is an electric current generated from the optoelectronic materials. Photocurrent may occur as a result of the photovoltaic effect or photo-thermoelectric effect, where the optoelectronic materials absorb the photons and generate electron-hole pairs or a voltage difference. The electron-hole pairs or the voltage difference will generate photocurrent. The conversion of the photons to the electric current signal enables different applications including photon detection, imaging mapping, optical spectroscopy, and fiber-optic communication.

There are several different photocurrent generation mechanisms. 1. Photocurrent generated by electron-hole pairs separation, including Photoconductive Effect (PCE) and Photovoltaic Effect (PVE). 2. Photocurrent generated by thermal effect, including Photo-thermoelectric Effect (PTE) and Photo-bolometric Effect (PBE). Details about these mechanisms will be discussed in the following chapters.

There are several important figure of merit which can be used as the reference to describe the photocurrent quantitatively, their units and formulas are shown in the table. The Responsivity (R) is the ratio between photocurrent and the incident light power. It is an indication of the power to convert the phonon into an electrical signal. For a constant incident light power, a higher responsivity device has a larger output photocurrent. Here R is responsivity, I_{photo} is the photocurrent and P is the incident light power. The External Quantum Efficiency (EQE) is the ratio

between the number of photocurrent charge and the number of the total incident photons. The EQE can be larger than 1 with certain optical gain, which means one photon can excite more than one pair of electron-hole carriers. Here h is the Planck constant, c is the speed of light, e is an elementary charge, λ is incident light wavelength. The Internal Quantum Efficient (IQE) is the ratio between the number of photocurrent charge and the number of the absorbed photons. The photons absorbed efficiency η can be used to describe the photon loss due to the transmission reflection, $IQE = \eta \cdot EQE$. The response time of the device describes the time it takes to generate photocurrent after light absorption. It is measured on either a rising edge or falling edge between 10% and 90%. The bandwidth of the photocurrent describes the frequency range of the light which can excite photocurrent. Noise Equivalent Power (NEP) is the power to generate a photocurrent which has an equivalent magnitude of the noise at 1Hz bandwidth. It describes the noise power in the devices. Here PSD is the current noise power spectral density at 1 Hz bandwidth.

	Unit	Formula
Responsivity	A/W	$R = \frac{I_{photo}}{P}$
External quantum efficiency (EQE)	%	$EQE = R \cdot \frac{hc}{e\lambda}$
Internal quantum efficiency (IQE)	%	$IQE = \eta R \cdot \frac{hc}{e\lambda} = \eta \cdot EQE$
Response time	s	
Bandwidth	Hz	
Noise equivalent power (NEP)	$W/Hz^{-\frac{1}{2}}$	$NEP = \frac{PSD}{R}$

Table 2 figure of merit

As mentioned above, both reflected/transmitted light signals and photon-converted electric signals have been achieved in our group. In this project, we chose the photocurrent to map the material photoresponse. The reason we chose the photocurrent is that of the close connection between photocurrent and sample bandstructure.

By applying voltage for both channel bias and gate bias, the current can describe the bandstructure in a macro way. For example, linear IV curve means an ohmic contact while exponential IV curve means a Schottky barrier. However, this method could not provide details about the bandstructure in spatial distribution.

The tilted conduction and valence band induce a built-in voltage, therefore an internal Coulomb force will apply on the charge carriers. The slope of the tilted band can be reflected by the photocurrent magnitude, where larger slope has larger built-in voltage and generates larger current. Thus the nanoscale photocurrent can be affected by the band shape and provide a way to describe the sample's bandstructure. With the AgNW-based NSOM tip, our setup can impinge photons to excite photocurrent in nanoscale and map the bandstructure with extremely high spatial resolution. Details about the bandstructure mapping will be discussed in the following chapters.

5.4 Spatial Resolution of the Photocurrent Mapping

The AgNW-based NSOM probe configuration will be introduced in this chapter. In this project, we use the Nanonics MultiView 2000 single probe optically integrated AFM-Raman-NSOM device. This device provides both shear force mode and tapping mode AFM for tuning fork and has good feedback stability.

As mentioned in the previous chapters, we developed our own method to prepare the NSOM probe. After attaching the bent tapered angle fiber onto the tuning fork, the tuning curve will be checked. The optical properties, including the light coupling efficiency and the tip light

pattern, will be checked after the AgNW is put onto the fiber tip. In this experiment, we use 532 nm green laser or 630 nm red laser as the light source. If the probe quality is good, the AFM performance will be checked. On the other hand, we have mentioned the two-dimensional sample preparation. After transferring the 2D materials onto the target substrates, we build three-terminals or two-terminals devices. Then the sample's IV curve will be acquired to check the electric properties, including sample conductivity, junction connection, and electric leakage. The optical response might be checked to make sure the sample is suitable for photocurrent mapping, by focusing a free space laser onto the sample.

When both the sample and probe are ready, they will be mounted onto the device. As shown in the figure, during scanning the bias circuit applies voltages on both channel and gate to drive the photocurrent. The bias voltage will be changed to acquire photocurrent mapping under different conditions.

As mentioned in chapter 4, the photocurrent is modulated using the oscillation from tuning fork. The reason to do the modulation is to cancel the large background noise. For the most common used scattering type NSOM, a free space laser beam will be focused on the gap between the tip and the sample. The size of the laser spot is much larger than the size of the tip. Therefore it will generate large background DC noise. To cancel these noise, researchers use the oscillation from the probe to modulate the signals. In this structure, the center laser dot is modulated by the frequency of the cantilever f. a lock-in amplifier will be used to demodulate the signal and pick out the information we want. This method can dramatically reduce the DC noise, however, it will induce large 1^{st} order noise due to the backscattering from cantilever shaft. To avoid 1^{st} order noise, researchers use complicated optical demodulation setup and algorithm to further filter out the 1^{st} order noise.

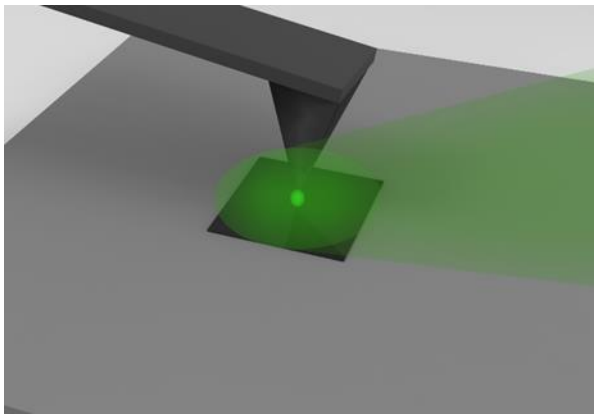

Figure 5. 9 The spot size from the laser beam is much larger than the size of the scattering NSOM probe.

Theoretically, a nanoscale light source using AgNW-based NSOM probe won't have any DC noise and 1st order noise, as long as the coupling efficiency is 100%. However, due to the imperfect coupling from the optical fiber into the AgNW, and also the circuit noise, we still need to use our tuning fork to modulate the photocurrent signals.

The photocurrent signals will flow into the noise filter circuit, and the noise will be filtered to avoid signal saturation in the preamplifier stage. The photocurrent signals will be amplified in the preamplifier to increase the signal to noise ratio. The driving frequency of the tuning fork will be used as a reference to lock the photocurrent signals. After all these stages, the AFM image and the Photocurrent Mapping image will be achieved.

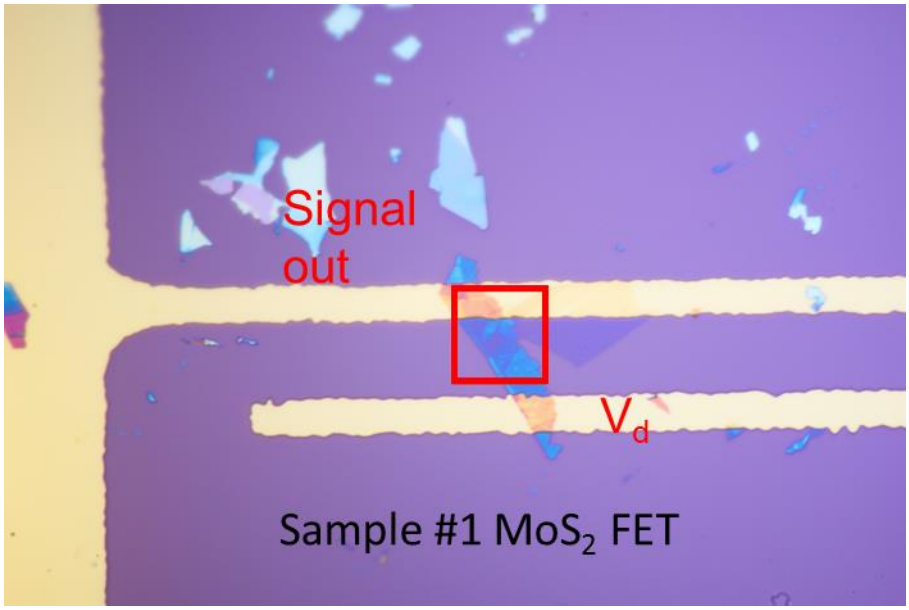

Figure 5. 10 MoS_2 FET sample.

As shown in figure 5.10, a MoS2 sample with flakes on its surface is transferred onto gold electrodes. A small bias voltage V_d=10mV is applied to the channel. Figure 5.11 shows the AFM and photocurrent mapping images of the sample. In the AFM image, there is dust on the sample surface and degrade the vertical AFM resolution. Those large particles cover the small MoS_2 features in AFM image. But here shows the power of the NSOM photocurrent mapping whose is not affected by these dust and can provide optical information with high resolution. In the photocurrent mapping image, sharp signals can be found at MoS_2 flake edges. As we zoomed in and scanned the feature regions, a photocurrent with 15 nm resolution has been achieved. These results show that our AgNW based NSOM probe has a very high spatial resolution for the photocurrent mapping. A 532 nm green laser is used during mapping with power around 1 μW.

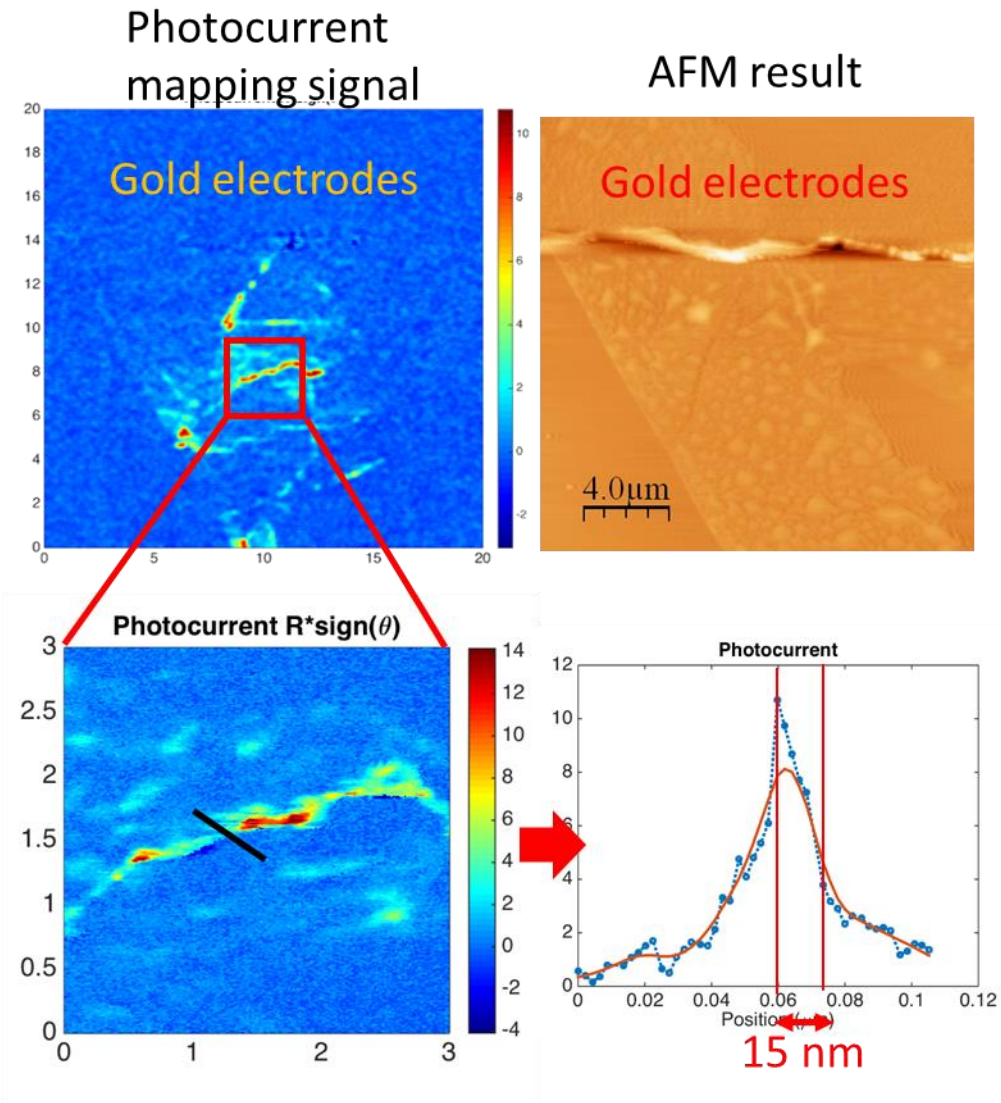

Figure 5. 11 High Spatial Resolution Photocurrent Mapping.

5.5 Graphene Wrinkle Photocurrent under Different Bias Voltage

A few-layer graphene wrinkle sample is prepared for photocurrent mapping as shown in figure 5.12. Before the mapping experiment, a transfer curve is measured using V_{bg} sweep. Due to micro-capacitor effect, the voltage sweeping curves didn't overlap. For V_{bg} from +60 V to -40 V, the Dirac point of the graphene wrinkle is close to +20V. A 532 nm green laser is used during mapping with power around 1 μW.

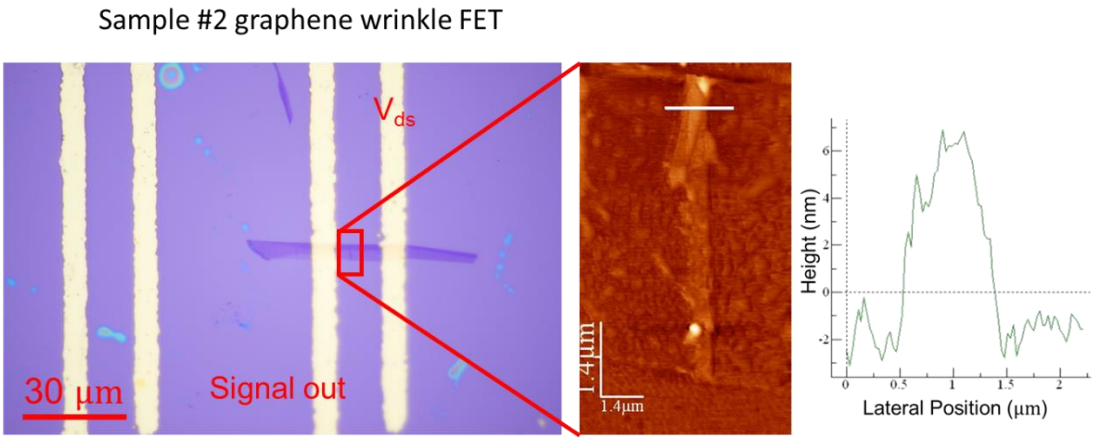

Figure 5. 12 Graphene Wrinkle sample.

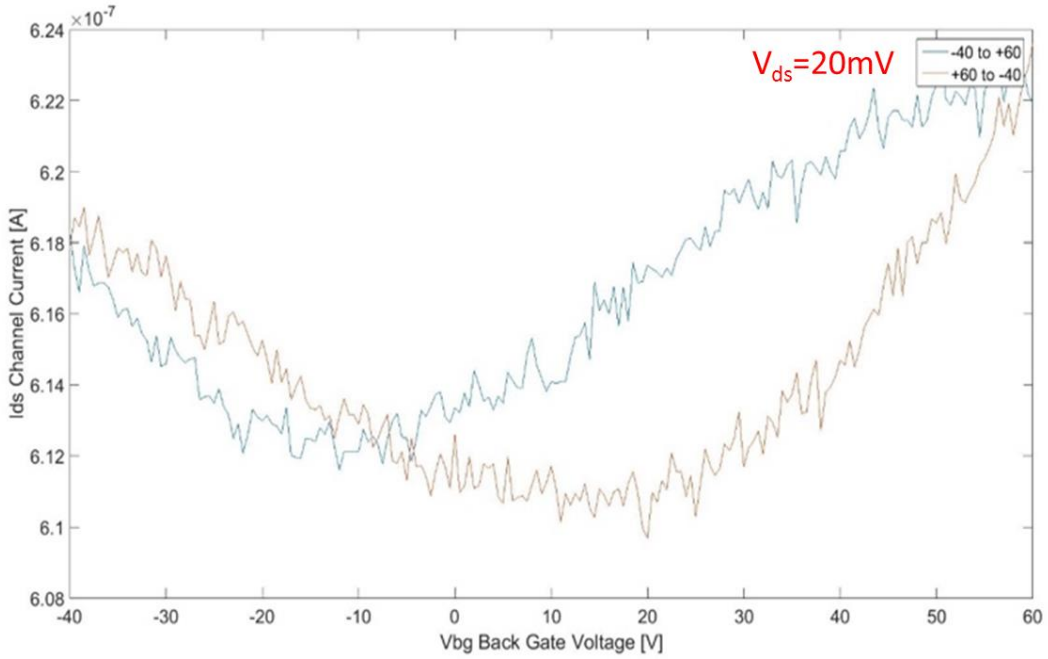

Figure 5. 13 Graphene Wrinkle transfer curve.

A photocurrent mapping with back gate voltage sweeping from +60 V to -50 V had been achieved.

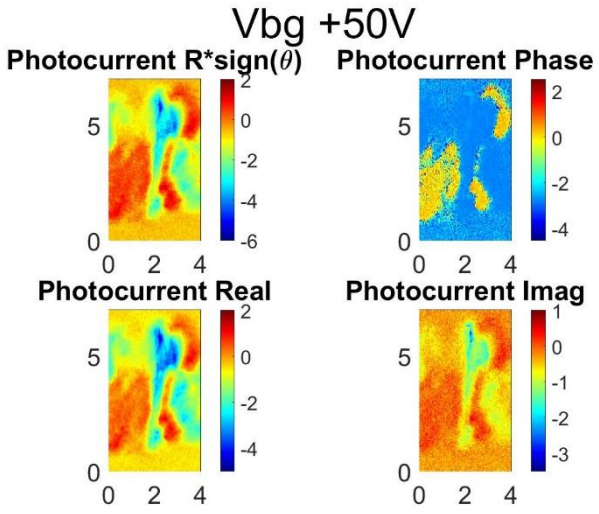

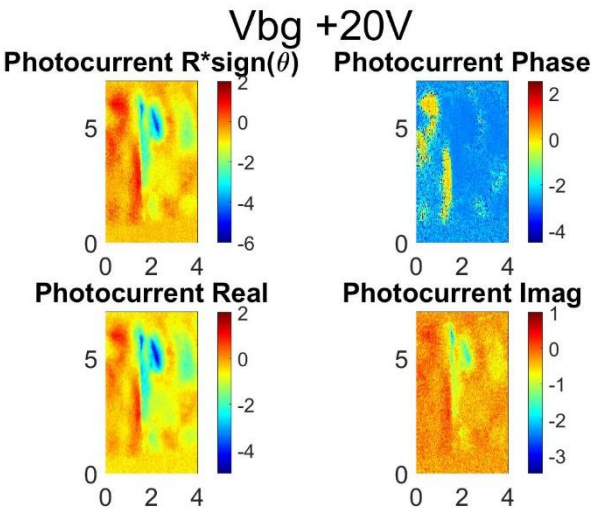
Vbg +20V
Photocurrent R*sign(θ)
Photocurrent Phase
Photocurrent Real
Photocurrent Imag

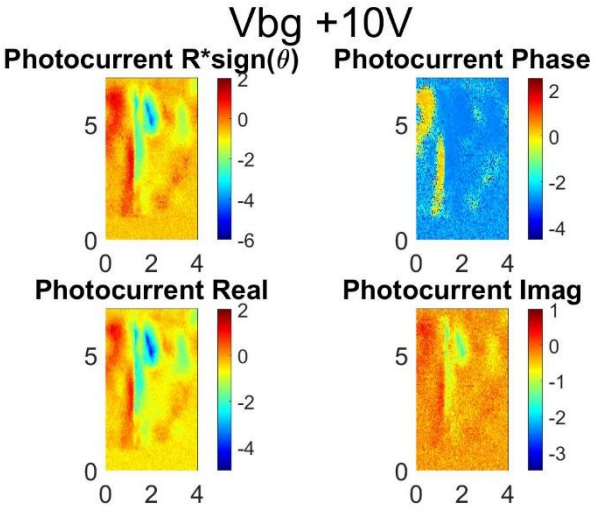
Vbg +10V
Photocurrent R*sign(θ)
Photocurrent Phase
Photocurrent Real
Photocurrent Imag

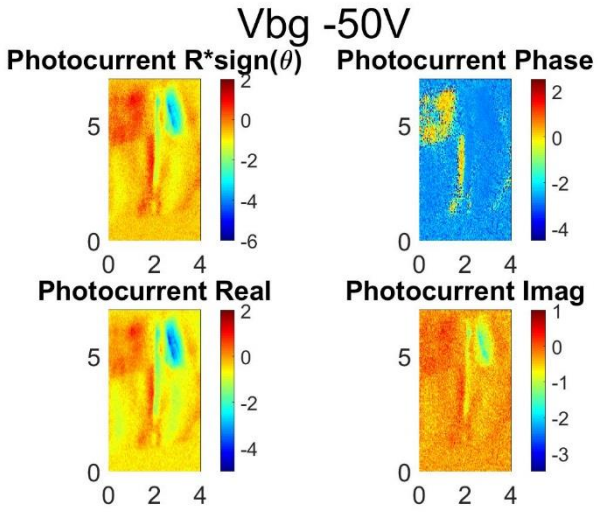

Figure 5. 14 Photocurrent mapping results of amplitude, phase, real and imaginary part under different $V_{bg.}$

From the scanning results, we can know that the photocurrent on the left part of the sample switches sign during back gate voltage sweeping. And the switching point is close to the +60 V to – 40 V Dirac point. Since the bandstructure of the graphene wrinkle and the region is still unclear, the mechanism of photocurrent sign switching needs further studies. However, for the first time, our method provides a high-resolution method to look into the details of sample bandstructure information.

5.5 Influences to the Photocurrent from the Electrode Contacts and the Interfaces

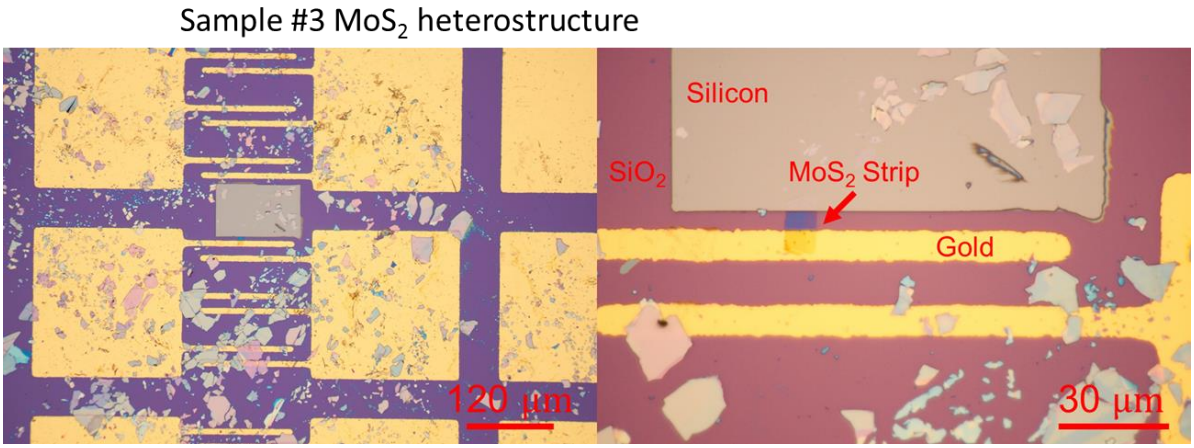

Figure 5. 15 MoS_2 heterostructure.

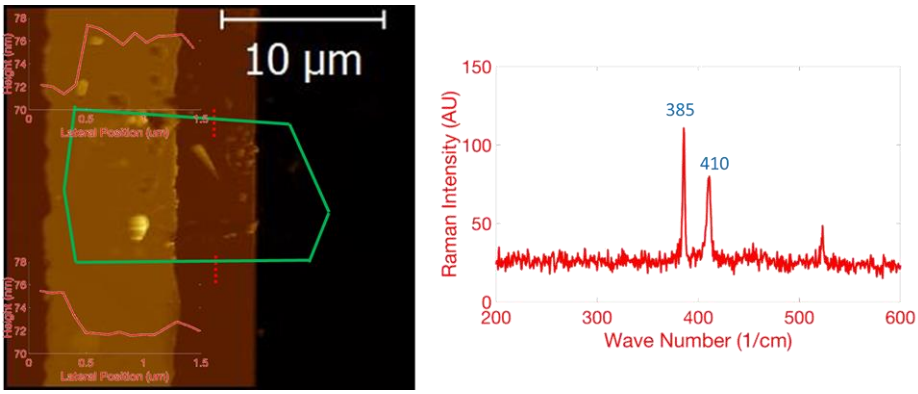

Figure 5. 16 AFM and Raman spectrum of MoS_2 heterostructure.

A heterostructure few-layer MoS2 sample is transferred between gold and silicon. The silicon region is created using SiO_2 etching method. The MoS2 sample is connecting the gold and silicon area as a bridge and form a two terminals device. Different in-channel voltage is applied to the MoS2 to obtain the photocurrent mapping images. A 532 nm green laser is used during mapping with power around 1 μW.

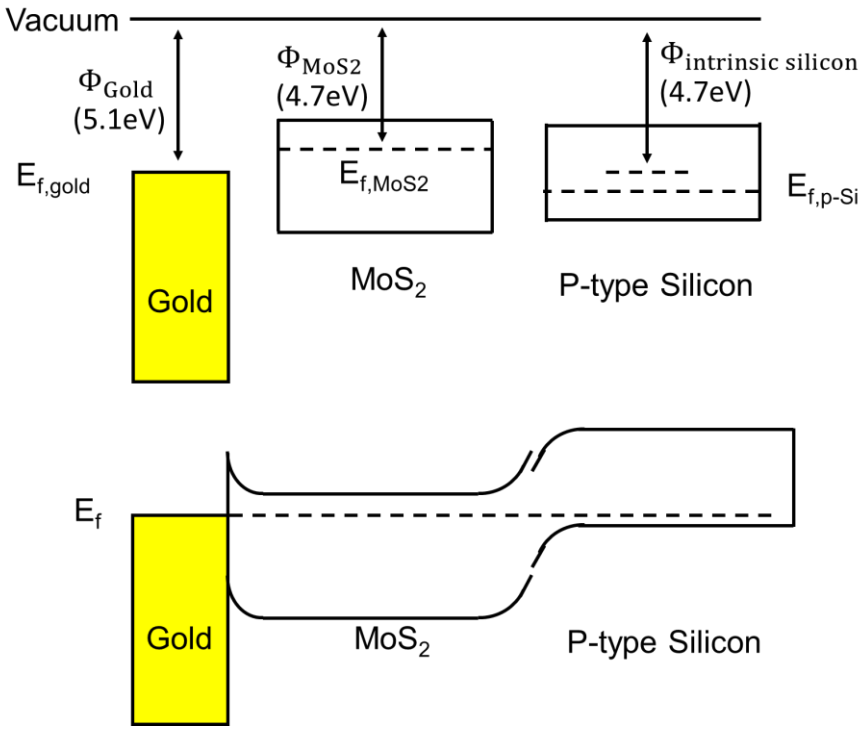

Figure 5. 17 Bandstructure of the heterostructure under our hypotheses.

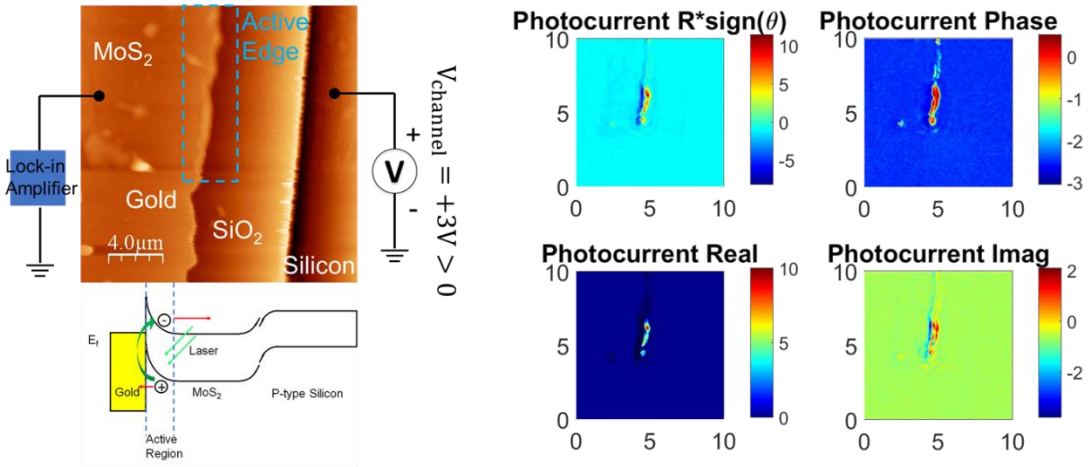

Figure 5. 18 Photocurrent mapping when $V_{channel}$=+3V>0

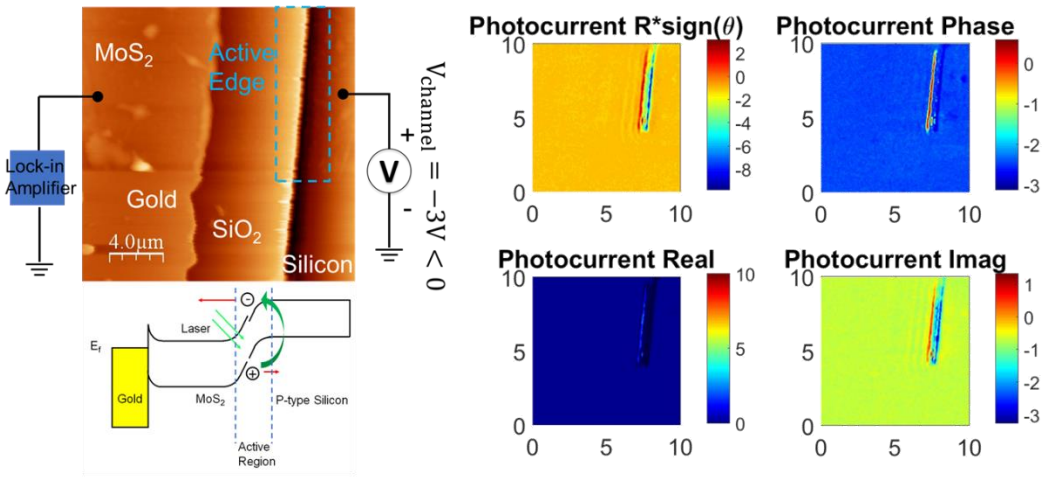

Figure 5. 19 Photocurrent mapping when $V_{channel}$=-3V<0

From figure 5.18 and 5.19 we can see that the photocurrent active region is different under different bias. When the $V_{channel}$ or $V_{gold\text{-}MoS2\text{-}p\text{-}silicon} > 0$, the active region is the edge between MoS_2 and gold electrode. When the $V_{channel}$ or $V_{gold\text{-}MoS2\text{-}p\text{-}silicon} < 0$, the active region is the edge between MoS_2 and the silicon substrate. The bandstructure is estimated in figure 5.17. There is a hypothesis for this phenomenon:

When the applied voltage $V_{gold\text{-}MoS2\text{-}p\text{-}silicon}$ is larger than zero, the PN junction between MoS_2 and gold increases its depletion length and generate a large build-in voltage. When the applied voltage is larger than the threshold voltage (+1 V in this sample), the PN junction at that edge is turned on and start to separate the electron-hole pairs excited by the incident photon.

When the applied voltage $V_{gold\text{-}MoS2\text{-}p\text{-}silicon}$ is smaller than zero, the PN junction between MoS_2 and p-type silicon increases its depletion length and generate a large build-in voltage. When the applied voltage is smaller than the threshold voltage (-1 V in this sample), the PN junction at that edge is turned on and start to separate the electron-hole pairs excited by the incident photon.

Due to the high concentration of carries in both the gold electrode and p-type silicon, a very short distance of electric field distribute at the edge without penetrating into the two terminals. Such short distance can only be studied using high spatial resolution NSOM probe which is the perfect example to show how powerful our AgNW based NSOM probe is.

Chapter 6 Vertical plasmon-matter interaction reconstruction

6.1 Z-plot method

As we mentioned before, the apertureless NSOM tip can provide imaging resolution less than 20 nm. The apertureless NSOM uses a metal coated sharp tip to scan the sample. The external light source is illuminated into the gap between the tip and the sample, and the scattered light from the tip will be collected. When the tip is in close proximity to the sample, the presence of the sample will change the polarizability of the tip. Therefore, the near-field signal with sample surface optical information can be measured. Nowadays the apertureless NSOM or scattering NSOM is one of the most powerful tools to get sample two-dimensional optical information with extremely high resolution.

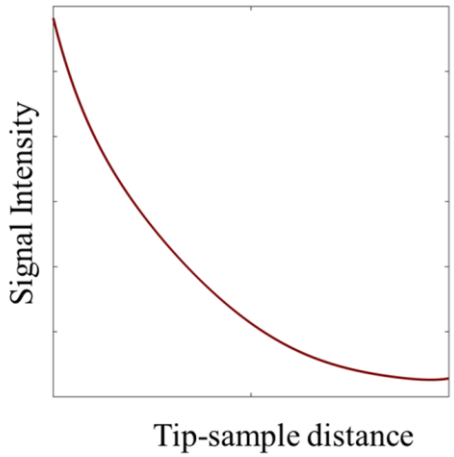

Figure 6. 1 Near-field Plamson-matter interaction curve, nonlinear relation.

The study about the vertical near-field electromagnetic interaction at the tip normal to the sample is still limited. Researchers can use powerful software employing Finite Element Method (FEM) to calculate the field distribution, therefore the near-field interaction between tip and sample

can be simulated. But lacking of obversion method to directly study the nanoscale behavior is still a big challenge in this field.

Currently the apertureless NSOM use tip sinusoidal oscillation to modulate the signal and remove the large background noise. Based on this modulation, an approach curve can be achieved by approaching the oscillating tip towards the sample and recording the scattering signal. This method is also called Z-plot method. It cannot provide a straightforward inspection of the electromagnetic field distribution along the tip, because each data point on the Z-plot curve is a summation of all the scattering signals within the tip oscillation range during the integration time. The Z-plot curve is a convolution between the oscillation range and the near-field distribution, therefore the results can only describe the near-field in an ambiguous way, just like a blurred imaging method. On the other hand it is necessary to provide a oscillation to modulate the signal, so the large background noise can be cancel.

6.2 Harmonic Reconstruction Method

Some groups have already developed near-field reconstruction method to describe the near-field behavior at the NSOM tip. In their method, a scattering type NSOM configuration is employed to do the near-field scanning. High order harmonic signals are collected by a lock-in amplifier and combined to rebuild the near-field distribution. Instead of trying to record the signal in real space, they record the signal in frequency domain and avoid the convolution problem. By summing all the harmonic components, it is possible to clearly describe the electromagnetic field. However, as we mentioned before, the apertureless NSOM has strong background noise. Part of this noise, which is 1^{st} order harmonic noise, is inherent in the apertureless NSOM configuration. In apertureless NSOM the 1^{st} order harmonic noise comes from probe shaft back scattering. Since the probe shaft and the probe tip has same oscillation frequency f, this backscattering noise is also modulated and

mixed with 1st order harmonic signals. Therefore, even people use harmonic modulation method to remove the large DC noise, they still need to use the Heterodyne system or the Homodyne system to remove the 1st order harmonic noise.[101]

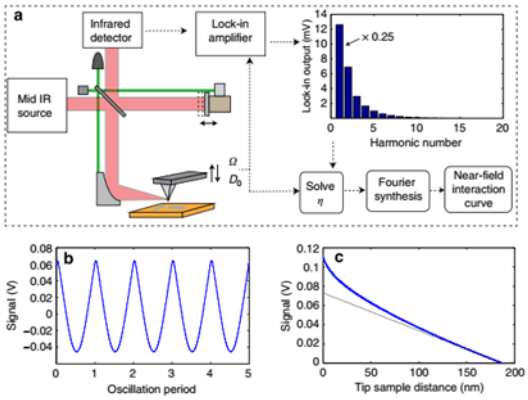

Figure 6. 2 Scattering NSOM high harmonic recontrcution.[101]

In our AgNW-based NSOM configuration, the 1st order harmonic noise is not inherent. Theoretically, the coupling efficiency between the bent tapered angle optical fiber and the AgNW can reach almost 100% as the tip preparation method improves. There is no backscattering noise from probe shaft, and all the light is strongly confined in the small gap between the tip and the sample. In this project we collect photocurrent signal instead of scattering light. Therefore, there is no noise signal oscillates at the frequency f and we don't need special algorithm to remove the 1st order noise. This makes the whole method operated in a simple and flexible way and we can directly reconstruct the tip electromagnetic field.

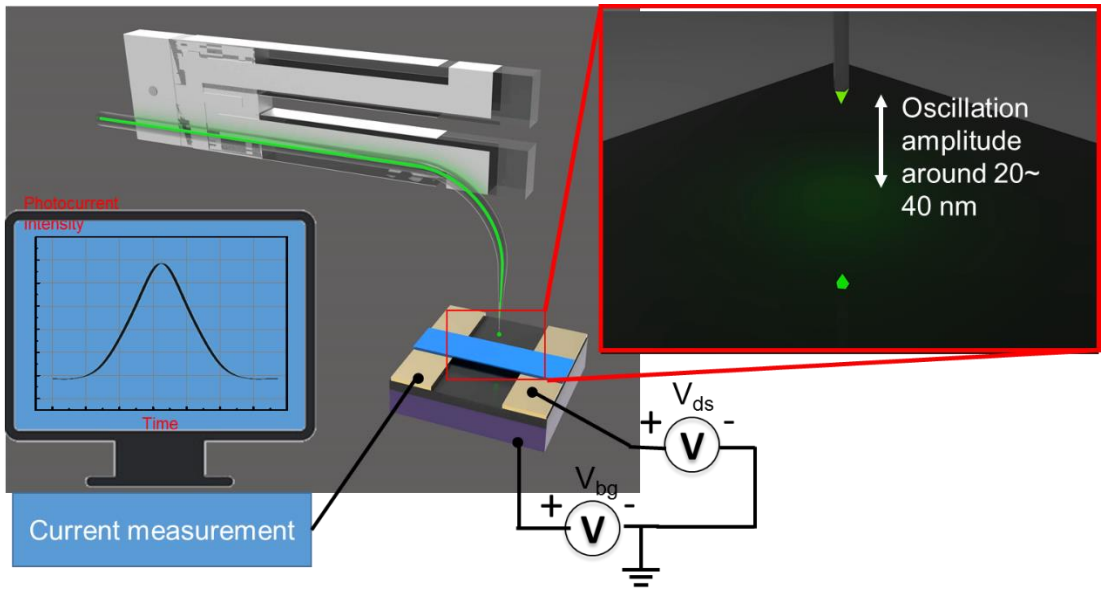

Figure 6. 3 The working principle of our AgNW based NSOM probe for near-field plasmon-matter interaction reconstruction.

It needs 3 steps to reconstruct the tip-sample near-field interaction.

1. Collecting the different order of harmonic components with lock-in amplifier for same scanning area as shown in the figure. The tuning fork probe is oscillating sinusoidally with frequency f, so the AgNW tip movement is $X(t) = X_0 \sin(2\pi \cdot ft)$, here X_0 is the tip oscillation amplitude which is around 20~40 nm. As we mentioned before, the polarizability α_{eff} has nonlinear relation with tip distance x. $\alpha_{eff} = \frac{\alpha(1+\beta)}{1-\alpha\beta/(16\pi(a+x)^3)}$. As the metal tip approaches close to the sample, there are sharp nonlinear changes in both amplitude and phase of the polarizability. The electromagnetic field as a function of tip-sample distance has a nonlinear behavior and can be taken as a signature of the near-field interaction. The nonlinear behavior is the key to generate high order harmonic components. In the figure, the sine wave is oscillating along the nonlinear curve and generates a 'distorted sine wave' photocurrent signal. The photocurrent signal contains different

orders of harmonic components. All these components will be collected by the lock-in amplifier and their proportion PC_n will be recorded.

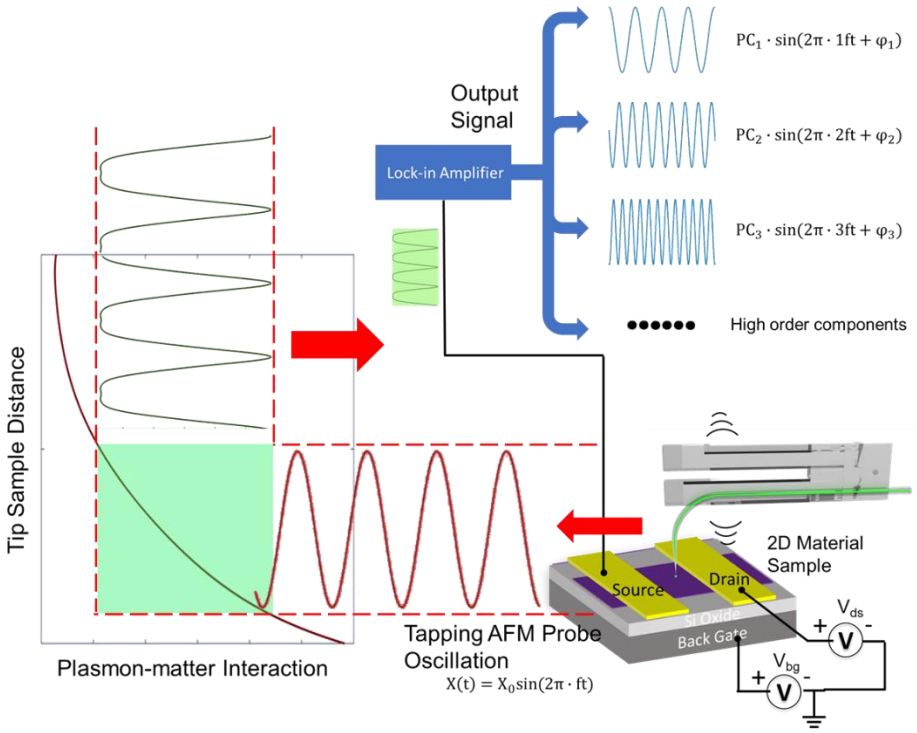

Figure 6. 4 The step one for reconstruction: collecting all harmonic components. Due to the nonlinearity of the plasmon-matter interaction as a function of tip-sample distance, the sine wave with frequency f will create a photocurrent signal with f, 2f 3f … high harmonic components. Using a lock-in amplifies to simultaneously record all the harmonic components for step 1.

2. Combining all the harmonic components to get photocurrent signal in time domain $PC(t) = \sum_n PC_n \cdot \sin(2\pi \cdot nft + \varphi_n)$. According to the Fourier Theory, if $PC(t)$ is integrable on the interval $[t_0\ t_0 + l]$ for real t_0 and l, then in this interval $PC(t)$ can be expressed as an infinite sum of series of harmonic sinusoidal functions as shown in the figure. These functions have the frequency $N \cdot \omega$ where $N \geq 1$ is ian nteger. Their Fourier coefficients decide their weight in the summation. Since their Fourier coefficients have been recorded in step 1, we can try to recover the original signal $PC(t)$.

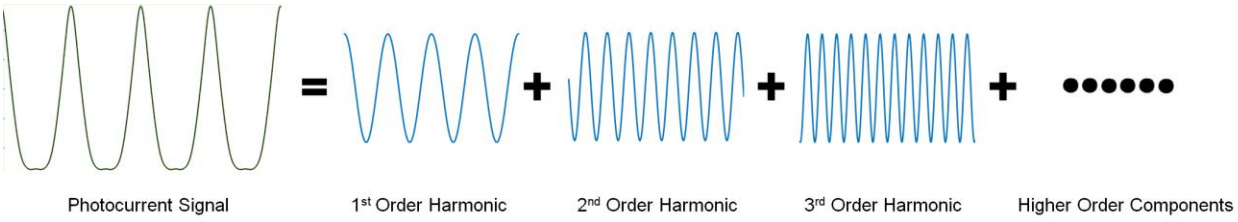

Figure 6. 5 reconstruction of the photocurrent signal as a function of time t.

$$PC(t) = PC_1 \cdot \sin(2\pi \cdot 1ft + \varphi_1) + PC_2 \cdot \sin(2\pi \cdot 2ft + \varphi_2) + PC_3 \cdot \sin(2\pi \cdot 3ft + \varphi_3) + \text{High order components}$$

$$= \sum_n PC_n \cdot \sin(2\pi \cdot nft + \varphi_n)$$

The Approaching curve method records the signal discretely. Each discrete data point is a summation of the neighbor signals within oscillation range. Thus, the approaching curve method can only get an ambiguous result, with part of its signal missing and other part blurred. On the other hand, the Fourier reconstruction method records the signal continuously, if the device sampling frequency is much higher than the tip oscillation frequency. Although there aren't enough channels in the lock-in amplifier to record all the high harmonics components, these missing parts won't affect the result too much since their Fourier coefficients are extremely small compared with the first few harmonic components. In the figure, we compare different Fourier coefficients from harmonic order N=1 to 8. Components order larger than 9 is smaller than thermal noise at their frequencies and cannot be recorded using our devices. From the figure, we can see that the Fourier coefficients follow an exponential decay. Losing high N components information is acceptable since they won't affect the final result too much.

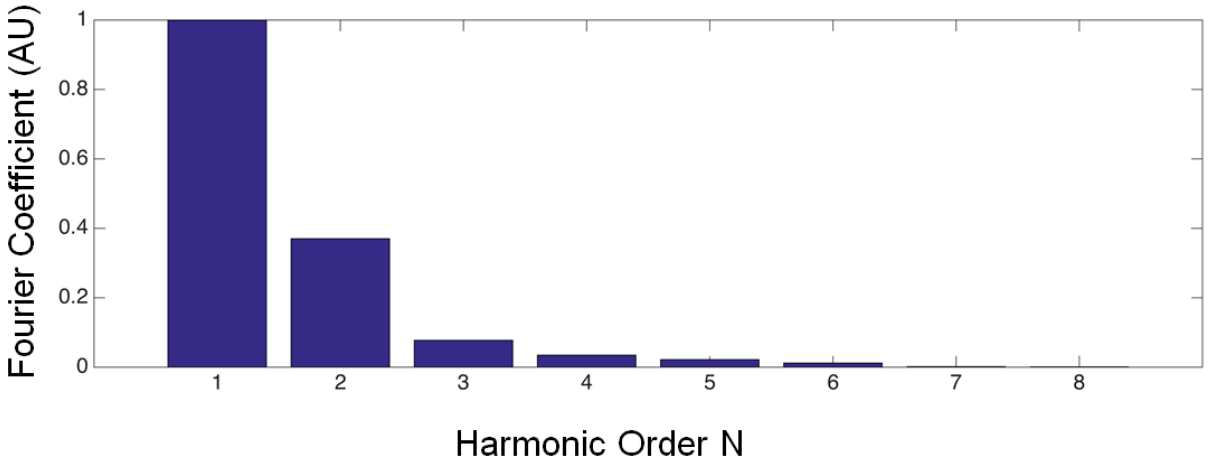

Figure 6. 6 Different harmonic components.

3. Replacing the variable t with tip-sample distance $X(t) = X_0(1 - \sin(2\pi \cdot \omega t))$, and reconstructing the tip electromagnetic field where PC is a function of variable X. This is the near-field interaction between tip and sample.

$$PC(X) = \sum_n PC_n \sin(n \sin^{-1}\left(1 - \frac{X}{X_0}\right) + \varphi_n)$$

By reconstruction of each point on the surface plane, we can rebuild the plasmon-mater interaction at each in-plane point (x,y) with any tip-sample distance z.

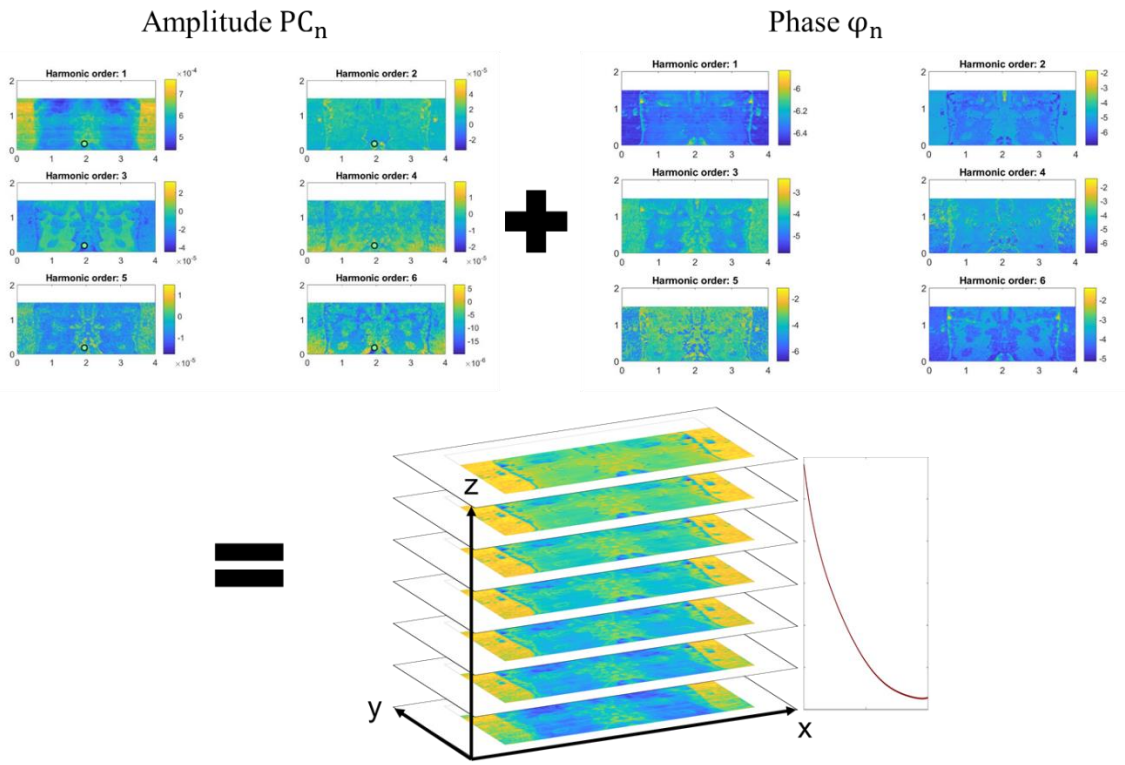

Figure 6. 7 Vertical near-field plasmon-matter interaction reconstruction for each point <x,y,z>.

A further study of vertical near-field plasmon-matter interaction reconstruction will be performed to understand the nanoscale photoresponse in the future.

Conclusion

In conclusion, we provide a revolutionary solution for increasing the NSOM resolution by using AgNW-based NSOM probe.

For AgNW-based SPM probe, we systematically study the SPM performance using AgNW based probe. The AgNWs show both greate electric and force performance. We also show that the sharp tip AgNW is a very powerful tool to achieve high spatial resolution.

For the photocurrent mapping and plasmon-matter interaction, we show comprehensive characterization of two-dimensional materials using our AgNW-based NSOM probe. The high spatial resolution of the photocurrent mapping was conducted to understand the nanoscale photo response which cannot be achieved using conventional optical system. The bandstructure of two-dimensional devices have been clearly studied for the first time. The plasmon-matter interaction using our setup will become a powerful nanoscale analysing tool in thre future.

Bibliography

1 Rayleigh, L. J. T. L., Edinburgh,, Magazine, D. P. & Science, J. o. XXXI. Investigations in optics, with special reference to the spectroscope. **8**, 261-274 (1879).

2 Cancado, L. G., Hartschuh, A. & Novotny, L. Tip-enhanced Raman spectroscopy of carbon nanotubes. *Journal of Raman Spectroscopy* **40**, 1420-1426, doi:10.1002/jrs.2448 (2009).

3 Synge, E. J. T. L., Edinburgh,, Magazine, D. P. & Science, J. o. XXXVIII. A suggested method for extending microscopic resolution into the ultra-microscopic region. **6**, 356-362 (1928).

4 Synge, E. H. J. T. L., Edinburgh,, Magazine, D. P. & Science, J. o. XXIII. An application of piezo-electricity to microscopy. **13**, 297-300 (1932).

5 Dunn, R. C. Near-field scanning optical microscopy. *Chemical Reviews* **99**, 2891-+, doi:DOI 10.1021/cr980130e (1999).

6 Ash, E. & Nicholls, G. J. N. Super-resolution aperture scanning microscope. **237**, 510 (1972).

7 Betzig, E., Trautman, J., Harris, T., Weiner, J. & Kostelak, R. J. S. Breaking the diffraction barrier: optical microscopy on a nanometric scale. **251**, 1468-1470 (1991).

8 Paesler, M. A. & Moyer, P. J. *Near-field optics: theory, instrumentation, and applications*. (Wiley-Interscience, 1996).

9 Valaskovic, G., Holton, M. & Morrison, G. J. A. o. Parameter control, characterization, and optimization in the fabrication of optical fiber near-field probes. **34**, 1215-1228 (1995).

10 Williamson, R. & Miles, M. J. J. o. a. p. Melt‐drawn scanning near‐field optical microscopy probe profiles. **80**, 4804-4812 (1996).

11 Betzig, E. & Trautman, J. K. J. S. Near-field optics: microscopy, spectroscopy, and surface modification beyond the diffraction limit. **257**, 189-195 (1992).

12 Pohl, D. W., Denk, W. & Lanz, M. J. A. p. l. Optical stethoscopy: Image recording with resolution λ/20. **44**, 651-653 (1984).

13 Pohl, D. J. T. S. F. Near-field optics: light for the world of nano-scale science. **264**, 250-254 (1995).

14 Dürig, U., Pohl, D. W. & Rohner, F. J. J. o. a. p. Near‐field optical‐scanning microscopy. **59**, 3318-3327 (1986).

15 Hecht, B., Bielefeldt, H., Pohl, D., Novotny, L. & Heinzelmann, H. J. J. o. a. p. Influence of detection conditions on near-field optical imaging. **84**, 5873-5882 (1998).

16 Veerman, J., Otter, A., Kuipers, L. & Van Hulst, N. J. A. P. L. High definition aperture probes for near-field optical microscopy fabricated by focused ion beam milling. **72**, 3115-3117 (1998).

17 Novotny, L., Pohl, D. & Regli, P. J. J. A. Light propagation through nanometer-sized structures: the two-dimensional-aperture scanning near-field optical microscope. **11**, 1768-1779 (1994).

18 Kavaldjiev, D., Toledo‐Crow, R. & Vaez‐Iravani, M. J. A. p. l. On the heating of the fiber tip in a near‐field scanning optical microscope. **67**, 2771-2773 (1995).

19 Stähelin, M., Bopp, M., Tarrach, G., Meixner, A. & Zschokke‐Gränacher, I. J. A. p. l. Temperature profile of fiber tips used in scanning near‐field optical microscopy. **68**, 2603-2605 (1996).

20 La Rosa, A. H., Yakobson, B. & Hallen, H. J. A. P. L. Origins and effects of thermal processes on near‐field optical probes. **67**, 2597-2599 (1995).

21 Lienau, C., Richter, A. & Elsaesser, T. J. A. p. l. Light‐induced expansion of fiber tips in near‐field scanning optical microscopy. **69**, 325-327 (1996).

22 Pilevar, S., Edinger, K., Atia, W., Smolyaninov, I. & Davis, C. J. A. p. l. Focused ion-beam fabrication of fiber probes with well-defined apertures for use in near-field scanning optical microscopy. **72**, 3133-3135 (1998).

23 Muranishi, M. *et al.* Control of aperture size of optical probes for scanning near-field optical microscopy using focused ion beam technology. **36**, L942 (1997).

24 Novotny, L., Sánchez, E. J. & Xie, X. S. J. U. Near-field optical imaging using metal tips illuminated by higher-order Hermite–Gaussian beams. **71**, 21-29 (1998).

25 Keilmann, F. & Hillenbrand, R. Near-field microscopy by elastic light scattering from a tip. *Philosophical Transactions of the Royal Society a-Mathematical Physical and Engineering Sciences* **362**, 787-805, doi:10.1098/rsta.2003.1347 (2004).

26 Bohren, C. F. & Huffman, D. R. *Absorption and scattering of light by small particles*. (John Wiley & Sons, 2008).

27 Xu, X. G., Tanur, A. E. & Walker, G. C. J. T. J. o. P. C. A. Phase controlled homodyne infrared near-field microscopy and spectroscopy reveal inhomogeneity within and among individual boron nitride nanotubes. **117**, 3348-3354 (2013).

28 Furukawa, H. & Kawata, S. J. O. c. Local field enhancement with an apertureless near-field-microscope probe. **148**, 221-224 (1998).

29 Taubner, T., Hillenbrand, R. & Keilmann, F. J. J. o. m. Performance of visible and mid‐infrared scattering‐type near‐field optical microscopes. **210**, 311-314 (2003).

30 Knoll, B. & Keilmann, F. J. O. c. Enhanced dielectric contrast in scattering-type scanning near-field optical microscopy. **182**, 321-328 (2000).

31 Keilmann, F., Hillenbrand, R. J. P. T. o. t. R. S. o. L. S. A. M., Physical & Sciences, E. Near-field microscopy by elastic light scattering from a tip. **362**, 787-805 (2004).

32 Hillenbrand, R. & Keilmann, F. J. P. R. L. Complex optical constants on a subwavelength scale. **85**, 3029 (2000).

33 Ocelic, N., Huber, A. & Hillenbrand, R. J. A. P. L. Pseudoheterodyne detection for background-free near-field spectroscopy. **89**, 101124 (2006).

34 Sasaki, Y. & Sasaki, H. J. J. J. o. A. P. Heterodyne detection for the extraction of the probe-scattering signal in scattering-type scanning near-field optical microscope. **39**, L321 (2000).

35 Hild, S. *et al.* DC-readout of a signal-recycled gravitational wave detector. *Classical and Quantum Gravity* **26**, doi:Artn 055012

10.1088/0264-9381/26/5/055012 (2009).

36 Stefan, G. *et al.* TOWARDS IMAGING SKIN CANCER BY APERTURELESS SCANNING NEAR-FIELD OPTICAL MICROSCOPY.

37 Maier, S. A. *Plasmonics: fundamentals and applications*. (Springer Science & Business Media, 2007).

38 Kretschmann, E. J. O. C. The angular dependence and the polarisation of light emitted by surface plasmons on metals due to roughness. **5**, 331-336 (1972).

39 Wild, B. *et al.* Propagation lengths and group velocities of plasmons in chemically synthesized gold and silver nanowires. **6**, 472-482 (2012).

40 Allione, M., Temnov, V. V., Fedutik, Y., Woggon, U. & Artemyev, M. V. J. N. l. Surface plasmon mediated interference phenomena in low-Q silver nanowire cavities. **8**, 31-35 (2008).

41 Hayazawa, N., Inouye, Y., Sekkat, Z. & Kawata, S. J. O. C. Metallized tip amplification of near-field Raman scattering. **183**, 333-336 (2000).

42 Pettinger, B., Ren, B., Picardi, G., Schuster, R. & Ertl, G. J. P. r. l. Nanoscale probing of adsorbed species by tip-enhanced Raman spectroscopy. **92**, 096101 (2004).

43 Novotny, L. & Stranick, S. J. J. A. R. P. C. Near-field optical microscopy and spectroscopy with pointed probes. **57**, 303-331 (2006).

44 Cançado, L. G., Hartschuh, A., Novotny, L. J. J. o. R. S. A. I. J. f. O. W. i. a. A. o. R. S., Including Higher Order Processes,, Brillouin, a. & Scattering, R. Tip‐enhanced Raman spectroscopy of carbon nanotubes. **40**, 1420-1426 (2009).

45 Anderson, M. S. J. A. P. L. Locally enhanced Raman spectroscopy with an atomic force microscope. **76**, 3130-3132 (2000).

46 Weber-Bargioni, A. *et al.* Hyperspectral nanoscale imaging on dielectric substrates with coaxial optical antenna scan probes. **11**, 1201-1207 (2011).

47 Fleischer, M. *et al.* Gold nanocone near-field scanning optical microscopy probes. **5**, 2570-2579 (2011).

48 Ren, B., Picardi, G. & Pettinger, B. J. R. o. S. I. Preparation of gold tips suitable for tip-enhanced Raman spectroscopy and light emission by electrochemical etching. **75**, 837-841 (2004).

49 Nieman, L. T., Krampert, G. M. & Martinez, R. E. J. R. o. S. I. An apertureless near-field scanning optical microscope and its application to surface-enhanced Raman spectroscopy and multiphoton fluorescence imaging. **72**, 1691-1699 (2001).

50 You, Y. *et al.* Tip‐enhanced Raman spectroscopy using single‐crystalline Ag nanowire as tip. **41**, 1156-1162 (2010).

51 Fujita, Y. *et al.* A silver nanowire-based tip suitable for STM tip-enhanced Raman scattering. **50**, 9839-9841 (2014).

52 Stöckle, R. M., Suh, Y. D., Deckert, V. & Zenobi, R. J. C. P. L. Nanoscale chemical analysis by tip-enhanced Raman spectroscopy. **318**, 131-136 (2000).

53 Yeo, B.-S., Zhang, W., Vannier, C. & Zenobi, R. J. A. s. Enhancement of Raman signals with silver-coated tips. **60**, 1142-1147 (2006).

54 Hayazawa, N. *et al.* Visualization of localized strain of a crystalline thin layer at the nanoscale by tip‐enhanced Raman spectroscopy and microscopy. **38**, 684-696 (2007).

55 Moretti, M. *et al.* Reflection-mode TERS on insulin amyloid fibrils with top-visual AFM probes. **8**, 25-33 (2013).

56 Zhang, W., Yeo, B. S., Schmid, T. & Zenobi, R. J. T. J. o. P. C. C. Single molecule tip-enhanced Raman spectroscopy with silver tips. **111**, 1733-1738 (2007).

57 Hartschuh, A. *et al.* Tip-enhanced near-field optical microscopy of carbon nanotubes. **394**, 1787-1795 (2009).

58 Yeo, B.-S., Mädler, S., Schmid, T., Zhang, W. & Zenobi, R. J. T. J. o. P. C. C. Tip-enhanced Raman spectroscopy can see more: the case of cytochrome c. **112**, 4867-4873 (2008).

59 Wiley, B., Sun, Y., Mayers, B. & Xia, Y. J. C. A. E. J. Shape‐controlled synthesis of metal nanostructures: the case of silver. **11**, 454-463 (2005).

60 Fujita, Y., Walke, P., De Feyter, S. & Uji-i, H. J. J. J. o. A. P. Remote excitation-tip-enhanced Raman scattering microscopy using silver nanowire. **55**, 08NB03 (2016).

61 Walke, P. *et al.* Silver nanowires for highly reproducible cantilever based AFM-TERS microscopy: towards a universal TERS probe. **10**, 7556-7565 (2018).

62 Sanders, A. W. *et al.* Observation of plasmon propagation, redirection, and fan-out in silver nanowires. **6**, 1822-1826 (2006).

63 Pyayt, A. L., Wiley, B., Xia, Y., Chen, A. & Dalton, L. J. N. n. Integration of photonic and silver nanowire plasmonic waveguides. **3**, 660 (2008).

64 Zhu, Y. *et al.* Size effects on elasticity, yielding, and fracture of silver nanowires: In situ experiments. **85**, 045443 (2012).

65 Ma, X. *et al.* Sharp-Tip Silver Nanowires Mounted on Cantilevers for High-Aspect-Ratio High-Resolution Imaging. **16**, 6896-6902 (2016).

66 Sun, Y., Yin, Y., Mayers, B. T., Herricks, T. & Xia, Y. J. C. o. M. Uniform silver nanowires synthesis by reducing AgNO3 with ethylene glycol in the presence of seeds and poly (vinyl pyrrolidone). **14**, 4736-4745 (2002).

67 Korte, K. E., Skrabalak, S. E. & Xia, Y. J. J. o. M. C. Rapid synthesis of silver nanowires through a CuCl-or CuCl 2-mediated polyol process. **18**, 437-441 (2008).

68 Wang, J. *et al.* Silver nanowire electrodes: conductivity improvement without post-treatment and application in capacitive pressure sensors. **7**, 51-58 (2015).

69 Ansar, S. M. *et al.* Removal of molecular adsorbates on gold nanoparticles using sodium borohydride in water. **13**, 1226-1229 (2013).

70 Luo, M. *et al.* Facile removal of polyvinylpyrrolidone (PVP) adsorbates from Pt alloy nanoparticles. **3**, 2770-2775 (2015).

71 Chen, C. J. *Introduction to scanning tunneling microscopy*. Vol. 4 (Oxford University Press on Demand, 1993).

72 Wiley, B., Herricks, T., Sun, Y. & Xia, Y. J. N. L. Polyol synthesis of silver nanoparticles: use of chloride and oxygen to promote the formation of single-crystal, truncated cubes and tetrahedrons. **4**, 1733-1739 (2004).

73 Gere, J. M. & Goodno, B. J. *Mechanics of Materials, Brief Edition*. (Cengage Learning, USA, 2012).

74 Vlassov, S. *et al.* Elasticity and yield strength of pentagonal silver nanowires: In situ bending tests. **143**, 1026-1031 (2014).

75 Ma, X. *et al.* Capillary-force-assisted clean-stamp transfer of two-dimensional materials. **17**, 6961-6967 (2017).

76 Stadler, J., Schmid, T. & Zenobi, R. J. N. l. Nanoscale chemical imaging using top-illumination tip-enhanced Raman spectroscopy. **10**, 4514-4520 (2010).

77 Calahorra, Y., Shtempluck, O., Kotchetkov, V. & Yaish, Y. J. N. l. Young's modulus, residual stress, and crystal orientation of doubly clamped silicon nanowire beams. **15**, 2945-2950 (2015).

78 Narayanan, S., Cheng, G., Zeng, Z., Zhu, Y. & Zhu, T. J. N. l. Strain hardening and size effect in five-fold twinned Ag nanowires. **15**, 4037-4044 (2015).

79 Gramotnev, D. K. & Bozhevolnyi, S. I. J. N. p. Plasmonics beyond the diffraction limit. **4**, 83 (2010).

80 Laroche, T. & Girard, C. J. A. p. l. Near-field optical properties of single plasmonic nanowires. **89**, 233119 (2006).

81 Zou, C.-L. *et al.* Plasmon modes of silver nanowire on a silica substrate. **97**, 183102 (2010).

82 Khanarian, G. *et al.* The optical and electrical properties of silver nanowire mesh films. **114**, 024302 (2013).

83 Luu, Q. N. *et al.* Preparation and optical properties of silver nanowires and silver-nanowire thin films. **356**, 151-158 (2011).

84 Li, Z., Zhang, S., Halas, N. J., Nordlander, P. & Xu, H. J. S. Coherent Modulation of Propagating Plasmons in Silver‐Nanowire‐Based Structures. **7**, 593-596 (2011).

85 Barnes, W. L., Dereux, A. & Ebbesen, T. W. J. n. Surface plasmon subwavelength optics. **424**, 824 (2003).

86 Wang, W., Yang, Q., Fan, F., Xu, H. & Wang, Z. L. J. N. l. Light propagation in curved silver nanowire plasmonic waveguides. **11**, 1603-1608 (2011).

87 Garnett, E. C. *et al.* Self-limited plasmonic welding of silver nanowire junctions. **11**, 241 (2012).

88 Zhang, S. *et al.* Chiral surface plasmon polaritons on metallic nanowires. **107**, 096801 (2011).

89 Deng, P., Hong, W. & Hong-Xing, X. J. C. P. B. Metallic nanowires for subwavelength waveguiding and nanophotonic devices. **22**, 097305 (2013).

90 Huang, Y. *et al.* Nanowire-supported plasmonic waveguide for remote excitation of surface-enhanced Raman scattering. **3**, e199 (2014).

91 Dong, C.-H. *et al.* Coupling of light from an optical fiber taper into silver nanowires. **95**, 221109 (2009).

92 Babadjanyan, A., Margaryan, N. & Nerkararyan, K. V. J. J. o. A. P. Superfocusing of surface polaritons in the conical structure. **87**, 3785-3788 (2000).

93 Stockman, M. I. J. P. r. l. Nanofocusing of optical energy in tapered plasmonic waveguides. **93**, 137404 (2004).

94 Esmann, M. *et al.* k-space imaging of the eigenmodes of sharp gold tapers for scanning near-field optical microscopy. **4**, 603 (2013).

95 King, G. & Nunes Jr, G. J. R. o. S. I. Attractive-mode force microscope for investigations of biomolecules under ambient conditions. **72**, 4261-4265 (2001).

96 Giessibl, F. J. J. A. P. L. High-speed force sensor for force microscopy and profilometry utilizing a quartz tuning fork. **73**, 3956-3958 (1998).

97 Tung, V. T., Chizhik, S., Hoai, T. X., Tinh, N. T. & Chikunov, V. in *Scanning Probe Microscopy-Physical Property Characterization at Nanoscale* (InTech, 2012).

98 Edwards, H., Taylor, L., Duncan, W. & Melmed, A. J. J. J. o. A. P. Fast, high-resolution atomic force microscopy using a quartz tuning fork as actuator and sensor. **82**, 980-984 (1997).

99 Neto, A. C., Guinea, F., Peres, N. M., Novoselov, K. S. & Geim, A. K. J. R. o. m. p. The electronic properties of graphene. **81**, 109 (2009).

100 Geim, A. K. & Novoselov, K. S. in *Nanoscience and Technology: A Collection of Reviews from Nature Journals* 11-19 (World Scientific, 2010).

101 Wang, L. & Xu, X. G. J. N. c. Scattering-type scanning near-field optical microscopy with reconstruction of vertical interaction. **6**, 8973 (2015).